

Spin-dependent transport in
cobalt nanocontacts

Vom Fachbereich Physik
der
Universität Duisburg-Essen
zur Erlangung des akademischen Grades eines
Doktors der Naturwissenschaften
genehmigte Dissertation

von

George Sarau

aus

Macin (Rumänien)

Referent: Prof. Dr. Claus M. Schneider
Korreferent: Prof. Dr. Günter Dumpich
Tag der mündlichen Prüfung: 16 April 2007

Promotor: Prof. Dr. Claus M. Schneider

Zusammenfassung

Diese Arbeit beschreibt die Herstellung und Untersuchung des Magneto-
transports in Kobalt Nanokontakten. Der Einfluss der Formanisotropie
auf die Magnetisierungsumkehr und die Wechselbeziehung zwischen spin-
abhängigem Transport und der magnetischen Mikrostruktur, welche durch
Simulation bestimmt wurde, wurden untersucht. Die Kobalt Nanokontakte
wurden in planarer Geometrie zwischen zwei breiteren Elektroden auf einem
Si/SiO₂ Substrat hergestellt unter Ausnutzung des Proximity-Effekts der
Elektronenstrahlolithographie in Verbindung mit einem speziellen Layout.
Dieses Verfahren führt zu mechanisch stabilen Nanokontakten, die frei von
Magnetostriktionseffekten sind.

Die Ergebnisse dieser Arbeit belegen, dass es zwei separable Beiträge zum
Magnetowiderstand (MW) gibt, die unabhängig beeinflussbar sind. Der
Magnetowiderstand bei hohen Feldern wird bestimmt von den Elektroden
und kann durch Variation der Breite der individuellen Elektroden modifiziert
werden, während der Magnetowiderstand bei schwachen Magnetfeldern der
Nanokontakt-Region zugeschrieben wird und von der Breite und Form der-
selben abhängt. Wenn die Elektroden entlang der y-Richtung (senkrecht zur
Stromrichtung) ausgedehnt sind, wird in longitudinaler Konfiguration (Feld
entlang der Stromrichtung x) ein Anstieg des reversiblen Hochfeld-MW
beobachtet, der von einem positiven Beitrag durch Domänenwandbildung
in den Elektroden stammt. In der transversalen Konfiguration (Feld ent-
lang y) zeigt der Hochfeld MW keine signifikante Abhängigkeit von
der Breite der Elektroden, da der Umkehrprozess der Magnetisierung do-
miniert wird von Rotation anstatt von Domänenwandbildung. Abhängig
von der Richtung des Magnetfeldes relativ zum Stromfluss werden reversible
oder irreversible Schaltvorgänge im Niedrigfeld-MW beobachtet. Durch
Veränderung der Form der Elektroden erhält man verschiedene Nanokontakt-
Geometrien. Dies führt zu verändertem Verhalten der Magnetisierung des
Nanokontakts in Folge der Formanisotropie. Für longitudinale Konfig-
uration findet ein Übergang von einem scharfen Schaltprozess zu einem
mehrstufigen Vorgang statt, wenn die Elektrodenbreite und damit die Ein-
schnürungskrümmung des Nanokontakts vergrößert wird. Bei transversalem
Feld hingegen geht minimal hysteretisches, quasi reversibles Schaltverhal-
ten bei geringer Krümmung in ebenfalls mehrstufiges Schalten über. Die
irreversiblen Schaltvorgänge stehen in Zusammenhang mit der Existenz
von Domänenwänden im Nanokontakt, während reversible Prozesse durch
kohärente Rotation der Magnetisierung zwischen der leichten und schweren
Richtung verursacht werden. Die Form der MW Kurve und der Abfall
des relativen Widerstands um bis zu 1% zeigen, dass der Anisotrope Mag-
netowiderstand (AMW) in allen gemessenen Systemen den dominierenden
Beitrag darstellt.

Mikromagnetische Simulationen zeigen, dass zwei Domänenwände beiderseits des Nanokontaktes der vollständigen Magnetisierungsumkehr vorausgehen. Für ein longitudinales Feld vereinigen sich beide Domänenwände und annihilieren direkt im Nanokontakt. Dies steht in direkter Verbindung mit dem experimentell beobachteten scharfen Schaltprozess. Die Präsenz von Domänenwänden im Nanokontakt im Bereich niedriger Magnetfelder wird ebenfalls bestätigt durch “minor” MW Hystereseschleifen. Bei transversalem Feld wird der Nanokontakt als letztes durch Rotation ummagnetisiert, was einer nicht- oder minimal hysteretischen MW-Kurve entspricht. Aus dem Vergleich von Simulation und Experiment lässt sich ein mittlerer positiver Grenzflächenwiderstand einer einzelnen Domänenwand von $8.4 \times 10^{-7} \Omega\text{m}^2$ und ein Domänenwand-MW von 0.07% abschätzen.

Die bei 4 K MW Messungen wurden vom Exchange Bias Effekt durch die antiferromagnetische oxidierte Co Oberfläche beeinflusst. Beim Kühlen in angelegtem Magnetfeld wird daher in der Co Schicht eine unidirektionale Anisotropie entlang der Richtung des Einkühlfeldes induziert. Die Magnetisierungsumkehr findet entweder überwiegend durch Domänenbildung oder Magnetisierungsrotation zwischen den beiden leichten Richtungen in Folge der Formanisotropie und des Bias-Feldes statt. Im Fall des feldlosen Kühlens variiert die Richtung des Exchange Bias lokal mit der Domänenstruktur der Probe und verursacht sukzessive nichtreproduzierbare MW Kurven.

Contents

1	Introduction	3
2	Fundamental aspects	7
2.1	Magnetic domains and domain walls	8
2.1.1	Magnetic domains	8
2.1.2	Bulk domain walls	9
2.1.3	Geometrically confined domain walls	12
2.2	Anisotropic Magnetoresistance	15
2.3	Magnetization reversal processes	15
2.3.1	Anisotropic magnetoresistance and magnetization reversal	17
2.4	Domain wall magnetoresistance - theoretical models	19
2.4.1	Diffusive regime	19
2.4.1.1	Positive domain wall magnetoresistance	21
2.4.1.2	Negative domain wall magnetoresistance	24
2.4.2	Ballistic regime	25
2.5	Nanocontacts: Experimental situation	27
2.5.1	Large domain wall magnetoresistance - ballistic limit	27
2.5.2	Small domain wall magnetoresistance - diffusive limit	29
2.6	Micromagnetic calculations	31
3	Experimental techniques	35
3.1	Sample preparation	35
3.1.1	Optical lithography	36
3.1.2	Electron beam lithography	38
3.2	Setup for transport measurements	42
3.3	Magnetic Force Microscopy	44
4	Experimental results and discussions	47
4.1	Cobalt thin films	48
4.2	Long rectangular electrodes: Structure A	51
4.3	Mixed electrodes: Structure B	61
4.4	“Butterfly” electrodes: Structure C	66

5 Conclusions and Outlook	73
References	80
Acknowledgments	88
Curriculum Vitae	89

Chapter 1

Introduction

The effect of an external magnetic field on the electronic transport in ferromagnetic materials - the magnetoresistance (MR) - is a physical effect of fundamental and industrial interest. Magnetic memory devices are used to store data by magnetic hysteresis and magnetic field sensors are used to read data by magnetoresistance effects. The oldest known MR effect, discovered in 1857 by W. Thomson, is the anisotropic magnetoresistance (AMR), which results from spin-orbit scattering and is manifested as the resistance variation with the angle between the local magnetization and electrical current lines. The AMR effect in thin films was exploited in first magnetoresistive read heads for magnetic hard disk drives in 1992, resulting in an increase of the annual growth rate of the storage density from 25% to 60%. A giant magnetoresistance effect (GMR) was discovered in 1988 by P. Grünberg and A. Fert [1, 2] in systems consisting of two magnetic layers separated by a thin spacer layer a few nm thick. The resistance is usually lower when the magnetizations in the two ferromagnetic layers are parallel than in the anti-parallel case. This discovery had a great impact both through its industrial applications as read-heads, enabling the storage density to be increased at a 100% rate per year, and Magnetic Random Access Memories (MRAM), as well as for triggering the field of *spintronics* (SPIN elecTRONICS), aiming to use the spin of the charge carriers in electronic devices with enhanced functionalities. The integration of AMR and GMR read heads into the computer technology have helped to increase the areal density of magnetic disk drive by a factor of 35 millions, since the introduction of the first disk drive (RAMAC) in 1957 by IBM. This development was possible by decreasing the size of the magnetic grains that make up data bits and increasing the read head sensitivity (AMR - few percent, GMR - 65% [3]) along with a decrease in its size. Another magnetic device is the magnetic tunnel junction (MTJ), which is currently slowly replacing GMR read heads and has potential use in high speed, high density and nonvolatility MRAM. It consists of two ferromagnetic metals separated by

a thin insulating layer. The tunneling current across the MTJ depends on the magnetic arrangement of the magnetic moments of the magnetic layers and is higher when the magnetic moments are aligned parallel than in the anti-parallel case. Tunneling magnetoresistance (TMR) effects of 350 % were reported and the theoretical models do not appear to place a limit on the TMR value [4]. A huge change in resistance, called colossal magnetoresistance (CMR), was observed in perovskite materials. An effect of 10^6 % was found in $La_{1-x}Ca_xMnO_3$ system [5] in the antiferromagnetic phase, where the application of a magnetic field induces a ferromagnetic alignment of spins that is highly beneficial to the electron conduction.

As the tendency towards miniaturization increases, it is important to understand, how the magnetoresistive effects are influenced by size reduction. By decreasing the size of a magnetic structure an increased fraction of its volume will consist of domain walls as long as they can be accommodated. Because of the local modulation of magnetic moments inside the domain walls, an additional magnetoresistance is generated, namely domain wall magnetoresistance (DWMR). In practice, a constriction is used to pin a domain wall of comparable size. There are two regimes of DWMR defined as function of the domain wall width, namely, the diffusive regime applicable for nm wide nanocontacts and the ballistic DWMR in the case of atomic point contacts. The diffusive DWMR is embedded in AMR, which in this case comes from the non-collinear magnetization inside the domain wall. The ballistic DWMR, known also as ballistic magnetoresistance (BMR), is attributed to a non-adiabatically accommodation of electron spin when passing a sharp domain wall pinned at the nanocontact. The thinner the domain wall, the more the system approximates to that of a GMR layer structure in which the change in the spin orientation is very abrupt when passing through the interfaces.

From the theoretical point of view positive and negative contributions of domain walls to the total resistance of a ferromagnetic metal are predicted. In the diffusive regime, the *additional* resistance given by a domain wall is direct proportional to the degree of spin-polarization of the current and inversely proportional to the square of the wall width, so that narrow walls are required to obtain a large MR. The MR ratio is independent of the overall scattering rate, thus, the relevant length scale is set by the rate at which the spin of the electrons can relax to track the changing magnetization direction in the domain wall [39, 40, 43, 45]. A domain wall can also cause a redistribution of the electrons between the spin-up and spin-down bands and thus modify the resistivity when the scattering relaxation times are different. A slight stoichiometry and morphological variations can result in a *negative* as well as a *positive* contribution, depending on the difference of scattering relaxation times [47]. In a disordered system, the wall suppresses the interference between the electrons, and hence *decreases* the resistance

in the weakly localized regime [46]. To get access to the ballistic regime, the nanocontact must be of atomic scale, resulting in a domain wall of atomic dimensions trapped there in the antiferromagnetically aligned state. This domain wall can influence the number of open conduction channels, transmission probabilities and degrees of spin polarization and spin-flipping.

The first observation of a (negative) MR of 200 % attributed to the BMR effect at room temperature was reported for mechanically formed point contacts made by touching two Ni wires [56]. The effect was only seen for contacts with a conductance of a few times the quantum unit of conductance $G = 2e^2/h$, implying that the contact area is little more than a few atoms. This result attracted a large number of other groups to look at this effect. New experiments were performed on electrodeposited nanocontacts across nickel wires in a “T” geometry with claims of magnetoresistance of over 3000% (11 nm estimated diameter) [58] and 100000% (few nm to few tens of nm estimated diameter) [59], with the saturated state being the high resistance one in most samples (positive MR). These results are still hotly debated, raising serious doubt about the origin of the measured BMR, but without ruling out the possibility of true BMR of electronic origin in nanocontacts. A careful series of experiments on similar geometries showed that large MR were caused by artifacts involving magnetostrictive or magnetostatic forces making and breaking the contact and the movement of magnetic nanoparticles created in the contact region during the fabrication using a plating process [60, 61]. Therefore, it is desirable to establish this effect in mechanically stable, lithographically defined structures.

The aim of this work is to explore the interrelation between magnetotransport in rigid, lithographically prepared nanocontacts and magnetic microstructure revealed by micromagnetic simulations. This thesis is divided in three main chapters: fundamental aspects, experimental techniques and experimental results. In the first chapter, the basic concepts necessary to understand spin-dependent transport phenomena in magnetic nanocontacts are introduced. The formation of domain and domain walls in μm large ferromagnetic sample due to energy minimization, the unconstrained Bloch and Néel bulk domain walls and the geometrically confined domain walls are described. AMR effect, magnetization reversal mechanisms and the correlation between them are presented. The theoretical models used to explain the two regimes of DWMR are given, followed by an overview of the experimental results obtained on nanocontacts by other groups, in both ballistic and diffusive regimes. At the end a description of the important issues concerning micromagnetic calculations is presented.

In the second chapter sample fabrication and experimental techniques are described in detail. The cobalt nanocontacts are defined in a planar geometry between two wider electrodes on a Si/SiO₂ substrate using a fabrication method that combines the proximity effect of electron beam lithog-

raphy with a special layout design. The 20 nm thick cobalt structures are linked with the bonding pads, previously defined by optical lithography, in a second EBL step by 100 nm thick Au electrodes. A non-magnetic material is chosen to eliminate any influences on the magnetic reversal of our structures. Magnetoresistance measurements are used as an indirect sensing tool based on the AMR effect to observe to magnetization reversal process in individual structures. Magnetic Force Microscopy (MFM) is used to investigate the remanent magnetic domain configuration of the structures.

In the third chapter the MR measurements performed on cobalt thin films and nanocontacts of different geometries and sizes are given and discussed. The magnetic field is applied in-plane, parallel (longitudinal configuration) as well as perpendicular (transversal configuration) to the nanocontact's axis/current flow direction. The obtained results on Co structures show that there are two separable contributions to the magnetoresistance which can be tuned independently. The high-field MR is given by the electrodes and can be modified by changing the width of individual electrodes, while the low-field MR is attributed to the nanocontact region and was found to depend on both nanocontact shape and width. Depending on the direction of the applied field relative to the current, reversible and irreversible switching events are observed.

The 4 K MR measurements are found to be influenced by the exchange bias effect between the ferromagnetic cobalt electrodes and the antiferromagnetic oxidized Co surface. When cooling down in an applied magnetic field, the uniform biased Co layer behaves as if it possesses a unidirectional anisotropy axis along the field cooling direction. In the zero field cooling case, the exchange bias varies locally throughout the sample giving rise to non-reproducible successive MR traces. The shape of the MR and the relative resistance drop of up to 1.3% indicate that the changes in resistance are due to the AMR effect.

Micromagnetic simulations are used to get a better understanding of magnetization reversal processes and their influence on the spin transport characteristics. Two domain walls pinned on each side of the nanocontact preface the complete reversal. In the longitudinal configuration, the two domain walls merge and dissolve in the nanocontact (irreversible switching event). In the transversal configuration, the nanocontact is the last reversed region by magnetization rotation (reversible event). Combining simulation and experiment, an average positive interface resistance of a single domain wall of $8.4 \times 10^{-7} \Omega\text{m}^2$ and a DWMR of 0.07% are estimated.

In this study, we show that the influence of individual electrodes on the magnetization reversal and switching field of magnetic structures with constrictions can be separated from the nanocontact's contribution. Moreover, the reversible and irreversible transitions in the MR measurements can be linked to the simulated magnetization reversal processes.

Chapter 2

Fundamental aspects

In this chapter the basic concepts necessary to understand spin-dependent transport phenomena in magnetic nanocontacts are introduced. First section (Sec. 2.1) deals with magnetic domains and domain walls (DWs). Two types of domain walls are described: bulk and geometrically confined DWs. The latter appears in magnetic constrictions and represents a new kind of DW, besides the unconstrained Bloch and Néel bulk walls. These systems are characterized by means of magnetoresistive effects, which serve as an indirect sensing tool on the nanometer scale. Anisotropic magnetoresistance (AMR) caused by spin-orbit interaction and domain wall magnetoresistance (DWMR) due to scattering of electrons at the domain walls are used to observe the magnetization reversal processes in cobalt structures with constrictions. The AMR effect is presented in Sec. 2.2, followed by a detailed description of the magnetic reversal for a μm large ferromagnetic sample in Sec. 2.3. Then, the correlation between AMR and magnetization reversal is discussed on the basis of an experimental work taken from literature. The theoretical models used to explain the DWMR effect are given in Sec. 2.4. There are two regimes of DWMR defined as function of the DW width, namely, the diffusive regime applicable for nm wide nanocontacts and the ballistic DWMR in the case of atomic point contacts. The diffusive DWMR is discussed to a larger extent, because it is relevant for the experiments presented in this thesis. The ballistic DWMR is described in order to give the reader a more complete picture of the spin-dependent transport in nanocontacts down to the atomic scale. An overview of the experimental results obtained on nanocontacts by other groups, in both ballistic and diffusive regimes, is given in Sec. 2.5. In the last section (Sec. 2.6), a description of the important issues concerning micromagnetic calculations is presented. The simulations were used to get a better understanding of magnetization reversal processes and their influence on the spin transport characteristics.

2.1 Magnetic domains and domain walls

2.1.1 Magnetic domains

The concept of magnetic domains was suggested by Weiss [6] in order to explain the fact that ferromagnetic materials with spontaneous magnetization could exist in a demagnetized state. This was one of the most important advances in the understanding of ferromagnetism after the earlier works of Ampère [7], Weber [8] and Ewing [9]. Within a magnetic domain, large numbers of atomic moments (typically 10^{12} - 10^{18}) are aligned in parallel due to the exchange interaction. In polycrystalline materials, the magnetization within the domain is almost uniform, with the direction of alignment varying from domain to domain in a more or less random manner and hence, the magnetization of a specimen can be zero. However, in single crystals certain crystallographic axes are preferred by the magnetic moments, which in the absence of a magnetic field will align along one of these equivalent “magnetic easy axes”.

The existence of domains is a consequence of energy minimization as shown first by Landau and Lifschitz [10]. A uniformly magnetized specimen as shown in *Fig. 2.1 a* has a large magnetostatic (demagnetizing) energy associated with it. This is the result of the presence of magnetic free poles at the surface of the specimen generating a demagnetizing field, H_d . This field opposes the field created by the specimen. The demagnetizing field is proportional to the magnetization M and is given by $H_d = N_d M$ where N_d is a demagnetizing factor which is calculated from the sample geometry. The configuration of *Fig. 2.1 a* is preferred by small particle with a few tens of nanometers in diameter [11] for which the domain wall formation is energetically unfavorable due to the exchange energy.

The break up of the magnetization into two domains as illustrated in *Fig. 2.1 b* reduces the magnetostatic energy by half. In fact if the magnet breaks down into N domains then the magnetostatic energy is reduced by a factor of $1/N$, hence *Fig. 2.1 c* has a quarter of the magnetostatic energy of *Fig. 2.1 a*. These stripe-domain patterns are often found in materials with high uniaxial anisotropy, e.g. cobalt and permanent magnets [12]. *Fig. 2.1 d* shows a closure domain structure (Landau pattern) where the magnetostatic energy is zero, however, this is only possible for materials that do not have a strong uniaxial anisotropy. Therefore, the neighboring domains can be at 90° to each other. Although cobalt has an uniaxial anisotropy, shape anisotropy becomes the leading contribution, when polycrystalline films are involved. This leads to a flux-closure magnetic configuration, which was often observed in this thesis on cobalt structures by MFM (see Sec. 3.3).

The introduction of domains raises the overall energy of the system due to the non-collinear magnetization inside the domain walls which results in

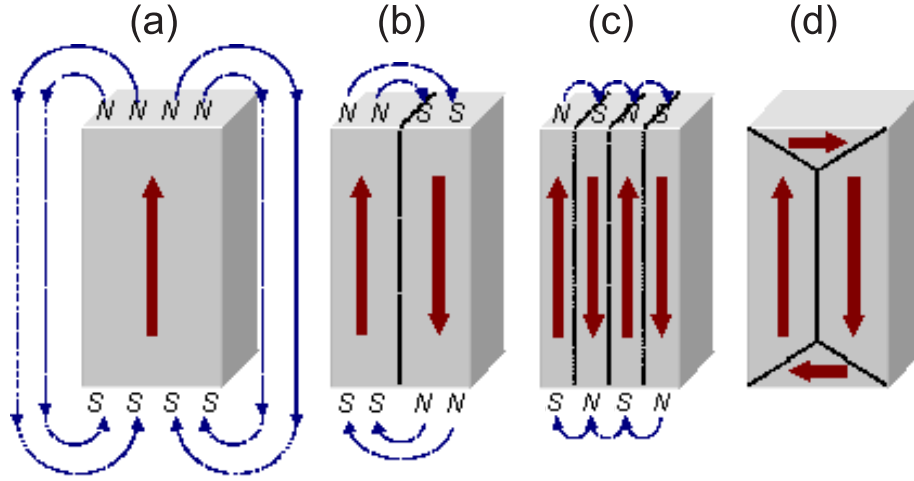


Figure 2.1: Schematic illustration of the break up of magnetization into domains: (a) single domain, (b) two domains, (c) four domains and (d) closure domains. Providing shorter return paths for the magnetic flux at the ends of the specimen or within the specimen reduce the magnetostatic energy. Taken from [13]

an increase in the exchange energy. Therefore, the division into domains only continues, as long as the reduction in magnetostatic energy is greater than the energy required to form the domain wall (associated anisotropy and exchange energy costs). The energy associated with a domain wall is proportional to its area. The magnetic structures studied in this thesis consist of two wide electrodes (1 to 5 μm) with a nanoconstriction between them. Therefore, two types of domain walls will be discussed, namely, bulk DWs and geometrically confined DWs.

2.1.2 Bulk domain walls

A domain wall is the transition region between two magnetic domains where the magnetic moments undergo a reorientation as was first suggested by Bloch [14]. The wall width is determined from a balance of the anisotropy energy and exchange energy. The crystalline anisotropy tends to make the domain wall thinner, because the anisotropy energy is lowest when all moments are aligned along crystallographically equivalent easy axes. Thus, the magnetization can change abruptly from one easy direction to another in traversing the wall. On the other hand, the exchange energy tends to make the walls thicker, since the exchange energy in a ferromagnet is minimized when neighboring moments are aligned parallel, resulting in a continuous and gradual variation of the magnetization in the wall. Therefore, the domain wall energy is an intrinsic property of the material, depending on the degree of magnetocrystalline anisotropy and the strength of the exchange interaction between neighboring atoms.

There are two main types of walls schematically shown in *Fig. 2.2*: the Bloch wall and the Néel wall. Both represent strongly simplified models for the actual arrangement of the magnetization in domain walls. Generally, the most probable case for a wall transition is a mixed form of both Bloch and Néel walls. In the Bloch wall [14] the magnetization vector rotates around an axis normal to the domain wall leading to magnetic charges where the Bloch wall intersects the surface. In the Néel wall [15], which is prevalent in thin films, the magnetization rotates in the plane of the structure. A Néel wall is free of surface charges, but leads to volume charges. Therefore, the ratio of the surface to the volume of the sample determines, which one of these wall types is energetically favored. The transition from Néel walls to Bloch walls with increasing layer thickness has been derived analytically by Néel [15] and has been calculated by means of micromagnetics by Trunk *et al.* [16]. A more complex domain structure has been found at the transition thickness, namely, the cross-tie wall [12, 17]. It consists of a periodic sequence of vortex and antivortex structures with vertical Bloch line (VBL) of opposite polarization and 90° Néel walls at the surface of the film between the vortex and antivortex.

The characteristic extension of Bloch walls $\delta_B = \pi\sqrt{A/K}$ and Néel walls $\delta_N = \pi\sqrt{2A/\mu_0 M_s^2}$ in bulk materials has been derived analytically by Kronmüller [18]. The domain wall thickness is calculated by minimizing the energy (the sum of the anisotropy and exchange energies) of the wall with respect to its width. The parameters involved are: A - the exchange constant (exchange stiffness), K - anisotropy constant and M_s - the saturation magnetization. For cobalt $A = 30 \times 10^{-12} \text{ J/m}$, $K_u = 520 \times 10^3 \text{ J/m}^3$ and $M_s = 1.4 \times 10^6 \text{ A/m}$ which gives $\delta_B \sim 24 \text{ nm}$ and $\delta_N \sim 15 \text{ nm}$, respectively. In case of polycrystalline films when $D \ll l_{exch,eff}$, the magneto-crystalline anisotropy constant is averaged out by the exchange interaction; the effective anisotropy constant is given by $K_{eff} = K \left(D/\sqrt{A/K} \right)^6$ [19], where D is the average grain size and $l_{exch,eff} = \sqrt{A/K_{eff}}$. This leads to a Bloch wall $\delta_B \sim 380 \text{ nm}$ and $l_{exch,eff} \sim 120 \text{ nm}$, taking $D = 3 \text{ nm}$ as measured by Atomic Force Microscopy (AFM) (see Sec. 4.2). In *Fig. 2.3* a zoom of a MFM image along with two domain wall profiles corresponding to a 180° wall (green line) and 90° wall (blue line) are shown. The wall widths measured between the two crosses/arrows are 380 nm (green arrows) and 320 nm (blue arrows), respectively. No corrections due to the tip shape or mutual interaction with the sample by means of the stray fields were done. A detailed discussion concerning the MFM technique is given in Sec. 3.3. In a narrow constriction a geometrically constrained magnetic domain wall can be formed. It constitutes a new kind of magnetic wall, besides the unconstrained Bloch and Néel walls presented above.

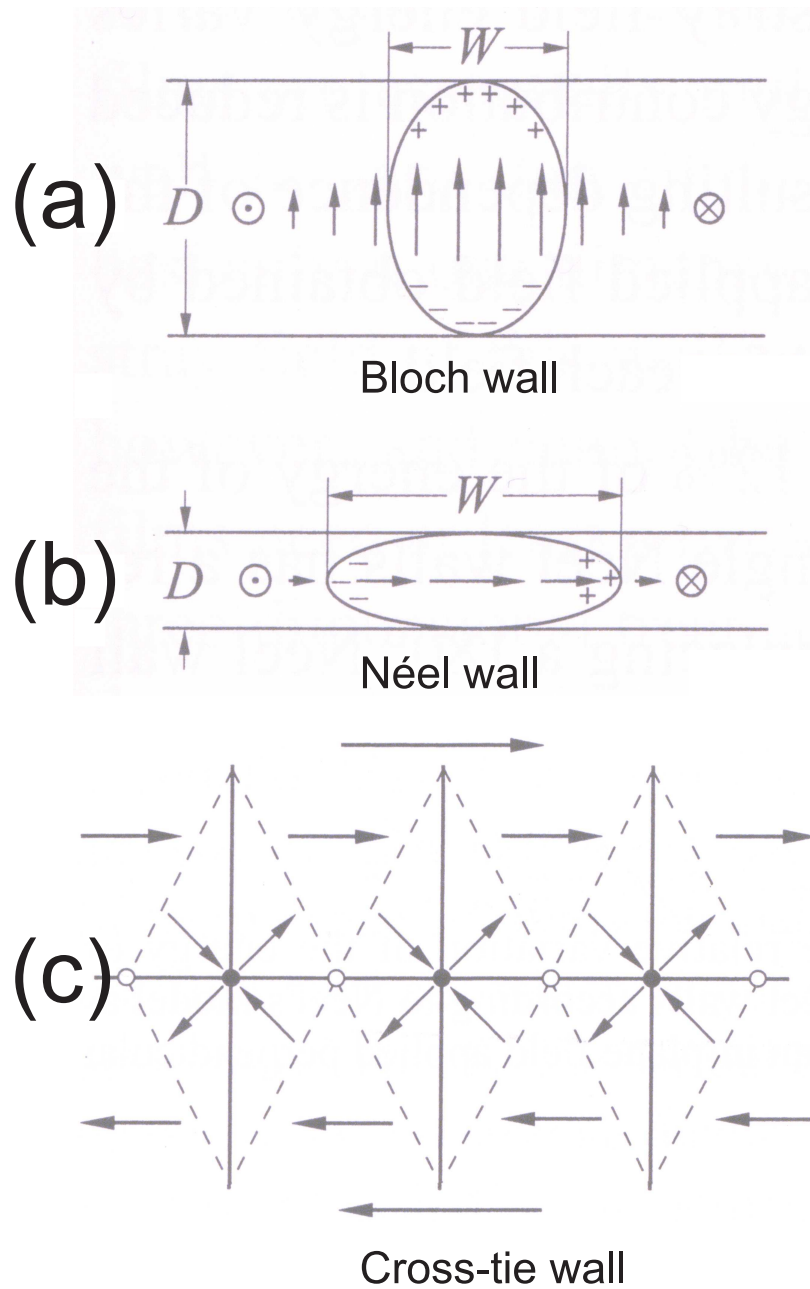


Figure 2.2: Sketches of the internal structure of (a) a Bloch wall with some of the magnetic moments oriented normal to the film plane. This leads to a demagnetization energy associated with the Bloch wall. (b) Néel wall has all moments oriented in the plane. The Néel wall is energetically favored once the film thickness decreases below a certain critical value. (c) A “domain” model of a cross-tie wall. The circular and cross Bloch lines are indicated by open and filled circles, respectively. Taken from [12].

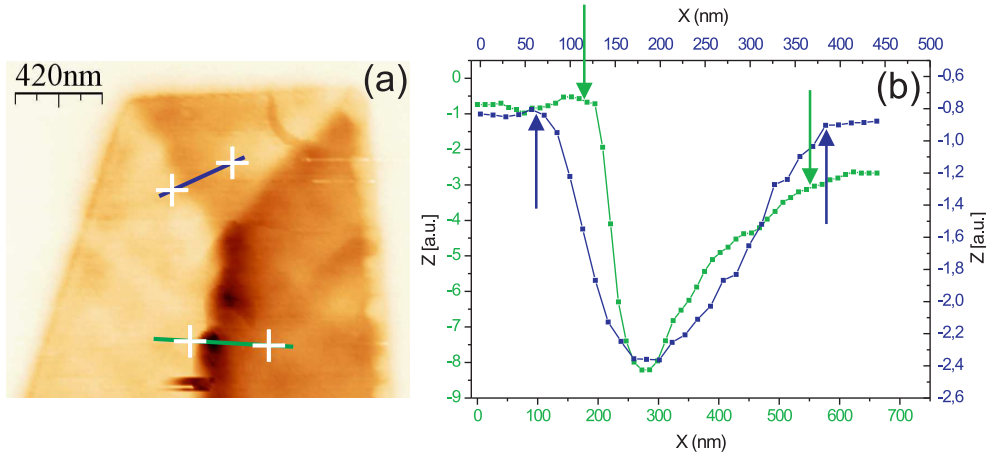


Figure 2.3: (a) Zoom of a MFM image with two domain wall profile lines. (b) The corresponding wall widths given by the distance between the green arrows for the 180° wall and blue arrows for 90° wall are 380 nm and 320 nm, respectively.

2.1.3 Geometrically confined domain walls

The structure and properties of a geometrically constrained magnetic wall in a constriction separating two wider regions were studied theoretically by P. Bruno [20]. This geometry is similar to our experimental configuration. He pointed out that in a constriction the usual $\pi\sqrt{A/K}$ formulation for the domain wall width δ is no longer valid. Considering a constriction whose cross section varies significantly on its length d , it was found that $\delta \sim d$. The wall energy consists mostly of exchange energy. Although for a very narrow wall located at the center of the constriction the exchange energy is very high, it is counterbalanced by the decrease in the wall energy as it occupies a very small volume. Therefore, the wall structure will be controlled essentially by the geometry of the constriction, which determines the strength of the exchange field and only depend weakly on the material parameters such as magnetization, exchange stiffness, and anisotropy constant. A calculated wall profile showing a substantial compression of the wall thickness is shown in *Fig. 2.4*. For an atomic point contact, the width of a domain wall trapped there will also be of atomic dimensions, and hence a good candidate for observing ballistic effects, which will be addressed in Sec. 2.4.2. The only available technique to observe domain walls of atomic dimensions is spin-polarized scanning tunnelling microscopy (SP-STM). This was used by Ding *et al.* to observe extremely narrow walls (1.1 nm) at the surface of a Co (0001) bulk single crystal [21]. Atomically abrupt domain walls ($6 \pm 2 \text{ \AA}$) were observed in Fe nanowires grown by epitaxial step-edge decoration of a vicinal W substrate by Pratzner *et al.* [22].

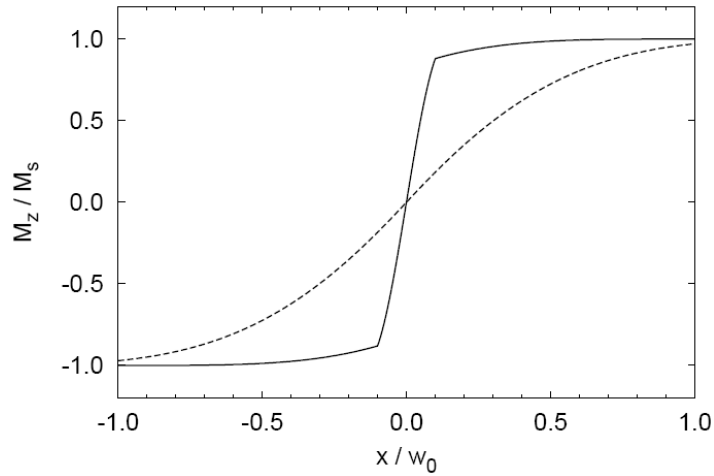


Figure 2.4: Magnetization profile of a geometrically constrained magnetic wall as calculated in [20] for a wire with a rectangular notch where the width is one-tenth that of the main magnetic wire and the length is one-tenth of $w_0 = \pi\sqrt{A/K}$ (solid line), as compared with to the unconstrained Bloch wall with the same w_0 (dashed line). The compression of the wall thickness is easily visible. Taken from [20].

The experimental investigation of magnetization reversal processes on the nanometer scale by means of macroscopic methods, e.g. SQUID (Superconducting QUantum Interference Device) or MOKE (Magneto-Optic Kerr Effect), is impossible, because the magnetic moment of an individual nanocontact is very small. Therefore, magnetoresistance measurements are used as an indirect sensing tool based on magnetoresistive effects such as AMR and diffusive/ballistic DWMR. The appearance of these effects depends on the width of the magnetic structure as sketched in *Fig. 2.5*. In the μm range more than one domain and domain wall contribute to the resistance resulting in about 1% AMR. When dealing with a magnetic nanowire a single domain wall can be introduced and measured [23]. Due to a domain wall extension, which is comparable with the wire width, the DWMR effect is one to two orders of magnitude smaller than the AMR, which in this case comes from the non-collinear magnetization inside the domain wall. This is the diffusive regime of DWMR. When the wire is reduced to a single atom, an atomically abrupt domain wall forms across the contact in the antiferromagnetically aligned state resulting in a 300% change in resistance according to the most recent experimental paper on cobalt atomic point contacts [24]. The effect is known as ballistic magnetoresistance (BMR) or ballistic DWMR. These effects along with the experimental situation are discussed in the following sections.

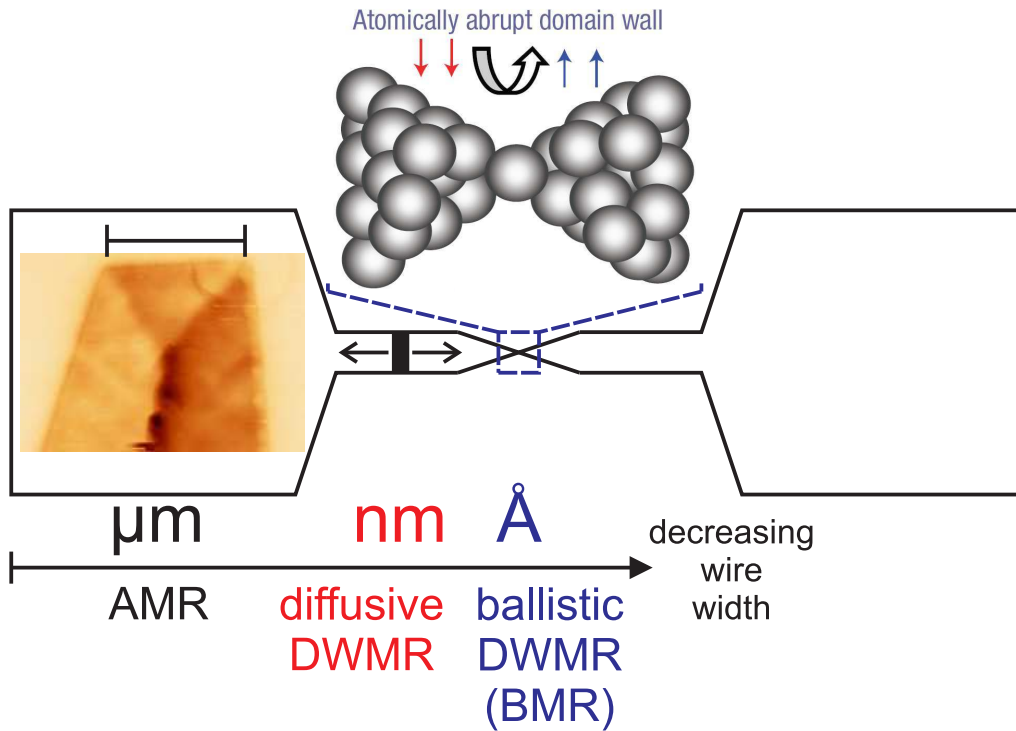


Figure 2.5: Magnetoresistive effects as function of the magnetic structure's width. The μm range is dominated by the anisotropic magnetoresistance. The MFM image illustrates the presence of more than one domain wall in the sample. The scale bar above the MFM image is $1\ \mu\text{m}$. In case of a nanowire, a single domain wall (the black rectangle), having a width comparable with that of the nanowire, can be isolated and measured. The effect is called diffusive domain wall magnetoresistance because it is embedded in the AMR. The \AA range corresponds to one or a few atoms contact. In the antiferromagnetically aligned state an atomically abrupt domain wall forms across the contact giving rise to a significant MR. Due to atomic dimensions the transport is ballistic and hence, the scattering is of magnetic origin. The effect is known as ballistic magnetoresistance or ballistic DWMR. Part of this figure (the atomically abrupt domain wall) was taken from [24].

2.2 Anisotropic Magnetoresistance

When a current flows through a ferromagnetic material, its resistivity varies as function of the relative angle between the electric current and the magnetization direction. This phenomenon was discovered by Thomson in 1857 and was called anisotropic magnetoresistance (AMR). The importance of this phenomenon was recognized more than a century later in the 1970s when AMR of a few percent at room temperature was found in a number of alloys based on iron, cobalt, and nickel, which stimulated the development of AMR sensors for magnetic recording [25]. In this thesis the AMR effect is used to reveal the magnetization reversal processes in magnetic structures with constrictions.

Film studies show that thickness, grain size, and deposition parameters play a significant role in determining the percentage change in magnetoresistance. The sign of the effect may be either positive or negative, depending on the material: minority spin metals have a negative AMR (3d metals and alloys containing iridium), while majority spin systems show a positive AMR (3d metals and alloys) [25, 26].

Ferromagnetic metals exhibiting the AMR effect show maximum resistivity, when the current is parallel to the magnetization direction, ρ_{\parallel} , and minimum resistivity when the current is perpendicular to the magnetization direction, ρ_{\perp} . The magnitude of AMR can be defined by

$$AMR = \frac{\rho_{\parallel} - \rho_{\perp}}{\rho_{\perp}} \quad (2.1)$$

At intermediate angles, θ , between the current and magnetization direction, the resistivity of an AMR material is given by

$$\rho(\theta) = \rho_{\perp} + (\rho_{\parallel} - \rho_{\perp}) \cos^2 \theta \quad (2.2)$$

The AMR effect is a result of electron scattering at the level of atomic orbitals. The spin-orbit interaction leads to an energy splitting of d-orbitals. This causes a non-symmetric charge distribution, which results in anisotropic scattering of the 4s-conduction electrons.

Our cobalt films showed an AMR effect of 0.12%, which is low as compared with 1% or 2.5% reported in the literature for pure cobalt films [27, 28]. As already mentioned, these differences are due to film preparation conditions as well as measurement configuration. Details about our films are given in Sec. 4.2.

2.3 Magnetization reversal processes

As described in Sec. 2.1 and shown in Sec. 2.1.2, a ferromagnetic structure of μm size contains magnetic domains separated by domain walls. The

main source of this section is the textbook of D. Jiles [29], chapter 8. The interested reader may study the references therein. When a weak magnetic field is applied it is the moments within the domain walls which can most easily be rotated since the resulting directions of the moments within the walls are a fine balance between the exchange and anisotropy energies. The energy input by the field alters this balance, causing the moments to rotate. The domains aligned antiparallel to the field direction are at the bottom of a deep energy well caused by their mutual interaction through the exchange field. The net result is that the moments within the walls rotate slightly from the crystallographic easy axes into the field direction as the field is increased. This process is called domain wall motion.

Two types of wall motion can occur: wall displacement and wall bending. The strength of the domain wall pinning and the surface energy of the wall determine which of these occurs in a particular case. In practice, domain walls exhibit both bending and translation under the action of a magnetic field.

Walls with high surface energy compared to the pinning energy tend to remain planar. The movement of a planar domain wall is irreversible if the material is not sufficiently pure and has defects. In this case, the displacement of domain walls is impeded by regions of inhomogeneous strain which interacts via the magnetostriction with the magnetic moments to provide local energy barriers which the domain walls need to overcome. The strain is associated with dislocations and microstructural inhomogeneities such as the presence of particles of a second phase (magnetic inclusions) within the lattice material.

Walls with low surface energy compared to the pinning energy show a tendency to bend. Domain wall bending is a reversible process at low fields. The domain wall expands like an elastic membrane under the action of a magnetic field. When the field is removed the wall returns to its original position. Wall bending becomes irreversible once the domain wall is sufficiently deformed, so that the expansion continues without further increase of the field. The bending of the domain wall which begins as reversible can also become irreversible, if during this process the wall encounters further pinning sites, which prevent it from relaxing once the field is removed.

Simultaneously with wall motion, a slight rotation of the magnetic moments within a domain from the crystallographic easy axes toward the field direction appears. This results in a reversible rotation of the magnetic moments within a domain. Both, domain rotation and wall motion lead to a growth of domains, which are aligned favorably with the field and a consequent reduction in size of domains which are aligned in a direction opposing the field.

At intermediate to high fields there is an irreversible mechanism within the domain when the moments rotate from their original easy axis to the

easy axis closest to the field direction. This occurs when the field energy overcomes the anisotropy energy. In this case, once the magnetic moments within the domain have rotated into a different easy axis the moments remain within the potential well provided by the easy axis if the field is reduced.

At high fields the energy minimum of the easy axis closest to the field is perturbed by the field energy until the minimum lies in the field direction. This results in a reversible rotation of the moments into the field direction and hence a reversible change in magnetization at high fields. Finally at very high fields there is a reversible change in which the magnetic moments within the specimen, which is already a single domain, are aligned more closely with the field direction. This occurs, because the individual magnetic moments precess about the field direction due to thermal energy. This precession does not give any net moment in other directions, but does reduce the component of magnetization along the field direction. As the field strength increases the angle of precession is reduced. Similarly, if the temperature is lowered the angle of precession is reduced due to a reduction in thermal energy.

2.3.1 Anisotropic magnetoresistance and magnetization reversal

Considering the dependence of AMR on magnetization direction, local magnetization reversal events should clearly show up in the resistivity, if the system is confined. In the following, the correlation between AMR and magnetization reversal is discussed on the basis of the work of Brands *et al.* [30], in which a 30 nm thick cobalt nanowire with two different widths was characterized. The film was polycrystalline with the magnetic easy axis of the Co grains randomly distributed. Therefore, no magnetocrystalline anisotropy was involved, the shape anisotropy being the leading contribution. In *Fig. 2.6 a* an MFM image is shown for a wire with widths $w_1 = 55$ nm and $w_2 = 700$ nm after saturating the wire along its long axis (+y-direction), then applying a field of $B = -75$ mT in the opposite direction (-y) and returning to $B = 0$ mT. Thus, one obtains a remanent state where the wider part of the nanowire has switched, whereas the narrower has not. The corresponding MR behaviour for the whole wire and central part are presented in *Fig. 2.6 b* and *c*, respectively. After saturating the wire with a magnetic field applied longitudinally (+y-direction), the nanowire returns to a monodomain-like remanence state at zero magnetic field due to the shape anisotropy. In order to minimize the magnetostatic energy a C -state forms at the ends of the wire. The application of a small field in the opposite direction results in a domain wall motion and domain rotation (reversible processes) in that region. This leads to the generation of a small amount of transversal magnetization components perpendicular to

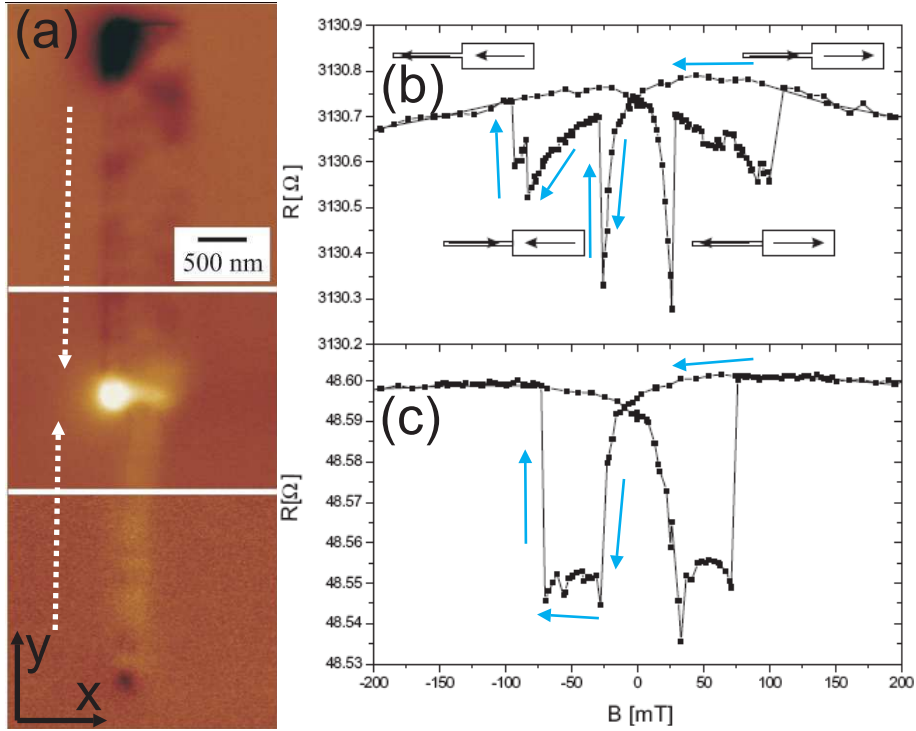


Figure 2.6: (a) MFM image of a cobalt nanowire with two different widths $w_1 = 55$ nm, $w_2 = 700$ nm. The image was taken at remanence after switching the wider wire by applying a magnetic field of 75 mT along the $+y$ -direction. The bright spot at the middle junction indicates a 180° domain wall. (b) Longitudinal resistance of a Pt-capped Co nanowire as a function of the applied magnetic field. The wire has a uniform thickness of 32 nm ($t_{Pt} = 2$ nm), length $l = 100$ μ m and two different widths $w_1 = 85$ nm, $w_2 = 700$ nm. (c) The resistance for the inner voltage leads of the same wire. The arrows represent the measurement procedure. Taken from [30].

the current which gives through the AMR effect a decrease in resistance. At a field of $B = -25$ mT the domain wall is depinned against the shape anisotropy and along with the reversed domain traverse the wider wire (irreversible processes). Both wires are now uniformly magnetized along their long axes, however, pointing against each other with a single 180° domain wall in between.

From $B = -25$ mT to $B = -80$ mT, the domain wall is pinned at the constriction since the wider wire is completely magnetized in the direction parallel to the magnetic field while the narrower wire has not yet switched. At $B = -80$ mT the domain wall is forced out of the constriction into the narrower part of the nanowire (irreversible process), but remains pinned there. The continuously decreasing resistance reflects the increasing amount of magnetization components in the narrower wire, which are oriented perpen-

pendicular to the current. The domain processes involved are again reversible domain wall motion and rotation. At a field of $B = -95$ mT the domain wall is depinned from the narrower wire accompanying its switching and the resistance returns to its original value. *Fig. 2.6 c* shows the resistance of the same wire as displayed in *b* measured however, at the inner voltage leads which have a width of about 500 nm and are only 900 nm apart. The pinning and depinning of the domain wall, both irreversible processes, are clearly visible. In-between the domain wall is trapped in the constriction.

2.4 Domain wall magnetoresistance - theoretical models

2.4.1 Diffusive regime

Because of the local modulation of magnetic moments inside the domain walls a resistance is generated in addition to that arising from the domains. This is known as domain wall resistance (DWR). This section deals with the diffusive regime of DWMR, which corresponds to a DW width in the nm range, similar to nanocontacts measured in this thesis (chapter 4). In order to study this effect a well-defined and simple domain state containing only one or many similar DWs is needed. This can be achieved either in thin films or nanostructures.

In the case of thin films dense domain patterns are formed at remanence, typically a stripe or labyrinth domain structure, with equal numbers of narrow domains magnetized along the two easy directions, in- or out-of the film plane. The magnetization subdivides until the associated energy cost of creating new walls exceeds the drop in magnetostatic energy. It is the high density of walls that makes thin films useful for DWR studies even if one may expect complex multidirectional wall structure which can prove problematic for the interpretation of transport data. A well-defined domain state can be achieved in many ways. The first one is to choose a material with a perpendicular magnetocrystalline anisotropy large enough to lift the magnetization vector out of the film plane [31]. Another option is to take advantage of the strong anisotropies present at interfaces between different magnetic metals and prepare multilayers with a high density of such interfaces which form a system with a strong out-of-plane anisotropy such as Co/Pt or Co/Pd [32]. To control the creation of in-plane magnetized domains one can use thickness modulation [33] or exchange bias effect [34].

In the case of nanostructures only one or a few domain walls are involved. The domain configuration is controlled by using shape-related magnetostatic effects. The most common geometry is that of a wire [35]. Some feature like a constriction or notch needs to be inserted into the wire in order to

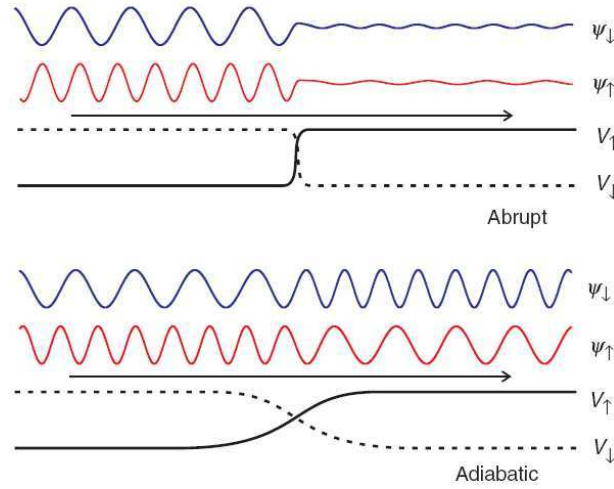


Figure 2.7: Spin-resolved potential profiles $V_{\uparrow,\downarrow}$ and resulting wavefunctions $\psi_{\uparrow,\downarrow}$ at abrupt and wide (adiabatic) domain walls. The wavefunctions are travelling from left to right. In the adiabatic case, the wavelengths of the two wavefunctions are exchanged, but the change in potential energy is slow enough that there is no change in the amplitude of the transmitted wave. When the wall is abrupt the wavelength change is accompanied by substantial reflection, resulting in a much lower transmitted amplitude (the reflected part of the wavefunction is not shown). This gives rise to domain wall resistance. Taken from [41].

locate and pin the wall. Since the wall surface energy is reduced when the wall enters the notch it forms an effective energy well in which the wall can reside. Wall nucleation generally takes place at the ends of the nanostructured wire, and is strongly affected by the details of the shape there [36]. By positioning a large pad at the end of the wire, a wall is reproducibly nucleated at the point where the pad joins onto the wire [23]. An alternative nucleation strategy is to use an on-top current-carrying wire to generate the localized magnetization reversal [37]. Once the domain wall is created, it can propagate in the nanowire by applying a magnetic field [37] or a current [38] and eventually be pinned at the constriction. Thus, DWR measurements on a single domain wall are possible.

In this thesis a nanoconstriction is lithographically defined between two wider electrodes. The size and shape of the two electrodes can be varied to separate their switching fields and thus to trap a single domain wall at the nanocontact during the magnetization reversal process.

The effect of domain walls on the resistance of a ferromagnetic metal is discussed below. From the theoretical point of view positive and negative contributions to the total resistance are predicted.

2.4.1.1 Positive domain wall magnetoresistance

The first attempt to calculate the electrical resistance of a domain wall is attributed to Cabrera and Falicov in 1974 [39, 40]. The basic idea of the so-called paramagnetic, spin-scattering model is the following. Electrons travelling in one domain will experience a different potential upon entering an oppositely magnetized domain since the band minimum will differ by the exchange energy splitting. The basis of their model was to calculate the reflection coefficients of the electronic wavefunctions at the potential steps that domain walls will represent within this picture, as sketched in *Fig. 2.7*. Two cases were considered: weak ($2\mu_B B_0 \ll E_F$) and strong ($2\mu_B B_0 \approx E_F$) exchange splitting of the bands, defined by comparing the exchange energy $2\mu_B B_0$ with the Fermi energy: B_0 is the molecular field, not a real magnetic field. In the case of weak splitting, the magnetoresistance of the wall is $\Delta\rho/\rho_{DW} \sim \exp(-\pi k_F D \zeta_F)$, where $\Delta\rho = \rho - \rho_{DW}$ with ρ_{DW} denoting the resistivity in the presence of a DW, D is the wall thickness and $\zeta_F = \mu_B B_0/E_F$. By definition, for weak splitting $\zeta_F < 1$, but the Fermi wavelength $2\pi/k_F$ is orders of magnitude smaller than D for most systems. This implies the wall resistance to be vanishingly small, because of the exponential dependence. For the example of iron, $2\pi/k_F$ is only 1-2Å, depending on the band, while the wall thickness is some thousands of Å. This leads to a value of $\Delta\rho/\rho_{DW} \sim 10^{-4}$. The physical reason for this is that waves are only scattered strongly by potential steps that are abrupt on the scale of the wavelength of that wave, as sketched in *Fig. 2.7*. For strong splitting ($\zeta_F \approx 1$), it was found to be necessary to restrict the calculation to a very narrow wall, assuming $k_F D \ll 1$. In practice, this means atomic abruptness. In this case a variable $v = k_{F\uparrow}/k_{F\downarrow} = (g(E_{F\uparrow}/E_{F\downarrow}))^{1/3}$, which is connected to the polarization P of a ferromagnet [41] determines the DW resistance. The obvious relationship with the Stearns definition of polarization, $P = (k_{F\uparrow} - k_{F\downarrow})/(k_{F\uparrow} + k_{F\downarrow})$, emphasizes that the theory is essentially one describing tunnelling between one domain and the next. The DW resistance vanishes as $v \rightarrow 1$, while for $v \rightarrow \infty$ (equivalent to $P \rightarrow 1$), the material becomes half-metallic and the wall resistance also tends towards an infinite value.

In 1978 Berger suggested that domain walls are too thick to “scatter” electrons appreciably [42]. Because the conduction electron wavelength is much shorter than the domain-wall width, the electronic spin follows the local magnetization adiabatically and gradually tilts as it traverses the wall. Berger also discussed the possible torques exerted on the moments within the wall (domain wall drag effect), which are proportional to the polarization of the current. This work represents the first suggestion that the interaction of a current with a magnetic domain wall can be used to measure the degree of spin-polarization of that current and the transfer torque.

Another model of DWR was given by Viret *et al.* in 1996 [43]. It is a semi-classical model based on the pseudo-Larmor precession of the electron spin around the rotating exchange field in a wall (see *Fig. 2.8 a*). This precession will allow the spin direction to track the local exchange field direction to a greater or lesser extent depending on the timescales of the precession and the wall rotation. As the spins deviate away from the local exchange field while crossing the domain wall an additional resistance, given by

$$\frac{\Delta R}{R} = \frac{2P}{(1-P)^2} (1 - \langle \cos \theta_S \rangle) \quad (2.3)$$

will be measured per domain wall, where P is the polarization of the current and θ_S is the angular deviation between the electron spin and the scattering center (local magnetic moment). As the electron traverses a wall of thickness D the exchange field will rotate around it with an angular frequency $\omega_{wall} = \pi v_F / D$. Meanwhile, the Larmor frequency of the spin in the canted exchange field is given by $\omega_{Larmor} = J / \hbar$, with J the exchange energy. The maximum angle θ_0 can be estimated as the angle the local moment rotates during half a Larmor precession $\theta_0 = (2\pi \hbar v_F) / (E_{exchange} D)$. Considering $\langle \cos \theta_S \rangle = \cos^2 \theta_0$ and θ_0 being small ($\omega_{Larmor} < \omega_{wall}$), so that $\sin \theta_0 \approx \theta_0$, the magnetoresistance within the wall can be rewritten as

$$\frac{\Delta R}{R} = \frac{2P}{(1-P)^2} \left(\frac{2\pi \hbar v_F}{E_{exchange}} \right)^2 \frac{1}{D^2} \quad (2.4)$$

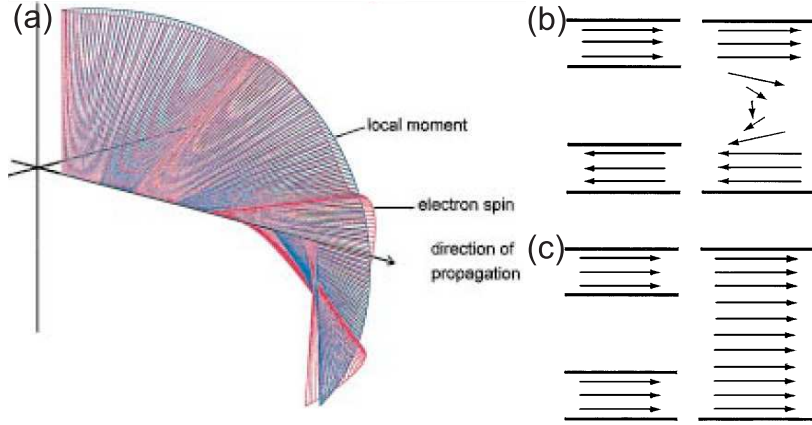


Figure 2.8: **(Left)** (a) The spin precessional behavior for a cobalt domain wall. The spin orientation is shown in red; the local exchange field variation is shown in blue. **(Right)** Schematic illustration of the similarity between the magnetic geometry of a GMR trilayer and a ferromagnetic domain wall. (b) The relationship between an antiferromagnetically aligned trilayer and the presence of a domain wall. (c) The trilayer in its ferromagnetically aligned state, which corresponds to the absence of the domain wall in the ferromagnet. Taken from [44].

It is evident from this expression that thinner domain walls make a more significant contribution to the magnetoresistance. In fact, the thinner the domain wall, the more the system approximates to that of a GMR layer structure in which the change in the spin orientation is truly “sudden” (see *Fig. 2.8 b* and *c*). In practice the entire sample, both domains and walls, is measured. In order to include the domains it is necessary to multiply this result by D/d , where d is the average domain size. Viret *et al.* studied ~ 30 nm thick Co and Ni polycrystalline films on glass. The average domain wall width was 15 nm for Co and 100 nm for Ni. Using Eq. 2.4 a spin-scattering magnetoresistance $(\Delta R/R)_{Co} = 3 \times 10^{-4}$ and $(\Delta R/R)_{Ni} = 4 \times 10^{-5}$ were calculated which compare to the experimental value of $(\Delta R/R)_{Co} = 2 \times 10^{-4}$ and $(\Delta R/R)_{Ni} = 3 \times 10^{-5}$. The main message of this work was that even for thicker domain walls the process of passing a wall is not purely adiabatic.

The following year, Levy and Zhang published a fully quantum mechanical model to explain the resistivity due to domain wall scattering [45]. They used the same Hamiltonian that was used to describe the GMR in magnetic multilayers. It consists of two parts: a spin dependent electronic structure part, whose eigenstates are referred to as the spin-dependent band structures of ferromagnetic metals and a scattering part due to defects present in the material. When a domain wall is present (magnetization is not collinear) an extra term appears in the Hamiltonian which represents the perturbation of the wavefunctions due to the twisting of the magnetization in the wall. The Hamiltonian for the wall does not have pure spin eigenstates as the rotating exchange field in the wall produces an admixture of states with opposite spins. The impurity potential therefore scatters electrons from one eigenstate to another and thereby mixes the two current channels. This is the source of extra resistance in the wall. The application of a field that is large enough to saturate the magnetization erases domains and the walls separating them. It produces a homogeneous sample whose eigenstates are pure spin states. The impurity potential does not scatter electrons between states of different spin so that the spin current channels are independent of one another.

Two basic geometries were considered, named after the corresponding geometries for GMR measurements: current in wall (CIW), where the current density lies in the wall plane; and current perpendicular to the wall (CPW), where the current flow is normal to the wall. The magnetoresistance ratios for the two geometries are given by:

$$MR_{CIW} = \frac{\rho_{CIW} - \rho_0}{\rho_0} = \frac{\xi^2 (\rho_{\uparrow} - \rho_{\downarrow})^2}{5 \rho_{\uparrow} \rho_{\downarrow}} \quad (2.5)$$

and

$$MR_{CPW} = \frac{\rho_{CPW} - \rho_0}{\rho_0} = MR_{CIW} \left[3 + \frac{10\sqrt{\rho_{\uparrow}\rho_{\downarrow}}}{\rho_{\uparrow} - \rho_{\downarrow}} \right] \quad (2.6)$$

where $\xi = (\pi\hbar^2 k_F)/(4mDJ)$ represents the departure from adiabaticity and is the spin-mixing parameter, ρ_\uparrow and ρ_\downarrow are the spin-resolved resistivities of the metal and $\rho_0^{-1} = \rho_\uparrow^{-1} + \rho_\downarrow^{-1}$ is the magnetically saturated resistivity. If the wall rotation is slow enough that perfect adiabaticity is maintained then the spin channels remain completely decoupled. It was shown in [45] that the formulae depend only on the spin-asymmetry ratio $\alpha = \rho_\downarrow/\rho_\uparrow$ which gives the polarization of the current, and $\xi \sim 1/D^2$. To estimate the MR due to the walls, commonly accepted values for $k_F = 1\text{\AA}^{-1}$, $J = 0.5\text{eV}$, and $\rho_0^\uparrow/\rho_0^\downarrow = 5 - 20$ (this range holds for Co, Fe and Ni, and for a variety of impurities at room and low temperatures) were used. Considering a 15 nm thick cobalt wall, $MR_{CIW} = 0.3\% - 1.8\%$ and $MR_{CPW} = 2\% - 11\%$ were estimated at room temperature. The conclusion of this work was that the mistracking is not a source of scattering or resistance; rather the impurity scattering produces the resistance.

Both the Levy and Zhang quantum model and the Viret *et al.* semiclassical model share some important features. In both cases, the MR ratio is independent of the overall scattering rate. It is the degree of spin-polarization of the current that determines the size of the MR effect. Also in both cases the MR ratio within the wall is inversely proportional to the square of the wall thickness, so that narrow walls are required to obtain a large MR. The length scale is set not by the randomization of the momentum of the electrons by scattering, since the scattering rate is not important. Hence there is no need for the electrons to traverse the wall in a ballistic manner, they may scatter many times. It is set instead by the rate at which the spin of the electrons can relax to track the changing magnetization direction in the sample.

2.4.1.2 Negative domain wall magnetoresistance

There also are theories which predict that the presence of a wall will increase the resistance. Tataru and Fukuyama treated the scattering of the conduction electron by a domain wall in a wire of ferromagnetic metal within the framework of linear response theory [46]. They investigated the effect of the wall on quantum transport properties in the disordered system, where the interference effect becomes important. The wall suppresses the interference between the electrons, and hence decreases the resistance in the weakly localized regime. This is predicted to be a measurable effect because the quantum part of the resistance was found to dominate over the classical Boltzmann part. Another interesting aspect presented in [46] is the appearance of conductance fluctuations due to small motions of the wall. This effect has to be carefully observed by means of transport and imaging measurements, because the nucleation or annihilation of a wall can produce similar jumps in resistance.

An alternative approach was given by van Gorkom, Brataas and Bauer [47]. They estimated the change in resistivity due to a change in magnetization within the Drude formula. The Drude resistivity of a single-domain ferromagnet in the two-band Stoner model is given by

$$\rho = \frac{m}{e^2} \frac{1}{n_{\uparrow}\tau_{\uparrow} + n_{\downarrow}\tau_{\downarrow}} \quad (2.7)$$

where m is the mass of the electron, e is the charge of an electron, $n_{\uparrow}(n_{\downarrow})$ is the density of spin-up (spin-down) electrons, and $\tau_{\uparrow}(\tau_{\downarrow})$ is the scattering relaxation time for the spin-up (spin-down) electrons. A domain wall causes a redistribution of the electrons between the spin-up and spin-down bands and thus modifies the resistivity when $\tau_{\uparrow} \neq \tau_{\downarrow}$. With $n = n_{\uparrow} + n_{\downarrow}$, $n_{\uparrow,\downarrow} = n_0^{\uparrow,\downarrow} + \delta n_{\uparrow,\downarrow}$, and $\delta n_{\uparrow} = -\delta n_{\downarrow}$, the change in resistivity is found to be

$$\delta\rho \approx -\rho_0^2 \frac{e^2}{m} \delta n_{\uparrow} (\tau_{\uparrow} - \tau_{\downarrow}) \quad (2.8)$$

where ρ_0 is the resistivity of a single-domain ferromagnet. In this model a *negative* as well as a *positive* domain wall resistance is possible, depending on the difference of scattering relaxation times. $\tau_{\uparrow,\downarrow}$ depend to a large extent on the type of impurities present in the sample [48] and slight stoichiometry and morphological variations as suggested in [49]. These predictions for the DW resistance can be experimentally tested by intentionally doping samples with different impurities and measuring the DW resistance as a function of type and concentration.

2.4.2 Ballistic regime

Although the ballistic DWMR effect was not found experimentally in this thesis due to the size of the measured nanocontacts, this regime is discussed in order to give to the reader a more complete picture of the spin-dependent transport in nanocontacts down to the atomic scale. While the phenomenon of a diffusive DWR has been theoretically (Sec. 2.4.1) and experimentally (Sec. 2.5.2) established beyond reasonable doubt, that of a ballistic effect is far more problematic to establish. This is mainly due to the extreme difficulty of characterizing the nanoscale devices that are required - since most magnets are metals, the Fermi wavelength λ_F is typically only $\sim 1\text{\AA}$, and the devices must hence consist of a few atoms to be of the appropriate size. Moreover, magnetic metals are not free electron-like, and so the mean free path l is at best only tens of \AA . This means that to form a truly ballistic contact the device size must be of atomic scale. Such devices are experimentally difficult to deal with in several ways: firstly they are hard to fabricate in a reproducible manner; they are almost impossible to characterize structurally or magnetically; and finally they are unstable

with time-varying properties and have rather short lifetimes of at best a few hours.

The conventional definition of a ballistic device is one where the dimensions are smaller than the mean free path, so that it is band structure and geometric effects, rather than scattering, that determine the conductance. The simplest definition for the ballistic traversal of a wall might then be that the electrons traverse the wall without scattering, so one condition might be $D \ll l$. However, the mean free path does not explicitly enter the formulae for the diffusive DWMR, Eq. 2.4, 2.5 and 2.6. The electron spins may still have a chance to dephase as the wall is crossed and the condition for preventing this is that $D \ll \hbar v_F / J$. More extreme is the Cabrera-Falicov limit, where the wall is thin enough to reflect an electron wavefunction, here the condition is $D \ll 2\pi / k_F$.

It is interesting to ask why in the case of a nanocontact one can predict a huge MR, but in the case of a extended wall the MR does not exceed a few tens of percent for reasonable values of spin-polarization. The answer lies in the fact that for a laterally extended system - be it domain wall, tunnel barrier, or interface - all available channels for conduction are open: that is, every value of k_{\parallel} less than k_F in the 2D Brillouin zone can contribute to the conduction. In the nanocontact case this does not apply and only a very small number of channels are open - perhaps only one. It is the polarization of these few states that is important, rather than the average over the full 2D zone. Since there are few states, there is a good chance that the spin polarization of these happens to be quite high. Thus, the number of open conduction channels with different transmission probabilities and certain degrees of spin polarization along with the different degrees of spin-flipping introduced by the wall can explain the variability in experimental results [50].

It has been shown theoretically that the spin polarization can be also changed by non-magnetic atoms at the nanocontact [51]. It is expected that a few-atoms Ni nanocontact does not remain chemically pure under ambient conditions in air, but it gets oxidized. This can give rise to conduction through spin-polarized oxygen p states, which were treated using the Kubo formula [52] to calculate the conductance between two semi-infinite Ni leads each coated with an adlayer of O atoms. Each O atom was found to develop a rather large magnetic moment of $1.4 \mu_B$, meaning that the conducting states are highly spin-polarized. Magnetoconductance ratios of hundreds of percent were found for this structure. Similar adlayers of Cl, S, or C were shown not to be polarized and no MR was found in these cases.

An expression for the magnetoconductance $\Delta G/G$ was given in [53] in terms only of the Fermi wavevectors $k_{F\uparrow}$ and $k_{F\downarrow}$ and the domain wall

thickness D :

$$\frac{\Delta G}{G} = \frac{\pi^2}{8} \frac{P^2}{1 - P^2} \left[\frac{1}{\cosh^2 \pi k_F D} + \frac{1}{\cosh^2 \pi k_F P D} \right], \quad (2.9)$$

where P is defined in terms of the spin-resolved Fermi wavevectors, $P = (k_{F\uparrow} - k_{F\downarrow}) / (k_{F\uparrow} + k_{F\downarrow})$, as in the Stearns tunnelling model, and $k_F = (k_{F\uparrow} + k_{F\downarrow}) / 2$ is the spin-averaged Fermi vector. The similarity of the central term, $P^2 / (1 - P^2)$, to the Julliere tunnelling formula (Eq. 5 in [41]) underlines the similarity of the physics in this model to the tunnelling process between the two magnetic electrodes.

There are theoretical predictions of very large DWMR through a magnetic point contact containing an atomically abrupt domain wall. Imamura *et al.* [54] showed that the spin precession of a conduction electron is forbidden in such an atomic scale DW and the sequence of quantized conductances depends on the relative orientation of magnetizations between left and right electrodes. The magnetoresistance is strongly enhanced for the narrow point contact reaching 1800% and oscillates with the conductance. Tagirov *et al.* [55] found MR ratios up to around 1000% in the ballistic limit and 450% in the diffusive case. All these predictions remain to be confirmed convincingly by performing the characterization of both the atomic and magnetic configurations on these very fragile systems.

2.5 Nanocontacts: Experimental situation

2.5.1 Large domain wall magnetoresistance - ballistic limit

In the past few years there has been a substantial research effort on magnetic nanocontacts. This effort was started with the claim by Garcia *et al.* of the observation of a MR of 200% in mechanically formed point contacts made by touching two Ni wires [56]. The effect, named ballistic magnetoresistance (BMR), was observed at room temperature and fields of only a few Oe were required to switch between the two resistance states. The effect was only seen for contacts with a conductance of a few times the quantum unit of conductance $G = 2e^2/h$, implying that the contact area is little more than a few atoms. This result attracted a large number of other groups to look at this effect. The effect was interpreted as the trapping of a nanometer sharp domain wall in the nanocontact (as suggested by Bruno [20]) at low fields, leading to a modification of the transmission coefficients of the various spin-polarized channels conducting the carriers through the constriction. No effect was observed when one, or both, Ni wires were replaced with Cu.

While in the original paper the conductance was always much lower when the domain wall was present, with the wires oppositely magnetized, a full MR loop was found to display either a positive or a negative effect [57].

These new experiments were performed on electrodeposited nanocontacts across nickel wires in a “T” geometry. The resistance of these nanocontacts was in the range of 1 to 500 Ω , corresponding to a diameter of 3 - 100 nm. The same contact was reported to show both positive and negative magnetoresistance effects (25% at room temperature) depending on the sequence of the applied magnetic fields and current pulses. The current pulses were thought to modify the local magnetic domain configuration in the electrodes in the vicinity of the nanocontact region, and various possible domain states were proposed that could explain the results. The mechanism for this to take place was suggested to be either a spin-transfer effect or a simple interaction with the strong Oersted field produced by these high current density pulses. The same electrochemical technique and “T” configuration have been used by Hua and Chopra to form Ni nanocontacts with claims of magnetoresistance of over 3000% (11 nm estimated diameter) [58] and 100000% (few nm to few tens of nm estimated diameter) [59], with the saturated state being the high resistance one in most samples. The zero-field resistance was in the range of 8 to 20 Ω . An experimental observation of the nanocontact [59] showed that it is made of whiskers with nano-constrictions, pointing toward a picture of several ballistic, quasiballistic, and diffusive conductors acting in parallel and series to give rise to the observed large effect, instead of the ideally assumed single, monolithic nanocontact.

These results are still hotly debated, raising serious doubt about the origin of the measured BMR, but without ruling out the possibility of true BMR of electronic origin in nanocontacts. Egelhoff *et al.* [60] have carried out a wide-ranging and careful series of experiments on the geometries, which had been used for BMR measurements, finding that whenever a large MR was observed it was caused by artifacts involving magnetostrictive or magnetostatic forces making and breaking the contact. Also, magnetic nanoparticles created in the contact region during the fabrication using a plating process can then move under the application of a field and cause large resistance changes [61]. A small amount of plating solution was extracted from the vicinity of the growth region and placed in the gap of a new unused pair of electrodes. Similar, BMR-like effects, were found. This group went on to construct an extremely well-controlled electrodeposition environment, where the contact can be stabilized and maintained at a very well-defined resistance, and MR measurements made *in situ* [62]. No BMR of any magnitude was detected for Ni contacts in any field orientation, as was also reported by Yang *et al.* in [63].

To address some of the criticisms of their earlier work, Garcia *et al.* formed pseudo-planar devices, showing some very large effects initially, but these soon vanished after field cycling [64]. The initial effects were of similar size for both Ni and NiFe contacts, although the effect of magnetostriction should be much reduced in the latter, if good quality permalloy contacts are

formed. One interesting statement in this paper is: "...This corresponds to the second loop taken; the first one exhibited 1 000 000% MR! We do not understand this and maybe it is an illusion..."

Most recently, the group of Chopra *et al.* continued to stress that their measured effects are genuine, and claim the absence of magnetostriction-related artifacts in Ni and Co contacts, showing large MR in the G_0 conductance limit [65, 24]. In their paper on Ni nanocontacts [65] they argue that at G_0 even a sub-Å motion of the contact would result in a total loss of conductance. However, the half MR traces that they measure are noisy and rather irreproducible. On the other hand, the complete MR curves on Co atomic point contacts in [24] show clear features, which occur at particular values of applied field. The presence of an abrupt domain wall across the contact, acting as a "quantum" spin-valve, causes the number or probability of transmitting channels to differ between antiferromagnetically and ferromagnetically aligned states, giving rise to a stepwise change in magnetoresistance. Another interesting aspect of these quantum contacts is the oscillatory nature of magnetoresistance as a function of contact size. The oscillations arise from a sudden change in the number of open conductance channels at certain sizes of the constriction.

As with Tunneling Magnetoresistance (TMR), one will anticipate the highest possible MR when half-metallic electrodes are used. Values up to 8000% for magnetite (Fe_3O_4) and 100% for $\text{La}_{0.7}\text{Sr}_{0.3}\text{MnO}_3$ in single and multiple nanoconstrictions 20 to 50 nm wide were found and interpreted within a model for domain-wall magnetoresistance [66]. Another half-metal which exhibited MR up to 80% at room temperature was $\text{Co}_2\text{Cr}_{0.6}\text{Fe}_{0.4}\text{Al}$ [67].

Large MR values of 2000% were measured in a (Ga,Mn)As double constriction patterned into a wire by electron beam lithography. The discovery of such a large effect in the new class of ferromagnetic semiconductor materials has been explained not by a DWR effect, but by TMR [68].

2.5.2 Small domain wall magnetoresistance - diffusive limit

In this section an overview of the experimental work done on diffusive nanocontacts is presented. If BMR is ever to be employed in a real device structure it will need to be implemented in a planar technology. In general, the formation of atomic scale structures using conventional lithography is not possible, even with the high resolution electron and focussed ion beam tools available today. Florez *et al.* have formed junctions of NiFe down to sizes of about 15 nm, which were shown to trap domain walls using MFM [49]. Drops in resistance, when scaled to the size of the wall, indicated that the presence of a wall in a contact actually increased the conductance by a few percent in these devices, although they claim that one single de-

vice showed a drop in conductance of the same order of magnitude. The presence of negative or positive DW contributions was explained using the model of Gorkom *et al.* (see Sec. 2.4.1) implying slight stoichiometry and morphological variations in the nanocontact.

On the other hand, several sets of well-controlled “T”-junction devices have not found any large MR effects. Stable Co constrictions of nm scale only show effects of the size that might be anticipated from AMR, all below 1% [69] in spite of a diligent search as will also be shown in this thesis. Ozatay *et al.* [70] formed Ni-Ni contacts in a membrane nanohole with an exchange biased bottom layer using FeMn. No effect larger than a fraction of a percent was found, although point contact spectroscopy revealed that the conduction was at least partly ballistic. Contact diameters, estimated from the junction resistances using the Sharvin formula [70], were as small as 3 nm.

The group of Viret *et al.* have studied truly atomic scale contacts, and demonstrated conductance through a single atom of Ni [71]. These samples were mechanical break junctions showing clear conductance quantization, measured at low temperatures. The junctions were formed in an inert helium atmosphere. Complicated MR responses of a few tens of percent were found, composed of smoothly varying curves, with some discrete jumps at largely reproducible field values. The field direction dependence indicated that this is an effect with the same features as the AMR, and could be interpreted in terms of the spin-orbit coupling in the atoms within the contact. In a follow-up paper they described, how to account for and minimize magnetostrictive effects in these junctions [72]. Since orbital moments are generally found to be enhanced in low-dimensional systems, one might expect that their effects on the transport would also be augmented. Indeed, a so-called giant anisotropic MR has recently been detected in an Fe atomic contact by this group in both the atomic contact and tunnelling regimes [73]. A theoretical description of the so-called “ballistic anisotropic magnetoresistance” has been given by Velev *et al.* [74].

However, there are claims of modest success in the fabrication of planar junctions. Khizroev *et al.* demonstrated MR of 18% at room temperature for a focused-ion-beam-fabricated NiFe nanoconstriction with critical dimensions of 35 nm. The extra resistance is attributed to a nonadiabatic spin transport through a domain wall confined in the junction [75]. A similar MR value was measured on Ni nanocontacts whose sizes were progressively decreased by electromigration. An evolution of the magnetoresistance from AMR in wide junctions, to an enhanced AMR in few-channel wires, to TMR in tunnel junctions, with large sample-to-sample variability in the shapes and signs of the TMR was observed. No observed magnetoresistances were larger than those expected from the known polarization of Ni. The mesoscopic variation in MR indicates that the local junction environment can

have a strong effect on the spin of the tunneling carriers [76].

It is clear that the problem of domain wall resistance has attracted a lot of interest, both from theoretical and experimental points of view. The predictions are diverse and it is not clear if the contribution is positive or negative. More experiments are necessary to discriminate between models.

2.6 Micromagnetic calculations

To understand the measured MR signals as a function of external field, the magnetization reversal process in Co nanocontacts has to be known. For this propose, micromagnetic calculations were performed using the Object Oriented MicroMagnetic Framework public code (OOMMF) from National Institute of Standards and Technology (NIST). It works by dividing the sample into 2D or 3D grids of small cuboids [77]. The size of the computational cell needs to be small enough to accurately represent the smallest magnetic object in the sample. There are two quantities which determine the maximum size of the computational cell: the exchange length $l_{exch} = \sqrt{A/K}$ which is proportional to the domain wall width and the demagnetizing length $l_D = \sqrt{2A/\mu_0 M_s^2}$ or the width of an isolated Bloch line. The parameters involved are: A - the exchange constant (exchange stiffness), K - anisotropy constant and M_s - the saturation magnetization. The domains or walls are not postulated but arise from boundary conditions and energy considerations. The concept is based on the fact that the magnitude of the magnetization $\vec{M} = M_s \vec{m}$ (M_s is the saturation magnetization and $\vec{m}(x, y, z)$ is the magnetization unit vector representing the magnetization direction) is constant for each cell but its direction smoothly changes with position from cell to cell. Thus, a continuum representation is used instead of discrete magnetic moments located at the sites of the atoms in the crystal lattice.

One then proceeds by integrating the Landau-Lifshitz-Gilbert (LLG) equation [77] forward in time for each element, taking into account the interactions between all the elements, until some convergence criterion is reached. The LLG equation is the equation of motion for the magnetization \vec{M} and has the following form:

$$\frac{d\vec{M}}{dt} = \frac{-\gamma}{1 + \alpha^2} \vec{M} \times \vec{H}_{eff} - \frac{\gamma\alpha}{M_s(1 + \alpha^2)} \vec{M} \times (\vec{M} \times \vec{H}_{eff}), \quad (2.10)$$

where γ is the gyromagnetic ratio ($m/(As)$), α is the phenomenological damping coefficient and \vec{H}_{eff} (A/m) is the local effective magnetic field obtained by taking the derivative of the total energy (J/m^3) at a given cell with respect to the local \vec{M} .

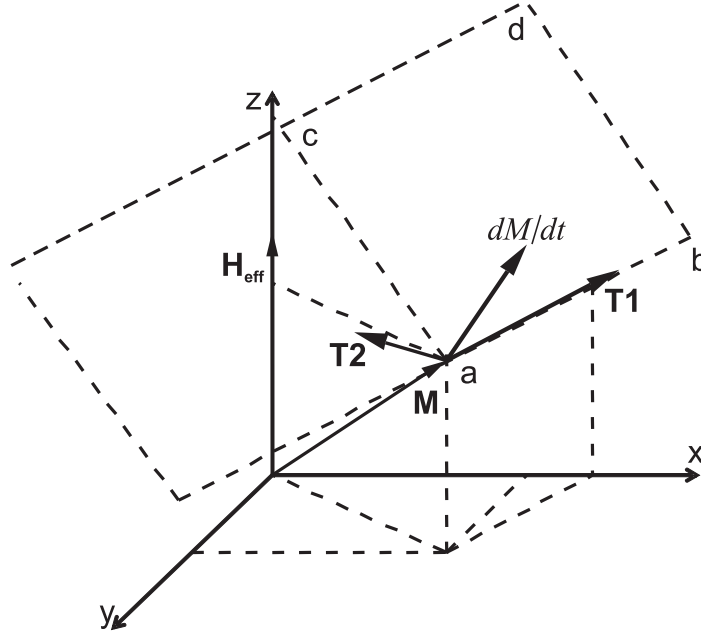


Figure 2.9: The different torques experienced by the precessing magnetization \vec{M} in an effective field \vec{H}_{eff} , related to the two terms in the Landau-Lifschitz equation (Eq. 2.10). The first term, $\propto -\vec{M} \times \vec{H}_{eff}$, induces the precession of the magnetization \vec{M} around the effective field \vec{H}_{eff} . The second term, $\propto -\vec{M} \times (\vec{M} \times \vec{H}_{eff})$, gives rise to the damping torque that causes the moment to eventually settle pointing along the effective field direction.

The vectors in Eq. 2.10 are represented in *Fig. 2.9*: the magnetization \vec{M} , its time derivative $d\vec{M}/dt$, the torque $\vec{T}_1 \propto -\vec{M} \times \vec{H}_{eff}$ and the damping term $\vec{T}_2 \propto -\vec{M} \times (\vec{M} \times \vec{H}_{eff})$. The torque \vec{T}_1 is perpendicular to the plane containing \vec{M} and \vec{H}_{eff} and causes an infinite precession of magnetization around \vec{H}_{eff} . The time derivative term $d\vec{M}/dt$ lies in the plane (abcd) perpendicular to \vec{M} . The damping term \vec{T}_2 is perpendicular to the plane determined by the vectors \vec{M} and $d\vec{M}/dt$. It causes energy dissipation, driving the system into an equilibrium state. The equilibrium state is reached when the magnetization at any point aligns along the local effective field, within a specified tolerance margin.

An externally applied field contributes to the effective field, driving the motion of the magnetic moments. The exchange, anisotropy and demagnetizing interactions are also included into this effective field. To calculate \vec{H}_{eff} the total energy density E at a given cell is needed. The various energy densities which sum together to give the total energy E are [41]:

$$E_{exch} = \frac{A}{M_s^2} (|\nabla M_x|^2 + |\nabla M_y|^2 + |\nabla M_z|^2), \quad (2.11)$$

$$E_{anis-cubic} = \frac{K_{c1}}{M_s^4} (M_x^2 M_y^2 + M_y^2 M_z^2 + M_z^2 M_x^2), E_{anis-uniaxial} = K_u \sin \theta, \quad (2.12)$$

$$E_{demag} = \frac{1}{2} \frac{\mu_0}{4\pi} \vec{M}(\vec{r}) \cdot \left(\int_V \nabla \cdot \vec{M}(\vec{r}') \frac{\vec{r} - \vec{r}'}{|\vec{r} - \vec{r}'|^3} d^3 r' - \int_S \widehat{\vec{n}} \cdot \vec{M}(\vec{r}') \frac{\vec{r} - \vec{r}'}{|\vec{r} - \vec{r}'|^3} d^2 r' \right), \quad (2.13)$$

$$E_{Zeeman} = -\mu_0 \vec{M} \vec{H}. \quad (2.14)$$

The first term E_{exch} shows that any change in the direction of \vec{M} with respect to the parallel alignment of the local magnetic moments results in an energy penalty. A is the exchange stiffness defined as $(n/a)JS^2$ where n is the number of atoms per unit cell, a the distance between neighboring planes (lattice constant), J is the value of the exchange integral having quantum mechanical origin and S is the spin.

The second term E_{anis} takes into account the interaction of the magnetization with the crystal lattice. This term also includes surface anisotropy. It results from spin-orbit interaction and depends on the crystal structure. It causes the preferred alignment of the magnetization into certain directions with respect to the crystallographic equivalent easy axes. For cubic materials like, e.g., iron and nickel the anisotropy energy density is given by the first formula in Eq. 2.12 where K_{c1} is the cubic anisotropy constant and \vec{M}_x , \vec{M}_y , \vec{M}_z are the magnetization components along the cubic axis. The high-order terms are neglected. For hexagonal materials like cobalt the second formula in Eq. 2.12 applies. K_u is the hexagonal (uniaxial) anisotropy constant and θ is the angle between magnetization \vec{M} and the main axis (easy axis) of hexagonal crystal.

The magnetostatic (demagnetization) energy density E_{demag} is the sum of long-range dipole-dipole interactions with a factor $1/2$ to avoid double counting. Eq. 2.13 shows that the E_{demag} at any cell is a spatial integral of the magnetization \vec{M} over the entire computational box. In a numerical calculation for a computational box containing n unit cells, this means that the demagnetizing energy term includes the interactions of every cell with all the others, thus involving n^2 terms, whereas n terms are required for computing the exchange and anisotropy energy terms only. Therefore, computing the magnetostatic energy takes most of the computer time in a typical micromagnetic calculation. The demagnetizing energy term also requires the most computer memory. It effectively restricts the size of the sample to below the micrometer region when using a reasonable cell size. As it was already mentioned in Sec. 2.1.1 the demagnetization forces are responsible for the domain formation.

Finally the Zeeman energy density E_{Zeeman} contains the interaction with an external magnetic field. The applied field can be uniform or non-uniform. For a uniform external field this energy depends only on the average magnetization and not on the particular domain structure.

The effective field is then defined by:

$$\vec{H}_{eff} = -\frac{1}{\mu_0} \frac{\partial E}{\partial \vec{M}} \quad (2.15)$$

Details about the calculation of the energy density terms, the integration of Landau-Lifshitz-Gilbert equation, the method used to control the integration error are given in [77].

For a given applied field, the numeric integration continues until a control point is reached. A control point event may be raised by the iteration count, elapsed simulation time, or by the maximum value of $|\vec{M} \times \vec{H}_{eff}|/M_s^2$ dropping below a specified control point - torque value. For the simulations of Co samples presented in this thesis a torque smaller than 10^{-6} for all the spins was used to test convergence to an equilibrium state. In order to obtain reliable results a base calculation cell of 3 nm was used. Since the real structures are in the μm range the micromagnetic simulations were carried out on the area around the nanocontact preserving its real dimensions and shape. The other parameters used in the calculation were: $M_s = 1.4 \times 10^6$ A/m, $A = 30 \times 10^{-12}$ J/m, $K_u = 520 \times 10^3$ J/m³, $\gamma = 2.21 \times 10^5$ m/As, and $\alpha = 0.5$ which allows the solver to converge in a reasonable number of iterations. The anisotropy direction was randomly varied in the xy-plane to simulate a polycrystalline material. The results are shown and discussed in chapter 4.

Chapter 3

Experimental techniques

In this chapter sample fabrication and experimental techniques are described in detail. In order to understand spin-dependent transport in magnetic nanocontacts a method to vary their size and geometry in a controlled manner is needed. We developed a new fabrication method by combining the proximity effect of electron beam lithography with a special layout design. In this way nanocontacts with widths ranging from 11 nm to 170 nm were routinely obtained. Details of sample preparation are given in the first section (Sec. 3.1). Then follows a description of the measurement setup along with the types of measurements used for electrical characterization (Sec. 3.2). Since the direct observation of the magnetization distribution during the reversal process in individual nanostructures is hard to achieve, we used magnetoresistance measurements as an indirect sensing tool based on anisotropic magnetoresistance effect. To further characterize the magnetic properties of the nanostructures we investigate the remanent magnetic domain configuration using Magnetic Force Microscopy (MFM). The third section (Sec. 3.3) explains the principle of MFM. Special attention is paid to the possible influence of the magnetic tip on the magnetic structure of the sample due to the scanning procedure specific to our microscope.

3.1 Sample preparation

The substrates used in this thesis consists of n-type heavily doped (100) silicon (Si) with a resistivity of $0.01 \Omega cm$ and a top layer of silicon dioxide (SiO_2) with a thickness of 100 nm. The highly doped Si can serve as a back gate, if a voltage is applied to it. After cutting the 4-inch silicon wafers into square pieces of 10 mm, the sample is transferred to the clean room where it undergoes cleaning and processing. Sample production consists mainly of an optical and two electron-beam lithographic steps.

Lithography is commonly used to manufacture devices on scales smaller than a micrometer. Light, electrons, X-rays and protons can be used to

print patterns on a sensitive layer. The methods used for the experiments presented in this thesis are discussed below.

3.1.1 Optical lithography

In optical lithography ultraviolet light ($\lambda = 250 \text{ nm}$) is used to expose a photosensitive emulsion (or resist) through a photomask. For this a Mask Aligner MA-6 from Süss coupled with a high-pressure mercury lamp with 7 mW/cm^2 maximum power were used. One cell of the photomask is shown in *Fig. 3.1*.

The gray features represent the pattern defined with chrome as the absorbing film, while the rest is transparent quartz. Optical lithography (image reversal technique) was used to define the e-beam markers and bonding pads. This method of image reversal produces negative tone images in positive photoresist. Most of the sample preparation took place in the 100 class cleanrooms of ISG2 and IEM at the Forschungszentrum Jülich. The standard procedure is shown schematically in *Fig. 3.2*.

First a 600 nm layer of AZ5206 photoresist is spun onto the sample and soft baked at 90°C for 2 min to remove the solvent and make the resist photosensitive. Then, the sample is exposed through the photomask shown in *Fig. 3.1* for 2.4 s. Although this is a positive photoresist comprised of a novolak resin and a photoactive compound, it is capable of image reversal resulting in a negative image of the mask pattern and a negative wall profile ideally suited for lift-off. The image reversal capability is obtained by a special crosslinking agent in the resist formulation which becomes active at temperatures above 110°C and only in exposed areas of the resist. The

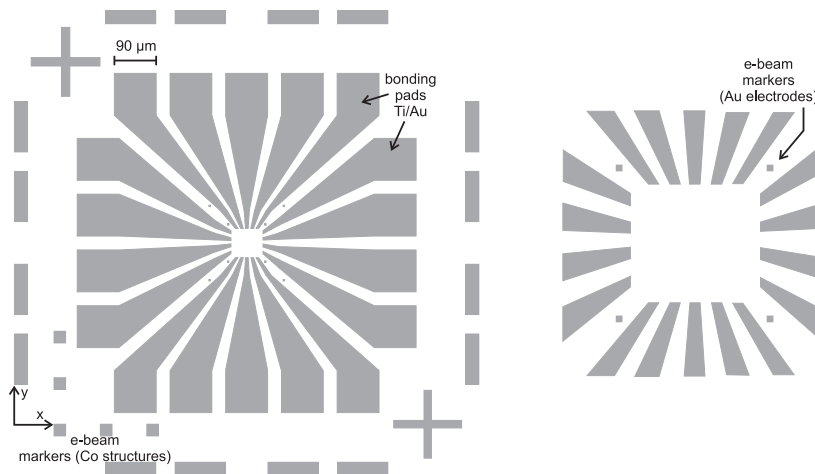


Figure 3.1: One cell of the optical mask (left) and a zoom in the center of the cell (right). There are 5×5 cells with a separation of $500 \mu\text{m}$ in between on a $10 \text{ mm} \times 10 \text{ mm}$ sample.

baking time was 2 min at 115⁰C. The crosslinking agent together with the exposed photoactive compound leads to an almost insoluble substance in the developer (AZ326 MIF:H₂O), which is no longer light sensitive, while the unexposed areas still behave like normal positive photoresist. After a flood exposure (no mask required) of 12 s these areas are dissolved in standard developer for positive photoresist and the crosslinked areas remain. This is done by dipping the sample for 25 s in a mixture of 100 ml AZ326 MIF and 12 ml H₂O. Before depositing metal, possible left-over photoresist in non-crosslinked areas, which can reduce the adhesion, is burned by exposing the sample to 200 sccm oxygen plasma for 2 min at 300 W. Next, 5 nm of Ti were deposited by e-beam evaporation to ensure good adhesion to the substrate followed by 100 nm of Au to define the e-beam markers and electrodes at a base pressure of 2×10^{-7} mbar. After metallization, the sample is transferred to an acetone bath, where the resist is dissolved. With this lift-off technique metal is only left where it was evaporated directly onto the substrate. In the end a cleaning step in NMP (N-Methyl-2-Pyrrolidone) at 80 °C for one hour is performed to ensure that no photoresist is left onto

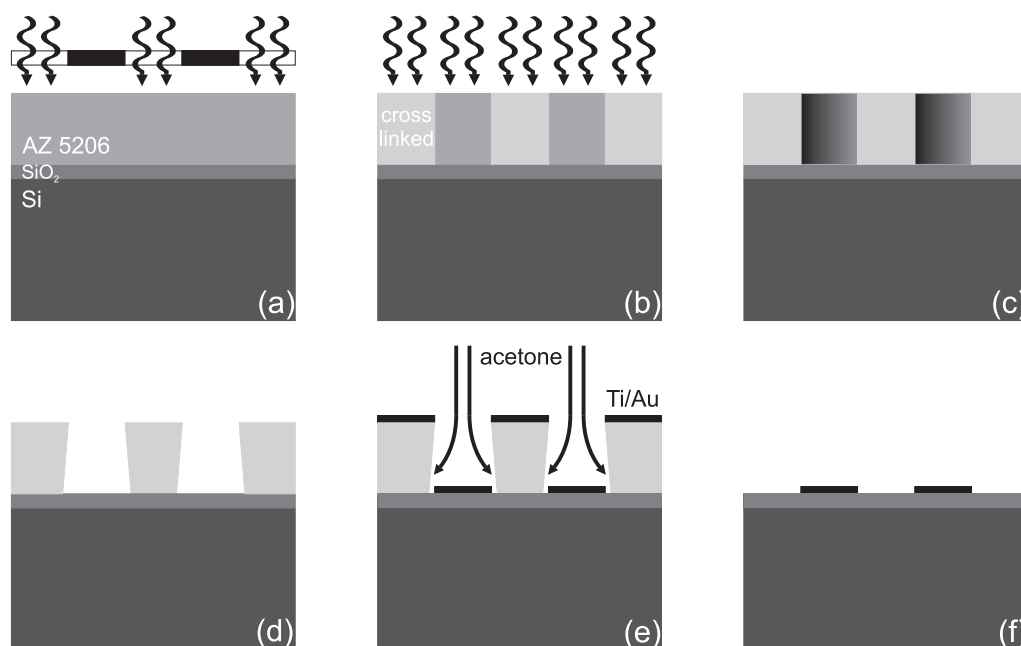


Figure 3.2: *Optical lithography - image reversal technique: (a) spin coating, soft bake and light exposure around the features where the metal will be deposited; (b) post exposure bake resulting in a crosslinking of the previous exposed areas and flood exposure; (c) flood exposure makes previously unexposed areas soluble to developer; (d) after development; (e) metal deposition and lift-off - the remaining resist is dissolved in acetone; (f) the final result - only the metal evaporated directly onto the substrate remains.*

the substrate. The final result is a 10 mm x 10 mm sample with 5 x 5 cells (like that on *Fig. 3.1*) with a separation of 500 μm between the cells.

3.1.2 Electron beam lithography

Derived from the early scanning electron microscopes, the electron beam lithography (EBL) technique consists of scanning a narrow beam of electrons across a surface covered with a resist film sensitive to those electrons, thus creating a latent image of the desired pattern in the resist film. EBL is a maskless technique offering the ability to change lithography patterns from one run to the next without incurring the cost of generating a new photomask. Besides flexibility, EBL is capable of very high resolution, but is also slower than optical lithography.

Electron beam lithography tools are capable of forming extremely fine probes, however, there are non-negligible effects due to electrons hitting the workpiece [78]. As the electrons penetrate the resist, they experience small angle (forward) scattering, which tend to broaden the initial beam diameter. As the electrons penetrate into the substrate, they occasionally undergo large angle scattering (backscattering). The backscattered electrons cause the proximity effect, where the dose that a pattern feature receives is affected by electrons scattering from other features nearby. During the propagation process the electrons are continuously slowing down, producing a cascade of low energy electrons called secondary electrons. These are responsible for the bulk of the actual resist exposure process. Since their range in resist is only of a few nanometers, they contribute little to the proximity effect. Instead, the net result can be considered to be an effective widening of the beam diameter. In the simplest positive resists, electron irradiation breaks polymer backbone bonds, leaving fragments of lower molecular weight. A solvent developer selectively washes away the lower molecular weight fragments, thus forming a positive tone pattern in the resist film.

Two EBL steps were used: first, magnetic structures were written and second connected by Au pads with Ti/Au electrodes previously defined by optical lithography. The aim was to obtain a very small magnetic nanocontact between two wider magnetic electrodes. For the first EBL step we used a dedicated Leica EBL system whose high e-beam energy and stable current ensure high reproducibility. It also provides fully automated sample movement and pattern alignment. We have chosen a two-layer PMMA (polymethylmethacrylate) resist system, with a high molecular weight PMMA (950 K 3%) on top of a low molecular weight PMMA (200 K 4%). The bottom PMMA is more sensitive than the top layer resulting in an undercut resist profile which aids in the lift-off process providing a clean separation of the metal from the resist walls. The standard procedure is shown in *Fig. 3.3*.

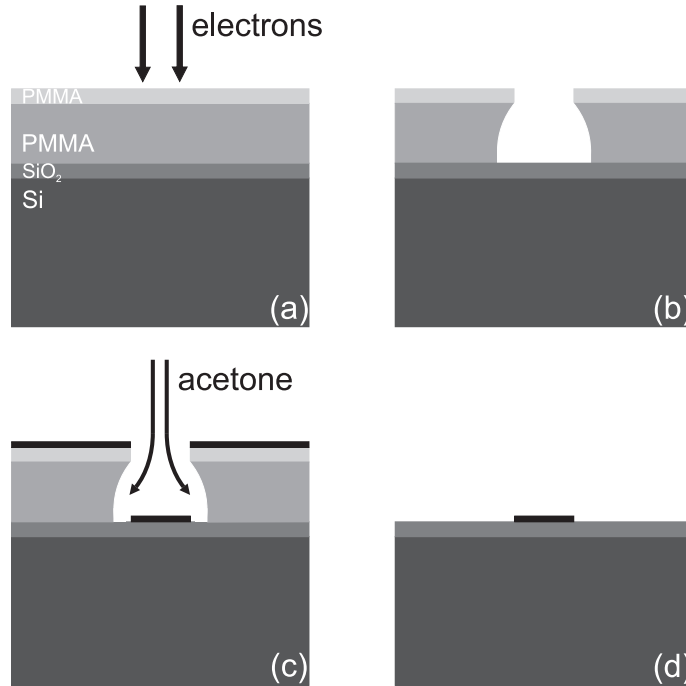


Figure 3.3: *Electron beam lithography: (a) spin coating, bake of two PMMA resist layers and e-beam writing of the desired pattern; (b) undercut profile obtained after development; (c) metal deposition and lift-off; (d) the final result.*

Additionally, by using a high energy of 70 keV and a thin PMMA top layer, the electrons pass the first resist layer without being significantly (forward) scattered losing their energy in the bottom PMMA layer. Thus, small features close to the size of the e-beam diameter (20 nm) could be realized. To go below that limit, we designed the electrodes with a gap in between expecting help from the proximity effect to expose the gap. *Fig. 3.4* schematically depicts the mechanism used to form small nanocontacts.

When the resist is exposed by the electron beam at the tip of each electrode, then the interelectrode region is also partially exposed because the beam has a Gaussian intensity profile (indicated by the dotted lines in *Fig. 3.4*). Since the designed gaps of 5, 10, and 15 nm are close to the actual beam size, both beams overlap in the gap region. Therefore, an overall beam dose whose profile is described by a solid line in *Fig. 3.4* interacts with the resist in this region. Consequently, after developing, the area dosage remains higher than threshold exposure dosage and forms a nanocontact structure. We could go down to 11 nm nanocontact width, which is below the e-beam diameter, for a designed gap of 15 nm and a dose of $220 \mu\text{As}/\text{cm}^2$ as shown in *Fig. 3.5 c* - bottom image.

Taking advantage of EBL flexibility the magnetic structures were varied as follows: Along the y-direction, magnetic structures with different ge-

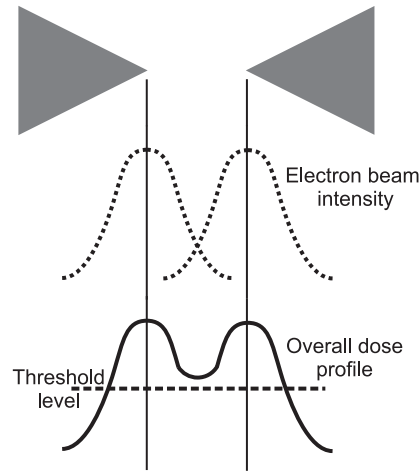


Figure 3.4: Schematic representation of the proximity effect of e-beam lithography. The designed gap between the electrodes (up) is exposed indirectly by the two beams overlap (middle) with a dose above the threshold level (bottom).

ometries and sizes were written resulting in a variation of the nanocontact geometry. These geometries are shown in *Fig. 3.5 b*. Along the x-direction, the e-beam dose was varied between $200 \mu\text{mAs}/\text{cm}^2$ to $280 \mu\text{mAs}/\text{cm}^2$ in steps of 20, affecting the nanocontact size but without changing the electrodes. Inside each cell there were four identical structures marked with dashed circles in *Fig. 3.5 a*. They were designed with no gap and 5, 10, and 15 nm gap in between the electrodes starting from up to down in order to obtain an additional variation of the nanocontact region. In this way nanocontacts with widths ranging from 11 nm to 170 nm and different geometries were realized in the same batch and on the same sample, offering the possibility of a thorough study of the spin-dependent transport.

In the second EBL step, the 20 nm thick cobalt structures are linked with the bonding pads by 100 nm thick Au electrodes. A non-magnetic material was chosen to eliminate any influences on the magnetic reversal of our structures. A completely cell is presented in *Fig. 3.5 a*.

Because this step is not so critical regarding size reproducibility we used a scanning electron microscope (SEM) for the writing process. The system consists of a Leo-1550 emission electron microscope equipped with a Raith lithography system and Elphy-Plus software. The maximum energy this SEM can provide is 20 keV which is too low to avoid forward scattering in the first PMMA layer and thus, a well defined cut-off profile is not realized. Giving that size reproducibility is not critical, the same two-layer PMMA resist system like in the first EBL step was used. Unlike the Leica system, the Raith's SEM conversion kit we used only had manual alignment. Thus, patterns were limited to single writing fields. Corrections for rotation, shift, and orthogonality were applied to single fields (with single patterns); these

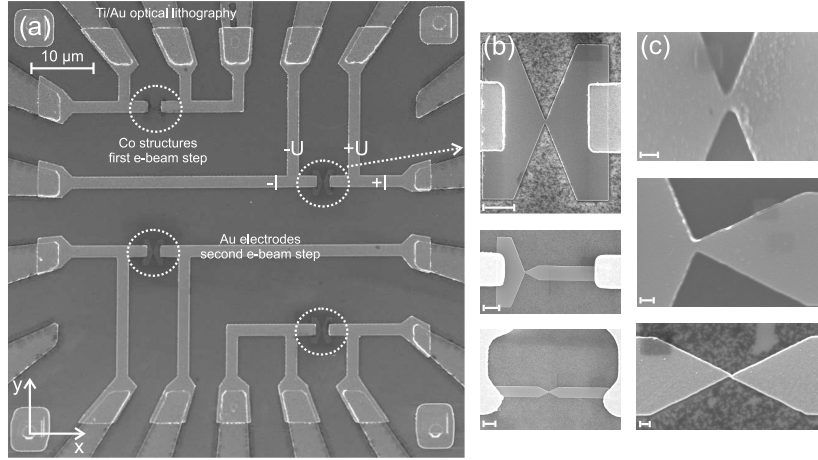


Figure 3.5: SEM pictures of (a) ready to measure cell; (b) examples of cobalt structures - scale bar 1 μm ; (c) zoom of the nanocontact region - scale bar 100 nm.

corrections were not applied globally to correct the sample rotation and stage nonorthogonality. Before exposure, the desired electrode pattern could be well adjusted by a two step alignment procedure: first taking a low resolution SEM image of each cell center also containing the four e-beam markers seen as squares in each corner of *Fig. 3.5 a* (rough alignment), followed by a high resolution scanning of each marker (fine alignment). The alignment consists of “dragging” the markers from the SEM images over the designed ones. The writing field (where exposure takes place) is 120 μm which covers the center of the cell together with the e-beam markers, the corresponding SEM magnification being of 850. The most important parameters for exposure are related by the formula: $t = ds^2/I$, where d is the dose (As/cm^2), I is the beam current (A), s is the step size (μm or pixel) and t is the dwelling time. The “step size” defines the distance between exposure spots either in μm or pixel, the entire writing field size is divided into $2^{16} = 65536$ pixels (16 bit DAC range) with the relation between the writing field size and step size (in μm and in pixel) defined as: $\text{step size } (\mu\text{m}) / \text{writing field size} = \text{step size (pixel)} / 65536$. The “dwelling time” parameter defines the waiting period for the beam in each writing spot during exposure. Considering a dose of 200 $\mu\text{mAs}/\text{cm}^2$, a beam current of 80 pA, a step size of 4 nm = 2 pixel, the calculated “dwelling time” is 400 μs .

The fabrication procedure is similar to the one depicted in *Fig. 3.3*. The only difference consists in an Ar plasma etching step in order to remove the native CoO before depositing Au *in-situ* by sputtering at a pressure of 10^{-7} mbar. This step ensures an ohmic contact Au/Co and thus a low resistance which is mainly given by the nanocontact cross-section.

3.2 Setup for transport measurements

The final device, bound on a chip carrier, is mounted in an exchange gas continuous flow cryostat with the possibility of applying a magnetic field up to 1.2 T. The cryostat comprises a heat exchanger, sample space, radiation shield and vacuum case. Liquid He is drawn from a separate helium storage dewar and circulated through the heat exchanger in the cryostat. The circulating cryogenic liquid does not come into contact with the sample, a separate He exchange gas being present in the sample region. This gas is in good thermal contact with the heat exchanger, thus cooling the sample by conduction through the exchange gas. The lowest working temperature was 4.2 K. The experimental setup is depicted in *Fig. 3.6*.

The external magnetic field can be applied in the sample plane at an arbitrary angle with respect to the nanocontact axis. To vary the angle a stepper motor is coupled to the sample holder. Different types of measurements including: magnetoresistance (R vs. B), voltage - current (V - I), angular magnetoresistance (R vs. θ) can be performed. All are run by a computer via LabView programs.

Transport measurements were performed in a four-point geometry, mainly at room temperature, but also at 4.2 K. The connections to a magnetic structure are presented in *Fig. 3.5 a*. For the d.c. case (see *Fig. 3.7 a*), a constant direct current of maximum 1 mA was applied with a Keithley 224 current source and a voltage drop $\Delta U = U_+ - U_-$ of the order of tens of mV was measured with a Hewlett Packard 34401 A multimeter. Thus, the

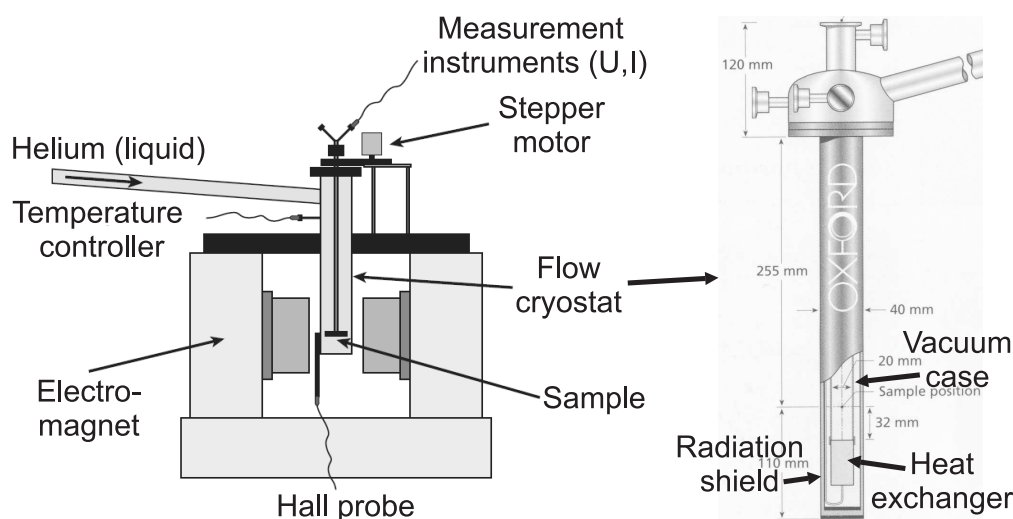


Figure 3.6: Schematic drawing of the experimental set-up and cryostat. An external magnetic field is applied in the sample plane under a variable angle set by a stepper motor.

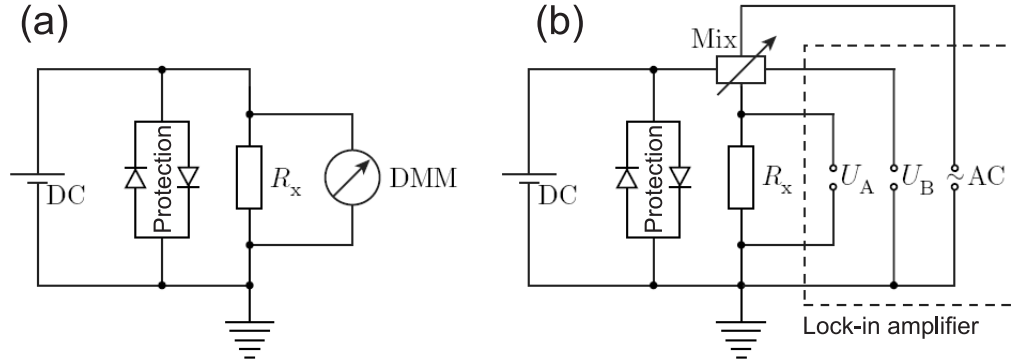


Figure 3.7: *Electronic schemes to determine the unknown resistance R_x . (a) A constant current I (DC) produces a voltage drop ΔU on R_x which is measured by a digital multimeter (DMM). To protect the sample against excess current two diodes are mounted in parallel with the sample (one for each current flow direction). The absolute resistance $R = \Delta U/I$ is measured. (b) A sinusoidal voltage given by the internal oscillator of the lock-in amplifier is applied to the sample producing a sinusoidal current. This creates an alternative voltage drop U_A which is in phase with the applied voltage. To increase the sensitivity a constant modulated voltage U_B is subtracted from U_A using the A-B mode of the lock-in. A resistance in arbitrary units is given due to compensation.*

absolute change in resistance $\Delta R = \Delta U/I$ could be calculated. The current density in the nanocontact was of the order of 10^7 A/cm² range. While such a current still reduces the life of the nanocontact, it is low enough not to generate heating effects and domain wall depinning by the current. For smaller d.c. currents the voltage drop falls within the noise limit (± 10 μ V). To gain sensitivity, a sinusoidal voltage of a few mV with a frequency of 1.2 kHz was applied to the sample by a lock-in amplifier model 5209 from EG&G Princeton Applied Research (see *Fig. 3.7 b*). The resulting sample modulated signal was input in the channel A of the lock-in amplifier, while the compensation signal was input in channel B. Because the two signals are in-phase, they can be subtracted using the A-B mode of the lock-in amplifier. Two to three orders of magnitude (typically mV to μ V) can be gained by compensation, while the physics of the measurements remains unchanged, because the signal at B is constant. Thus, the main advantage of this technique is to provide a high resolution using a small bias current of 0.1 mA. It also has a drawback: namely, due to compensation, the results are given in arbitrary units [a.u.], and a d.c. measurement is additionally needed for a quantitative analysis.

3.3 Magnetic Force Microscopy

Magnetic Force Microscopy is one of the most commonly used magnetic imaging techniques. There are many commercial as well as home-made MFM instruments with different operating modes and detection/feedback schemes. All of them are using the same principle, detection of a force gradient between the magnetic coated AFM tip and magnetic sample. To generate a magnetic image, MFM can be operated in a constant frequency shift mode [79], a tapping/lift mode [80] or a constant height mode. They are schematically presented in *Fig. 3.8*.

A commercial MFM system was used, MultiMode SPM from Digital Instruments, which operates in a tapping/lift mode that allows to separate between magnetic contrast and topography. The MFM tips from NanoSensors have a 40 nm thick cobalt alloy coating. As shown in *Fig. 3.8 b*, measurements are taken in two passes across each scan line; each pass consists of one trace and one retrace. In the first pass, topographical data is taken in tapping mode using the cantilever oscillation amplitude as feedback. In the lift mode the tip is raised to an user controlled scan height (h) which takes into account the previously measured topography, providing a constant separation between the tip and local surface topography. The interaction between the sample stray field and the magnetic tip is detected by monitoring the cantilever's frequency (or the phase) shift with respect to the resonant frequency. A quantitative analysis of the observed magnetic contrast is not straightforward, since MFM does not directly monitor the magnetization distribution, but rather the stray field. Furthermore, one needs to know the tip stray field and its distribution to estimate the mutual distortion between the MFM tip and the sample moment for a given tip-sample separation [81]. MFM images of a cobalt structure and nanocontact are shown in *Fig. 3.10 b* and *c*, respectively. It was taken at remanence following positive saturation (+200 mT) with a lift scan height of 30 nm.

For parallel sample/tip stray fields directions the tip will feel an at-

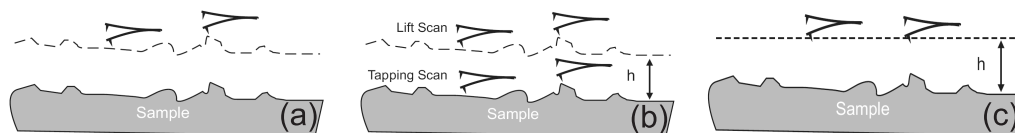


Figure 3.8: Schematic diagrams of the different operating modes: (a) constant frequency shift mode. The feedback loop maintains the resonance frequency at a constant value by adjusting the tip-sample separation; (b) tapping/lift mode, tapping scan is used to obtain the sample topography, while the lift scan follows the measured topography with a lift height h (dashed line). Clean separation of topography signal and magnetic signal can be obtained; (c) constant height mode. The tip lies in a plane above the surface.

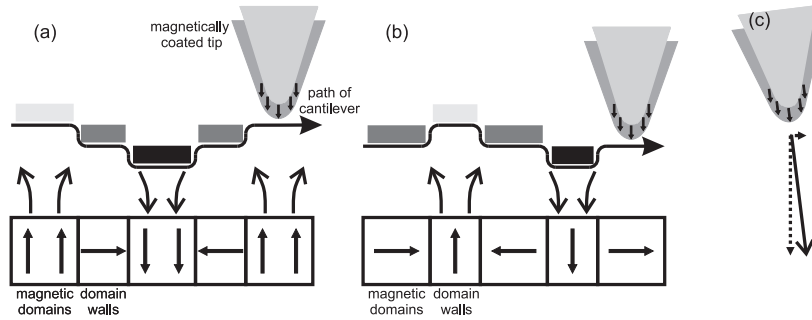


Figure 3.9: Schematic description of the MFM principle. The main source of sample stray fields are (a) magnetic domains for out-of-plane magnetized sample; (b) domain walls for in-plane magnetized sample. The attractive or repulsive interaction with the tip stray field determines a path for the cantilever. The associated magnetic contrast is shown above the path. (c) small canting of the tip presumably responsible for the in-plane sensitivity.

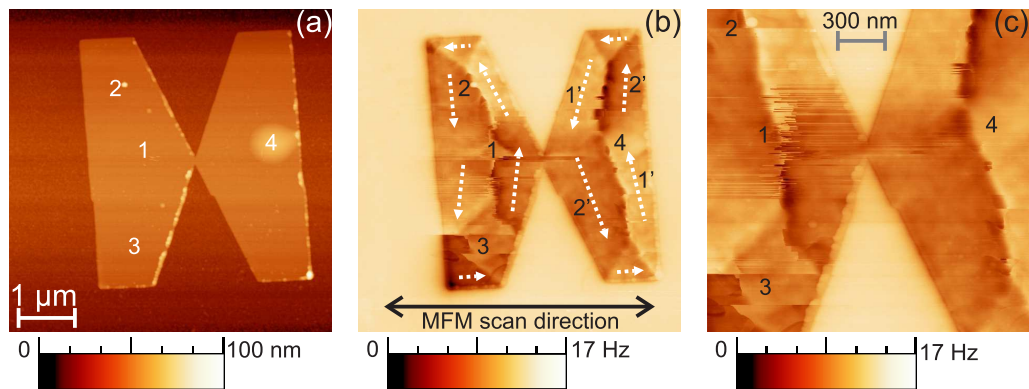


Figure 3.10: Examples of MFM images following positive saturation $B = 200$ mT: (a) topography, (b) magnetic signal, (c) image of the nanocontact region taken in the next scan. Both MFM images were taken with a lift scan height of 30 nm. Regions 1, 1' and 2, 2' demonstrate the in-plane sensitivity of the magnetic tip. Regions denoted with 1 and 3 show a reversible and respectively, an irreversible change of the sample magnetic configuration due to the MFM tip stray field. The topographic feature indexed with 2 influences the magnetic imaging, while the feature 4 has no significant influence. The white arrows represent the magnetic configuration given by the magnetic contrast.

tractive force (force gradient) and the cantilever resonance frequency will become smaller - dark contrast. For antiparallel case the opposite happens, the MFM tip will feel a repulsive force and its resonance frequency will increase - bright contrast [83]. The ideal case for a thin film is presented in *Fig. 3.9* for out-of-plane (a) and in-plane (b) magnetized sample.

Our sample is magnetized in-plane so what we should see are just the stray fields coming out from domain walls and vortices. Nevertheless, a

different magnetic contrast is observed for antiparallel in-plane magnetized regions of the sample (1, 1' and 2, 2' in *Fig. 3.10 b*). The in-plane sensitivity can be explained by a small canting of the tip relative to the surface normal as shown in *Fig. 3.9 c*. This produces a parallel component with the sample surface of the tip stray field, which interacts with in-plane magnetization giving a dark contrast for parallel alignment and a bright contrast for the antiparallel case. Taking into account the previous considerations, a magnetization distribution like the one outlined in *Fig. 3.10 b* is deduced in our sample.

During MFM imaging, especially in the tapping mode, the tip and sample are in contact to each other. This can potentially lead to an alteration of the magnetic configuration by the tip. To check this, the same structure was scanned along two perpendicular directions. The result is shown in *Fig. 3.11*, demonstrating that the magnetic tip does not influence the magnetic structure during the tapping mode.

However, the MFM tip stray field can cause locally, reversible and irreversible distortions which can be enhanced by topographic features. It can reversibly affect domain walls by moving them back and forth during the trace and retrace. This effect can be seen in region 1 of *Fig. 3.10 b*, while it disappears in the next scan - *Fig. 3.10 c*. It can also irreversibly change magnetic structure by locally moving domain walls to new energy minima, without returning to the original position even when the tip stray field is removed - region 3 of *Fig. 3.10 b* and *c*. The area denoted with 2 is an example of a distortion caused by a topographic feature, while, on the contrary, feature 4 has no significant influence on the magnetic contrast. This difference can be explained by the abrupt change in topography caused by feature 2 in comparison with a relatively smooth change seen for feature 4.

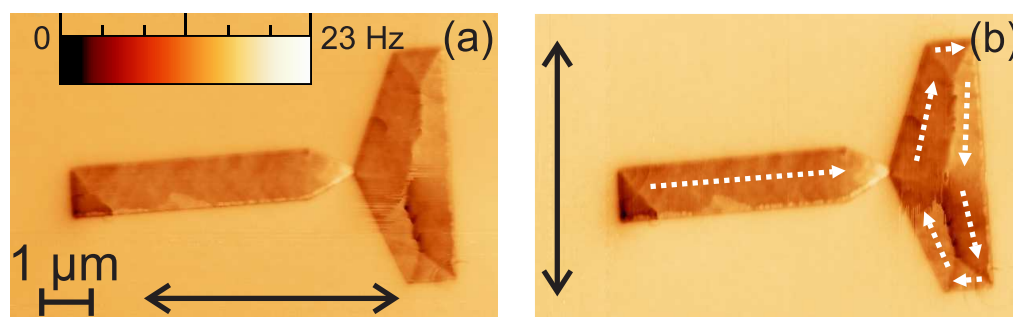


Figure 3.11: *Experimental proof that the magnetic tip does not write the structures during the tapping mode. (a) first MFM image; (c) second MFM image on the same structure. The scan directions are indicated on the MFM pictures. The white arrows represent the magnetic configuration given by the magnetic contrast.*

Chapter 4

Experimental results and discussions

It has been experimentally established that domain walls contribute to the magnetoresistance and numerous theoretical formulations have been proposed (see Sec. 2.4 and 2.5). In most cases, the domain wall (DW) scattering contribution is embedded in larger contributions from the anisotropic magnetoresistance (AMR) and the Lorentz magnetoresistance (LMR). In the following, I will describe the MR and MFM measurements on 20 nm thick cobalt nanostructures of different geometries and sizes that contain localized constrictions. The purpose of the constriction is twofold: first, to magnetically decouple the electrodes, and second, to act as a pinning center for domain walls. The magnetic field was swept from positive to negative saturation (backward sweep +/-) and back (forward sweep -/+) in order to see the hysteretic behavior. The magnetic field was applied usually in-plane, parallel to the current (longitudinal configuration) as well as perpendicular to the current (transversal configuration). This study starts with an extended cobalt thin film and continues with different patterned structures, which provide well-defined transport measurement geometries. To explain the measured MR curves, the understanding of the magnetization reversal processes from the micromagnetic point of view is needed. For this propose, micromagnetic simulations were performed using the public code OOMMF described in Sec. 2.6. Since the temperature is not included and the simulated area ($1 \mu\text{m} \times 522 \text{ nm}$) represents only a small part of the real sample, the simulations give a qualitative description of the reversal. This generally results in an overestimation of the switching fields. Throughout this chapter the micromagnetic calculations are displayed using arrows and colors. The arrows represent the top view (z axis) and are mostly black because the magnetization lies in the sample's plane. The color code gives the in-plane (x - y) magnetization configuration: red (+ x), blue (- x), white($\pm y$).

4.1 Cobalt thin films

The 20 nm thick cobalt films were deposited by electron beam evaporation on Si/SiO₂ substrate at a rate of 0.1 Å/s in a vacuum system with a pressure of 2×10^{-6} mbar. The structural properties of the Co films have been investigated using AFM and XRD. The films are polycrystalline consisting of small grains with an average size of 3 nm and a surface roughness of 0.28 nm (see *Fig. 4.1*). The crystal structure is found to be mainly hcp Co from XRD measurements. The residual resistance ratio $\Gamma = R(300 \text{ K})/R(4.2 \text{ K})$ is low ($\Gamma = 1.4$), indicating that the films are highly disordered. According to the Kohler plot [82] the classical Lorentz magnetoresistance becomes negligible for highly disordered metals. The LMR contribution, which is proportional to $(\mu B)^2$ was estimated to $\simeq 5 \times 10^{-6} \%$ [83] for typical magnetic fields of $B \leq 300$ mT, and can be thus safely neglected. Thus, the observed magnetoresistance effects are mainly due to AMR and DWMR.

To characterize the magnetic properties of the films, magnetoresistance, MOKE, and SQUID measurements were performed. In *Fig. 4.2 a* and *b* the MOKE and MR measurements for a 20 nm thick cobalt film are given. The dashed lines emphasize the correspondence of the magnetization reversal to the MR curves, demonstrating that the MR measurements can be used as a indirect tool to determine the magnetization reversal process. The similarity of the MOKE curves, taken with the magnetic field applied in-plane of the film, parallel and diagonal to the sample's edge, indicates that no magneto-crystalline anisotropy is involved. This means that the magnetic easy axis of the Co grains in the polycrystalline film is randomly distributed. In the following the longitudinal and transversal MR curves are discussed (*Fig. 4.2 b*). In the longitudinal configuration, coming from positive saturation, a decrease in resistance at remanence as compared to the saturation is observed. Below $B = 0$ mT, the resistance continues to decrease until

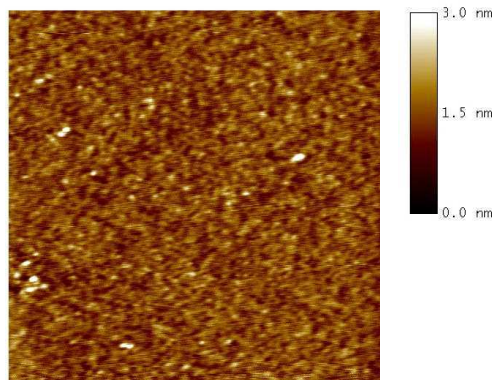


Figure 4.1: AFM image ($2 \times 2 \mu\text{m}^2$) of a 20 nm thick Co film on SiO₂/Si substrate.

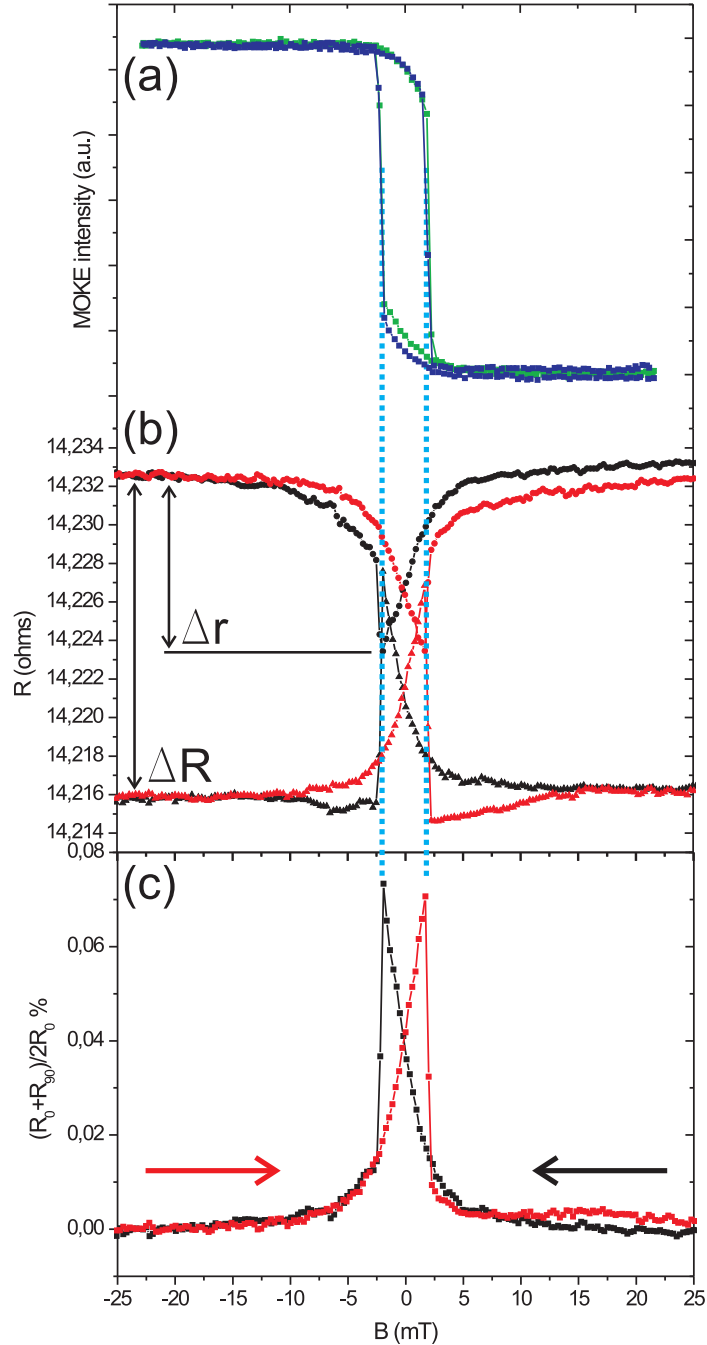


Figure 4.2: (a) and (b) Comparison of Magnetization vs. B and Resistance vs. B - hysteresis curves for the same Co film. B represent the external applied magnetic field. MOKE measurements were performed with the in-plane magnetic field applied diagonally (green) and parallel (blue) to sample's edge. The longitudinal (circles) and transverse (triangles) MR curves show a hysteretic behavior with two peaks at the coercive fields $B = \pm 2$ mT. The corresponding values of $MR = [R(B) - R_p]/R_p$ are 0.08% and -0.06%, respectively. The saturation magnetic field was ± 70 mT. (c) Domain wall scattering induced resistance obtained by adding transverse and longitudinal magnetoresistance curves. The black/red arrow represents the backward/forward sweep direction.

the switching field is reached, followed by a continuous increase back to the saturation value. This behavior is explained as originating from the formation of domains with transversal magnetization (M_{\perp}). The fraction of M_{\perp} is given by $(\Delta r/\Delta R) \times 100$, assuming that ΔR corresponds to an in plane perpendicular magnetization fraction of $M_{\perp} = 100\%$. It increases, reaches a maximum of 53% at the coercive field, and decreases towards the negative saturation, showing an opposite behavior as compared to MR. In the transverse configuration, following a similar reasoning, the increased fraction of longitudinal magnetization accounts for the increase in resistance. The magnetization reversal process ends, when the magnetization aligns with the applied negative magnetic field. These correlations suggest that the MR curves are dominated by the anisotropic magnetoresistance effect discussed in Sec. 2.2.

The symmetry properties of AMR were used to subtract it from the measured signal as proposed by Viret *et al.* [43]. Measurements were performed, where the current flow was along and normal to the field direction. Due to the small grain size of our films and the extended shape no magneto-crystalline or shape anisotropy is involved, which can affect the reversal mechanism by imposing preferred directions. It can be seen from Eq. 2.2 that $\text{AMR} \sim \cos^2 \theta$, where θ is the angle between magnetization \vec{M} and current density \vec{J} . Thus, the diagonal and parallel measurements will generate AMR signals that are $\propto \cos^2 \theta$ and $\propto \sin^2 \theta$ respectively. If there is no other effect than AMR in the sample, these two terms should add to a constant. Any deviations should reveal a magnetoresistance of other origin. The data obtained for the Co film is displayed in *Fig. 4.2 c*. The deviation from AMR, visible in the $(R_{0^\circ} + R_{90^\circ}/2R_{0^\circ})$ vs. B plot, is due to domain wall scattering.

The sign of this DWMR contribution as well as its magnitude (7×10^{-4}) are found to be in agreement with those observed Viret *et al.* (2×10^{-4}), thus determining the applicability of their model to this case (see Sec. 2.4.1). The positive peaks, which appear at the coercive field are attributed to an extra resistance based on the Larmor precession of the conduction electrons, which experience difficulty in following adiabatically the changing orientation of the local exchange field while crossing domain walls. We also note that this value is of the same order of magnitude as the one found theoretically by Cabrera and Falicov in the case of hundreds of nm wide domain wall (see Sec. 2.4.1). Taking into account the similar results of other works, we conclude that the domain walls in our cobalt films give a positive contribution to the resistance.

In *Fig. 4.3* SQUID measurements on a cobalt film are shown. Because after deposition the cobalt film is exposed to air, a native antiferromagnetic CoO layer should be formed on the surface. To check this the Co/CoO system was cooled below the Néel temperature of the antiferromagnet ($T_N \approx$

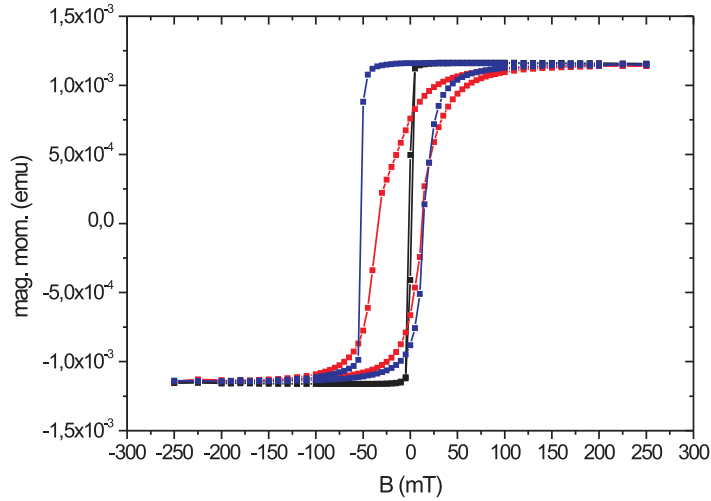


Figure 4.3: *SQUID* investigations of a 20 nm thick cobalt film at room temperature (black), and at 30 K with zero field cooling (red) and field cooling of 250 mT (blue), demonstrating the presence of a native CoO film. The magnetic field was applied in the sample's plane.

290K), where due to the exchange bias effect [84] the Co layer is biased. This should result in a negative shift of the hysteresis loop of the ferromagnet in comparison with the room temperature loop (shown in black), which was indeed observed. The strength of the exchange bias field depends on the cooling procedure. When cooling down in the presence of a magnetic field (shown in blue) the biased Co behaves, as if it possesses a unidirectional anisotropy axis along the cooling field direction showing a larger shift and an abrupt switching. In the zero field cooling case (shown in red) the exchange bias varies locally giving rise to a smaller shift and a smooth switching.

4.2 Long rectangular electrodes: Structure A

The first type of magnetic structure is shown in *Fig. 4.4 a*. It consists of two identical cobalt electrodes with a constriction of variable width (18, 21, 36 and 77 nm) between them. An MFM scan taken at remanence following positive saturation in a magnetic field of 200 mT applied along the long axis of the electrodes reveals domain flux closure patterns within the sample, mostly visible at the ends of the electrodes. From the magnetic contrast one can infer a dominant monodomain-like remanence state due to the shape anisotropy. Representative longitudinal and transversal magnetoresistance

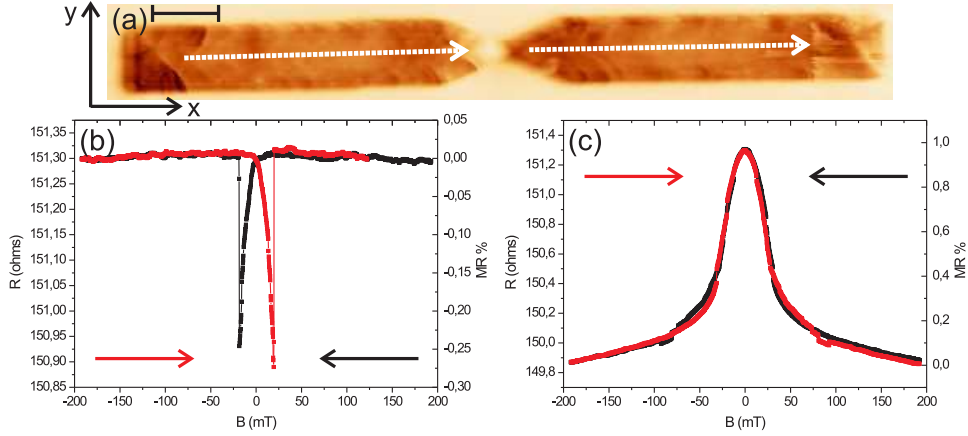


Figure 4.4: (a) MFM image at remanence after saturating the magnetization along the $+x$ direction. The scale bar is $1 \mu\text{m}$. Longitudinal (b) and transversal (c) magnetoresistance curves of a 36 nm wide nanocontact are shown. The backward ($+ 200\text{mT}/- 200\text{mT}$) and forward ($- 200\text{mT}/+ 200\text{mT}$) sweep directions are shown in black and red, respectively and with arrows.

curves of such a structure with a 36 nm wide constriction are shown in *Fig. 4.4 b* and *c*. The MR exhibits nonlinear hysteretic behavior showing irreversible and reversible transitions marked by abrupt and gradual changes in the resistance, respectively. In the longitudinal configuration, starting from positive saturation $B = + 200 \text{ mT}$, the resistance remains almost constant up to $B = 0 \text{ mT}$, since the magnetization in the nanocontact region remains mostly unchanged, which is consistent with the MFM result.

After applying the magnetic field in the opposite direction, transversal magnetization components develop in the electrodes as the magnetization reverses leading to a continuous resistance decrease with increasing magnetic field. On reaching the coercive field B_c where $M_{\perp} = 30\%$, the resistance sharply jumps to its saturation value. This fast switching reversal process can be explained by the dissolution of two domain walls at the nanocontact as will be discussed in more detail later.

In the transversal configuration the magnetic field is applied perpendicular to the current and the easy axis defined by the shape anisotropy. Decreasing the magnetic field from positive saturation ($B = + 200 \text{ mT}$), longitudinal magnetization components develop in the electrodes. The resistance increases and reaches the same remanent resistance value as in the longitudinal configuration corroborating that the contribution comes from shape anisotropy. Passing $B = 0 \text{ mT}$ towards negative saturation ($B = - 200 \text{ mT}$), transversal magnetization components develop in the electrodes leading to a decrease in resistance back to its saturation value. The magnetization reversal process can be described by predominantly coherent rotation

of the magnetization between the magnetic easy axis and hard axis. The shape of the MR and the relative resistance drop of up to 1% indicate that the changes in resistance, in both configurations, are due to the AMR effect.

In the following the results of the micromagnetic simulations on the 36 nm wide nanocontact are presented and discussed. They are used to check the conclusions drawn from the experiments. Complete simulations on this structure, in both configurations, are shown in *Fig. 4.5* (longitudinal case) and *Fig. 4.6* (transversal case). The evolution of the magnetization as a function of the applied field is qualitatively similar also for the 18 and 77 nm wide nanoconstrictions (the 21 nm wide structure was only used for MFM imaging). When the longitudinal magnetic field decreases from positive saturation (image *a2*) towards zero (*a3*), the magnetization at the electrode's ends rotates in order to lower the magnetostatic energy, while the rest remains mostly homogeneously magnetized along the $+x$ direction. Applying a negative field, the end domains grow by magnetization rotation and domain wall movement giving rise to reversed domains which approach the nanocontact region from both sides (*a4* to *a8*). The reversal occurs when the domains on each side of the nanocontact merge and dissolve (*a9* to *a15*), which corresponds to the sharp resistance jump observed in *Fig. 4.4 b*. In *Fig. 4.5 b* the calculated evolution of the magnetization components is shown along with the steps taken for the magnetic field. The increase in M_{\perp} (M_y - green) before switching accompanied by the decrease in M_{\parallel} (M_x - red) is qualitatively consistent with the experimental longitudinal MR for which the transversal magnetization components count. This leads to the continuous resistance decrease with increasing magnetic field observed before switching. It is also consistent with the AMR interpretation, because the resistance shows a minimum when the magnetization is perpendicular to the current flow direction.

The results of the micromagnetic simulations for the transversal field orientation are presented in *Fig. 4.6*. Returning from positive saturation (image *a1*) towards zero (*a2*) the magnetization aligns parallel to the nanocontact's axis and rotates in the electrodes to minimize the magnetostatic energy and follow the shape anisotropy. The relaxation is progressively resulting in a continuous increase in the longitudinal magnetization components (M_x - red), which accounts for the measured increase in resistance. Applying a negative magnetic field, reversed domains develop in the electrodes by magnetization rotation and domain wall movement. They extend into the electrodes approaching the nanocontact (*a3* to *a8*), which is the last reversed region by magnetization rotation (*a9* to *a12*). Thus, during the sweep to negative saturation the amount of transversal magnetization (M_y - green) increases which accounts for the measured decrease in resistance. The simulations confirm qualitatively that the changes in resistance are due to the AMR effect.

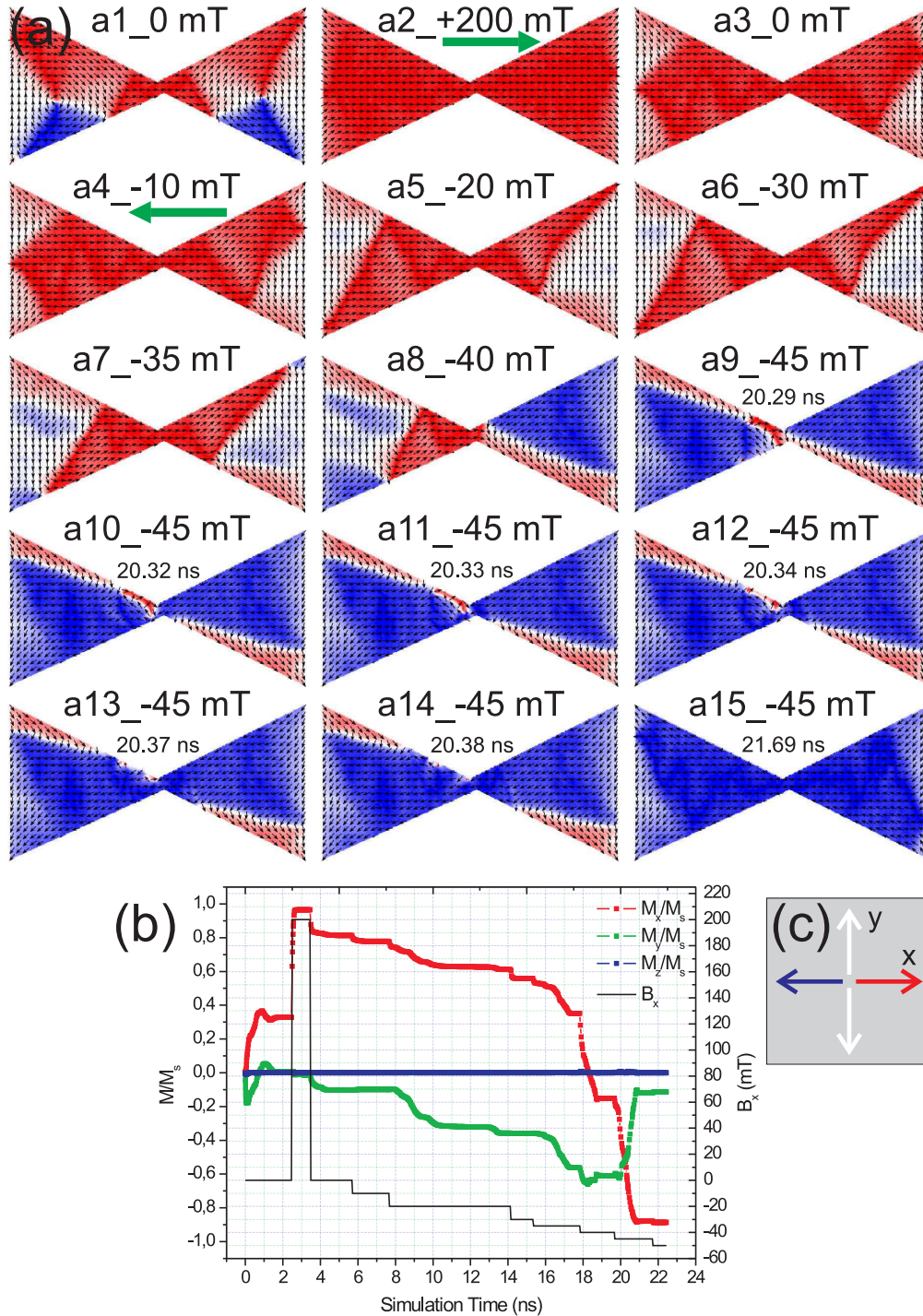


Figure 4.5: (a) The simulated evolution of the magnetization with the magnetic field applied along the long axis of the electrodes for the 36 nm wide junction is shown. The reference above the images represents their index and the applied magnetic field in mT. At the same magnetic field the difference is given by the simulation time in ns, which is displayed below the reference. The green arrows on (a2) and (a4) emphasize the direction of the magnetic field. (b) The corresponding evolution of the magnetization components integrated over the structure. (c) The color code for (a).

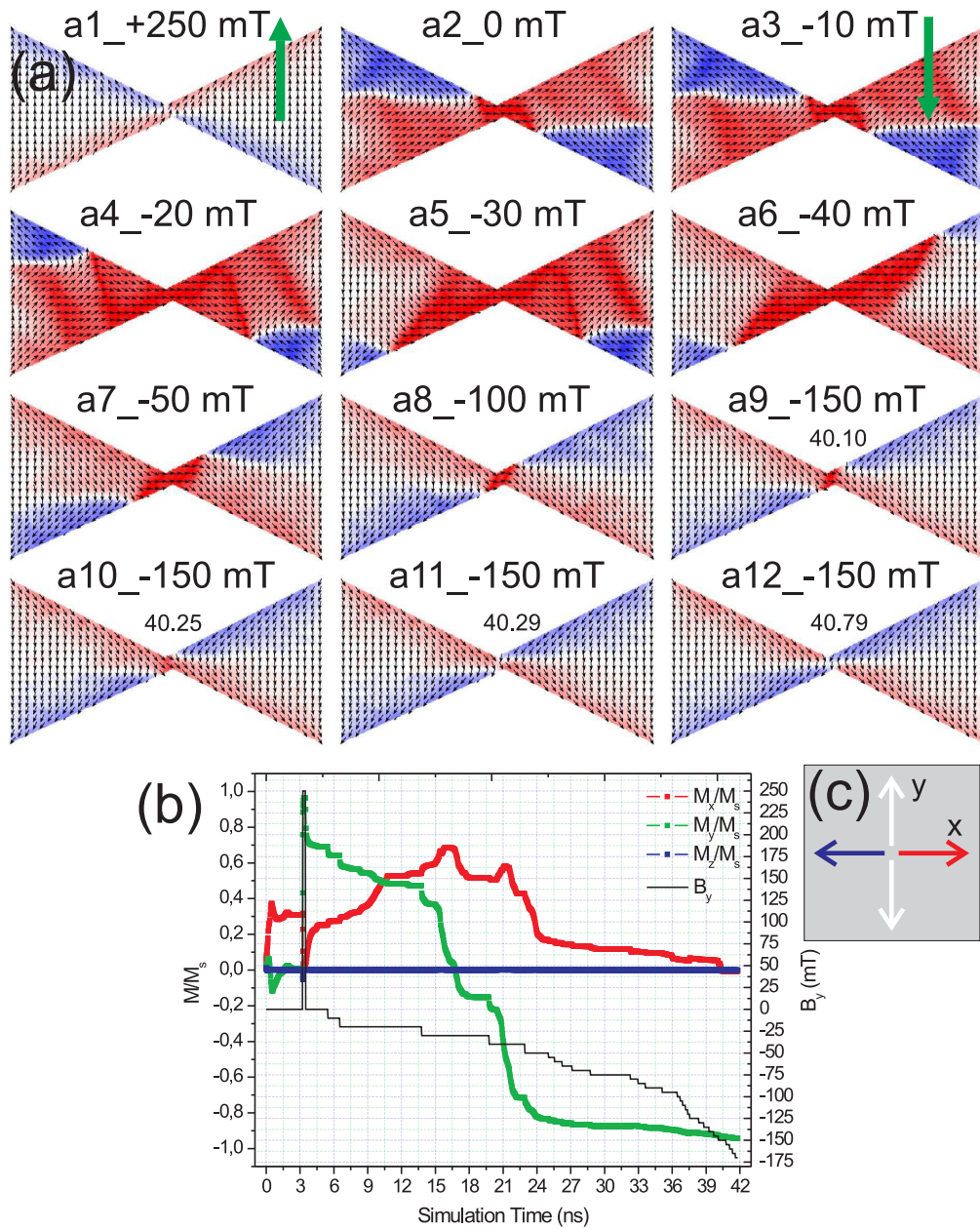


Figure 4.6: (a) The simulated evolution of the magnetization with the magnetic field applied perpendicular the long axis of the electrodes for the 36 nm wide junction. The reference above the images represents their index and the applied magnetic field in mT. At the same magnetic field the difference is given by the simulation time in ns, which is displayed below the reference. The green arrows on (a1) and (a3) emphasize the direction of the magnetic field. (b) The corresponding evolution of the magnetization components integrated over the structure. (c) The color code for (a).

Additional insight into the low resistance state can be gained by minor MR loops. In *Fig. 4.7* longitudinal MR traces for an 18 nm wide nanocontact are given. The left graph (a) is a complete MR cycle, which shows positive transitions at the coercive fields B_{c1} and B_{c2} . In the middle graph (b) the magnetic field is swept from positive saturation (black arrow) and stopped just before the sharp jump in resistance. Then, the field is swept back (red arrow), the MR curve indicating a reversible domain wall propagation and domain rotation. In the right graph (c) the sweep was stopped just after the jump. When sweeping back the high resistance state persisted up to $B = 0$ mT, and a positive transition is observed at a positive field B_{c2} . This is characteristic of an irreversible process due to the dissolution of domain walls, and strongly suggestive that B_c is the field, at which the two domain walls dissolve in the junction accompanying the reversal process as confirmed by the micromagnetic simulations presented above. Some snapshots illustrating this process are presented in *Fig. 4.9 a, b and c*. The presence of domain walls in the nanocontact region suggests that besides AMR, DWMR contributes to the measured signal.

The longitudinal MR behavior for three nanocontacts with different widths is shown in *Fig. 4.8*. The MR curves suggest that the underlying magnetization reversal processes are similar. This is confirmed by micromagnetic simulations carried out on the area around the nanocontact preserving its real dimensions and shape shown in *Fig. 4.9*. An asymmetric nanocontact is obtained after a voltage - current characteristic with a maximum current of 0.5 mA is measured on the 77 nm wide nanoconstriction, resulting in an asymmetric MR as compared with the previous MR measurements. As can be seen in *Fig. 4.8 c*, the structure exhibits a two-step switching process when returning from negative saturation. The first jump can be associated with the pinning of two domain walls at the constriction

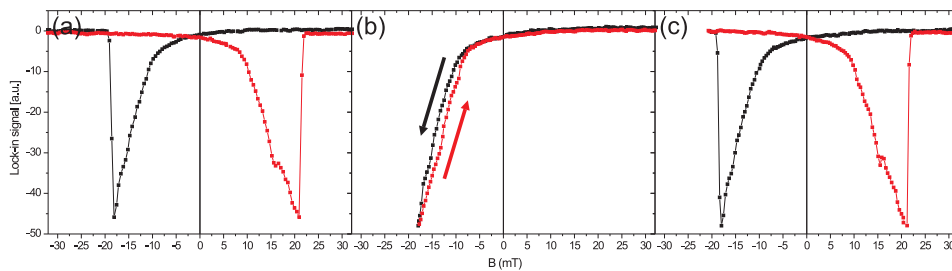


Figure 4.7: MR of a 18 nm wide nanocontact: (a) a complete MR curve; two minor loops showing a reversible (b) and an irreversible (c) change in MR. A typical hysteretic signature is recorded for the latter. The maximum applied field is ± 60 mT.

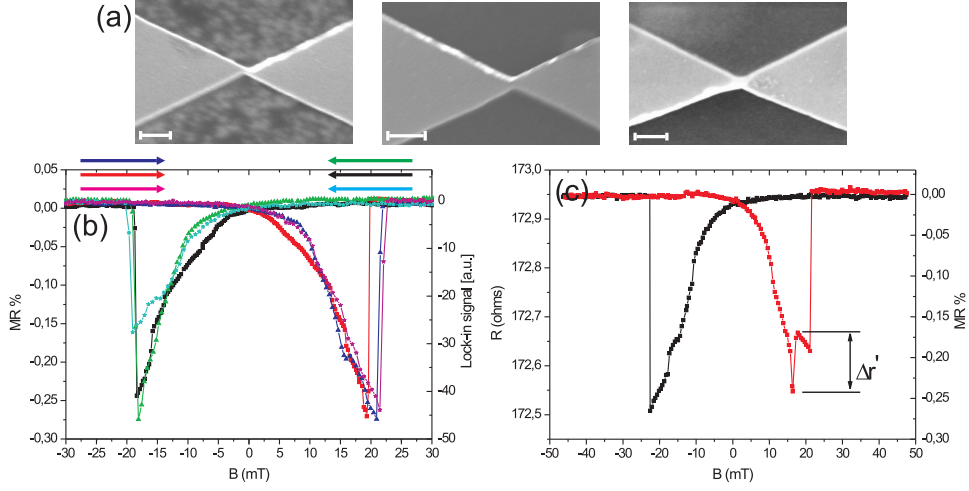


Figure 4.8: (a) SEM pictures of three nanocontacts with widths of 18, 36 and 77 nm (from left to right). The scale bars are 200 nm. (b) Comparison of longitudinal MR measurements performed on these nanostructures: 18 nm (triangles), 36 nm (squares), 77 nm (stars) (before applying a current of 0.5 mA). The arrows are associated with the symbols and show the sweep directions. (c) The MR response of the 77 nm width junction after applying a current of 0.5 mA. The first positive jump in resistance $\Delta r'$ is attributed to domain wall pinning.

as shown in *Fig. 4.9 g*. Similar MR was observed experimentally in [30] and discussed in Sec. 2.3.1. The continuously decreasing resistance after the first jump reflects the increasing amount of magnetization components in the nanocontact, which are oriented perpendicular to the current. The second step represents the dissolution of the two domain walls corresponding to the completion of the switching process. The absence of the second step in the opposite sweep direction can be explained by considering that an asymmetric nanocontact behaves like a domain wall diode [85]. Thus, each side of the nanocontact has a different pinning potential, which a domain wall needs to overcome. We suggest that a domain wall coming from right to left (backward sweep, shown in black) faces a weaker or no pinning, as compared to a DW coming from right to left (forward sweep, shown in red).

Combining simulation with experiment, the sign and magnitude of the DWMR effect are determined. From the simulation one can estimate the amount of $M_{\perp, sim}$ before the switching (*Fig. 4.5 a9*) to 51%, which gives $\Delta r_{sim} = (\Delta R_{exp} \times M_{\perp, sim})/100 = 0.66 \Omega$. ΔR and Δr are referred in *Fig. 4.2 b*. This value is higher than the experimental one of $\Delta r_{exp} = 0.38 \Omega$, which corresponds to $M_{\perp} = 30\%$. Both, the simulation and experiment include the AMR, but only the latter contains DWR contributions. Therefore, it is tempting to attribute the extra resistance to one or more domain walls. Micromagnetic simulations show that two domain walls exist in the

nanocontact just before the reversal (see *Fig. 4.9 d*).

From the domain walls resistance of $R_{DW} = 0.28 \Omega$ ($\Delta r_{sim} - \Delta r_{exp}$) a positive interface resistance of a single DW of $1 \times 10^{-16} \Omega \text{ m}^2$ is extracted. The formula used to obtain this value is given by [86]

$$R_{interface} = \frac{R_{DW} \times w \times t}{n} \quad (4.1)$$

where R_{DW} is the domain wall resistance (0.28Ω), w is the wall width (36 nm), t represents the wall thickness (20 nm) and n is the number of domain walls (2). An increase in resistance ($\Delta r'$) arising from the pinning of two domain walls (see *Fig. 4.9 g*) is observed experimentally in the case of a 77 nm wide nanocontact (see *Fig. 4.8 c*). This positive contribution is partly compensated by the AMR effect, which accounts for $58\% \times \Delta r'$, representing the percentage contribution of 0.38Ω from 0.66Ω . Thus, the total change in resistance caused by the two domain walls ($\Delta r' + 58\% \times \Delta r'$) is 0.19Ω , which corresponds to $6.8 \times 10^{-17} \Omega \text{ m}^2$ interface resistance of a single DW. This value agrees well with the previous experimental results of 8.3 , 6.4 , and $7.8 \times 10^{-17} \Omega \text{ m}^2$ obtained on cobalt films [33, 34, 86]. The corresponding MRs for a single DW, calculated relative to the longitudinal saturation resistance, are 0.09% and 0.055% , respectively. These values are about one order of magnitude smaller than the AMR effect.

It is shown by SQUID measurements given in *Fig. 4.3*, that a native antiferromagnetic CoO layer forms on the surface of a cobalt film when being exposed to air. In the following, the influence of the exchange bias effect on the spin-dependent transport in cobalt structures with constrictions is discussed. For this purpose, we performed magnetoresistance measurements at 4 K, cooling down in an applied magnetic field of $B = +410 \text{ mT}$. This procedure results in a uniform biased Co layer, which behaves as if it possesses a unidirectional anisotropy axis along the field cooling direction. In *Fig. 4.10* the 4 K MR curves of a 36 nm wide nanocontact are given. The cooling field direction (grey arrow) as well as the measurement configuration (magenta arrow - applied magnetic field, cyan arrow - current flow direction) are shown. Let us first discuss the case when the cooling field is applied along the long axis of the electrodes. An asymmetry in the switching field is observed, which is attributed to the exchange bias field. This is illustrated in *Fig. 4.10 a* and *b*, which shows that when the magnetization (green arrow) rotates against (black arrow) the bias field (grey arrow) the switching field is higher than in the opposite case when, the magnetization rotates towards (red arrow) the bias field. The difference between the room temperature longitudinal and transversal MR shown in *Fig. 4.4 b, c* and 4 K MR can be explained by the presence of the exchange bias field and temperature dependence of the magnetization reversal process. Thus, the merging and dissolution of two domain walls at the nanocontact, associated

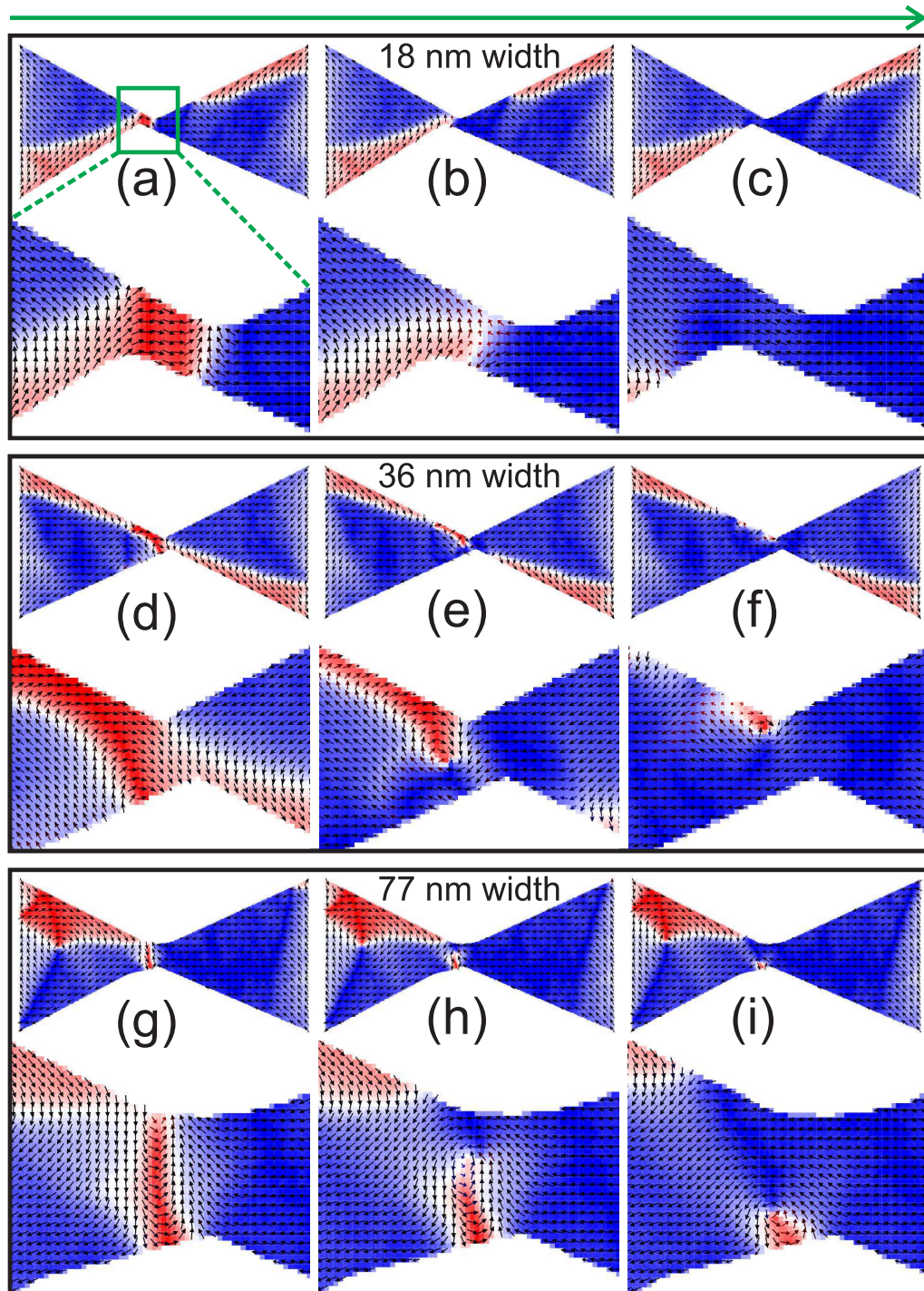


Figure 4.9: *The last stages of the simulated magnetization reversal process for three different junction widths. The lower images in each panel are extended views of the nanocontact region. The variable parameter is time indicated by the green arrow. Complicated magnetic structures involving two domain walls preface the reversal. How the domains merge and dissolve depends on the geometrical details of the nanoconstriction.*

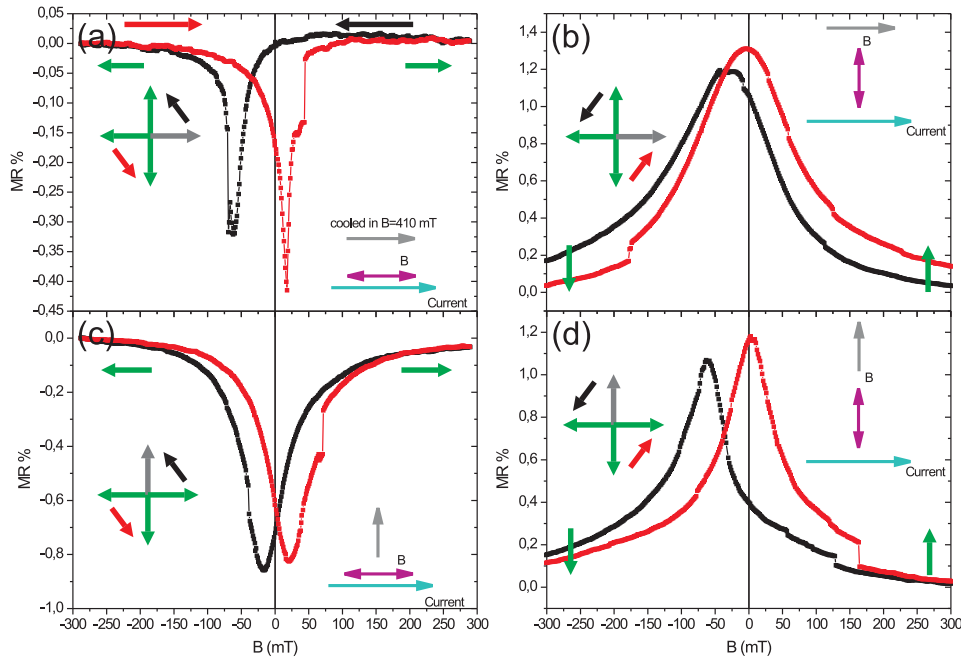


Figure 4.10: Magnetoconductance measurements of a 36 nm wide nanocontact performed at 4 K after cooling down in an magnetic field of 410 mT. The cooling field direction (shown in grey) along with the measurement configuration are given on the right side of the graphs. On the left side, a schematic representation of the magnetization reversal (green arrows) with respect to the exchange bias field (grey arrow) is shown. This drawing applies to the low-field switching region. The black and red arrows correspond to the MR traces.

with the jump in resistance in *Fig. 4.4 b*, can be hindered, at low temperatures by the bias field and pinning at defects and edges. These may play an insignificant role at room temperature, where the thermal energy is high enough to overcome them. This results in a smoother reversal at 4 K (*Fig. 4.10 a*). When the cooling field is applied perpendicular to the long axis of the electrodes (*Fig. 4.10 c and d*), a preponderant magnetization rotation is observed, which takes place between a magnetic easy axis given by the shape anisotropy and hard axis defined by the bias field. The shape of the MR and the relative resistance drop of up to 1.3% indicate that the changes in resistance are again due to the AMR effect.

4.3 Mixed electrodes: Structure B

The second structure we have investigated is shown in *Fig. 4.11*. In contrast to structure *A*, one of the electrodes is extended along the y direction in order to obtain a different nanocontact geometry and shape anisotropy and thus, to observe, if this leads to a different behavior of the magnetization at the nanocontact. Typical longitudinal and transversal MR curves along with the corresponding change in resistance are shown in *Fig. 4.11 c* and *d*, respectively. In the longitudinal configuration, an interesting aspect is the increase in resistance between $+200$ mT and $+15$ mT, which is attributed to the left electrode. As the magnetic field decreases, the magnetization in this electrode tends to follow to a larger extent the shape anisotropy. This results in transversal magnetization components before passing 0 mT and formation of domain walls. As the increase in M_{\perp} (M_y) gives a decrease in resistance due to AMR, we assigned the extra resistance to domain walls. Thus, the findings from Sec. 4.2 and Sec. 4.2 regarding the sign of DWMR are confirmed. Between $+15$ mT and 0 mT the M_{\perp} contribution exceeds that of the domain walls and the resistance decreases. In *Fig. 4.11 a* the magnetic configuration at remanence is shown. It consists of a flux-closure magnetic state for the left electrode and a predominantly monodomain-like state for the right electrode.

Reversing the magnetic field, M_{\perp} increases in both electrodes leading to a decrease in resistance with increasing magnetic field. The longitudinal MR curve of structure *B* shows an additional small jump in resistance denoted with “2”, as compared with structure *A*, suggesting a two-step switching process. Due to the larger extension of the left electrode, the formation of a reversed domain close to the nanocontact is possible at a lower magnetic field. When the field energy exceeds the shape anisotropy energy the magnetization in this domain switches to the field direction. This is an irreversible process (depinning against shape anisotropy), which corresponds to the first big jump in MR at $B = -16$ mT denoted with “1”. The expansion of the reversed domain stops at the junction resulting in a pinned domain wall. The second smaller jump at $B = -20$ mT denoted with “2” is attributed to the depinning of the end reversed domain in the right electrode. This takes place at about the same magnetic field as in structure *A* accompanying the complete reversal of the elongated electrode and the dissolution of the domain wall pinned at the junction. At this stage the left electrode is not completely switched, the resistance having a larger value as compared with the saturation. This can be explained by a positive DWMR contribution, which exceeds the AMR. The magnetization reversal process ends at saturation, when the magnetization throughout the sample aligns with the applied negative magnetic field.

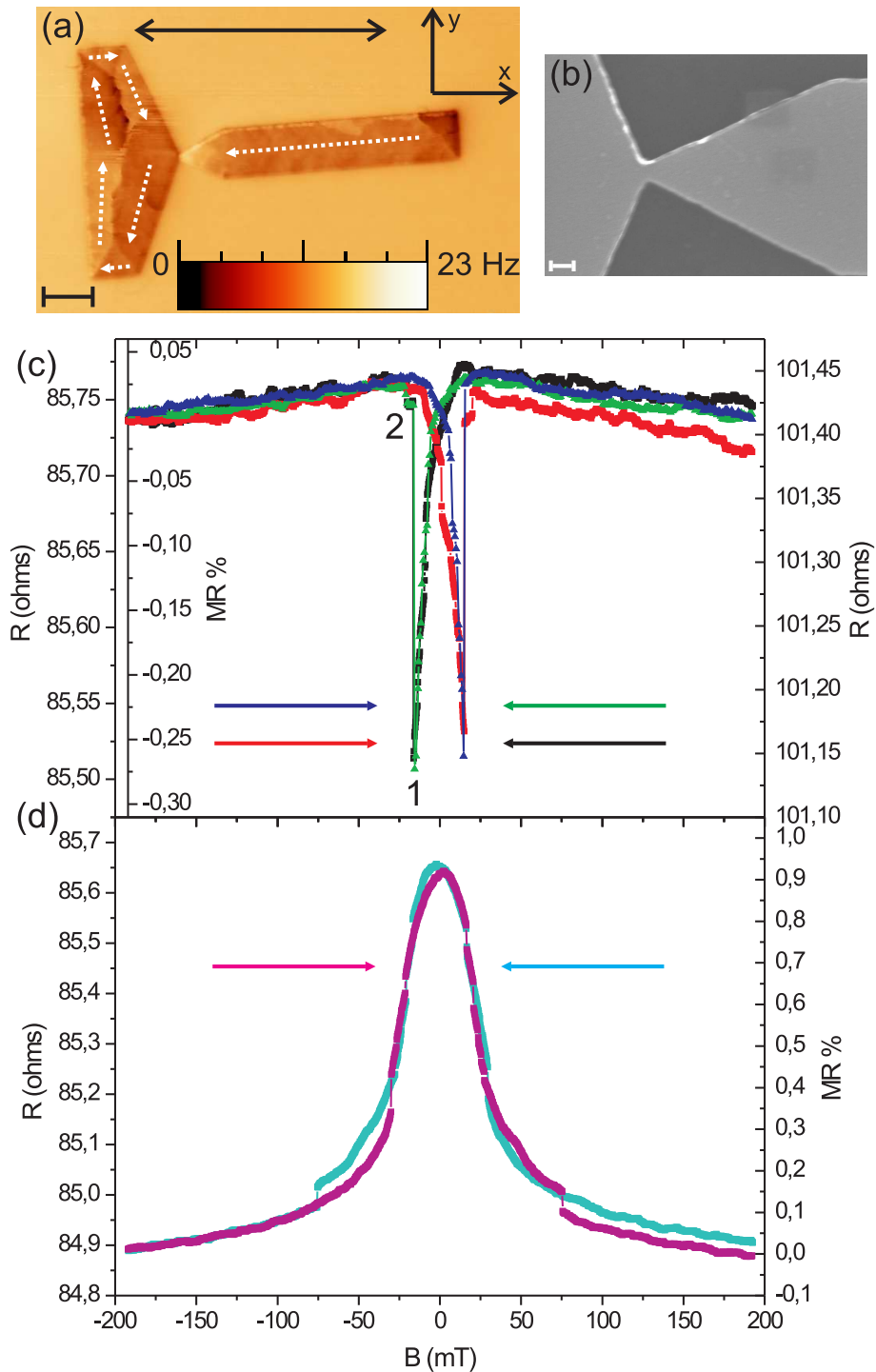


Figure 4.11: (a) MFM image at remanence following saturation along the $-x$ direction. The scale bar is $1 \mu\text{m}$. The double arrow represent the scanning direction, while the dotted arrows the inferred magnetization configuration. (b) SEM image of the 85 nm wide nanocontact. The scale bar is 100 nm . (c) Comparison of longitudinal MR measurements on two nanocontacts: 45 nm (triangles) and 85 nm (squares). The arrows show the sweep directions. (d) Transversal MR curve of the 85 nm wide nanoconstriction.

In the transversal configuration a small hysteresis appears in MR around zero magnetic field when returning from saturation as compared with the structure *A*. Its presence indicates a magnetic anisotropy along the long axis of the left electrode, which is favored at low magnetic fields. The main contribution to the magnetization reversal process is given by the right electrode. The reversal can be described by predominantly coherent rotation of the magnetization between the magnetic easy axis and hard axis (defined by the shape anisotropy) of the right electrode. The general shape of the curves and the values of the MR are consistent with the AMR effect.

In the following the results of the micromagnetic simulations on the 85 nm wide nanocontact are discussed. They are shown in *Fig. 4.12*: top panel - longitudinal configuration and bottom panel - transversal configuration. When the longitudinal magnetic field decreases from positive saturation (image *a2*) towards zero (*a3*), the magnetization at the electrode's edges rotates in order to lower the magnetostatic energy. This process depends on the shape anisotropy of the two electrodes. While the right electrode remains mostly homogeneously magnetized along the $+x$ direction, a magnetic pattern resembling a flux-closure state develops in the left electrode. The presence of domain walls and domains with transversal magnetization components support the picture of an interplay between these contributions, which was used to explain the measured MR before passing 0 mT. Applying a negative magnetic field, reversed domains develop in the electrodes by magnetization rotation and domain wall movement (*a4* to *a9*). While for the right electrode an end reversed domain expands towards the nanocontact, for the left one a reversed domain develops close to the junction. The reversal in the nanocontact region occurs when the domains on each side of the junction merge and dissolve (*a9* to *a13*). This would correspond to a single jump in resistance as shown in the case of structure *A*. This discrepancy can be explained taking into account the effect of scaling down the sample size on the simulation results. We suggest that in the simulation the domain wall, which crosses the left electrode hinders the formation of a reversed domain at a lower magnetic field, as observed in the experiment. The presence of this domain wall was confirmed experimentally by MFM, but in the real sample it was situated at about 1 μm away from the nanocontact, as compared to about 125 nm in the simulation. At this stage (*a14*) the left electrode is not completely reversed, part of the transversal domain wall being still present. This configuration can be associated with the high resistance state after the second switching. The decrease in resistance towards saturation corresponds to the wiping of domain walls out from the sample (*a15*).

The calculated evolution of the magnetization for the transversal case is shown in *Fig. 4.12* - bottom panel. Returning from positive saturation (image *b1*) towards zero (*b2*) the magnetization aligns parallel to the

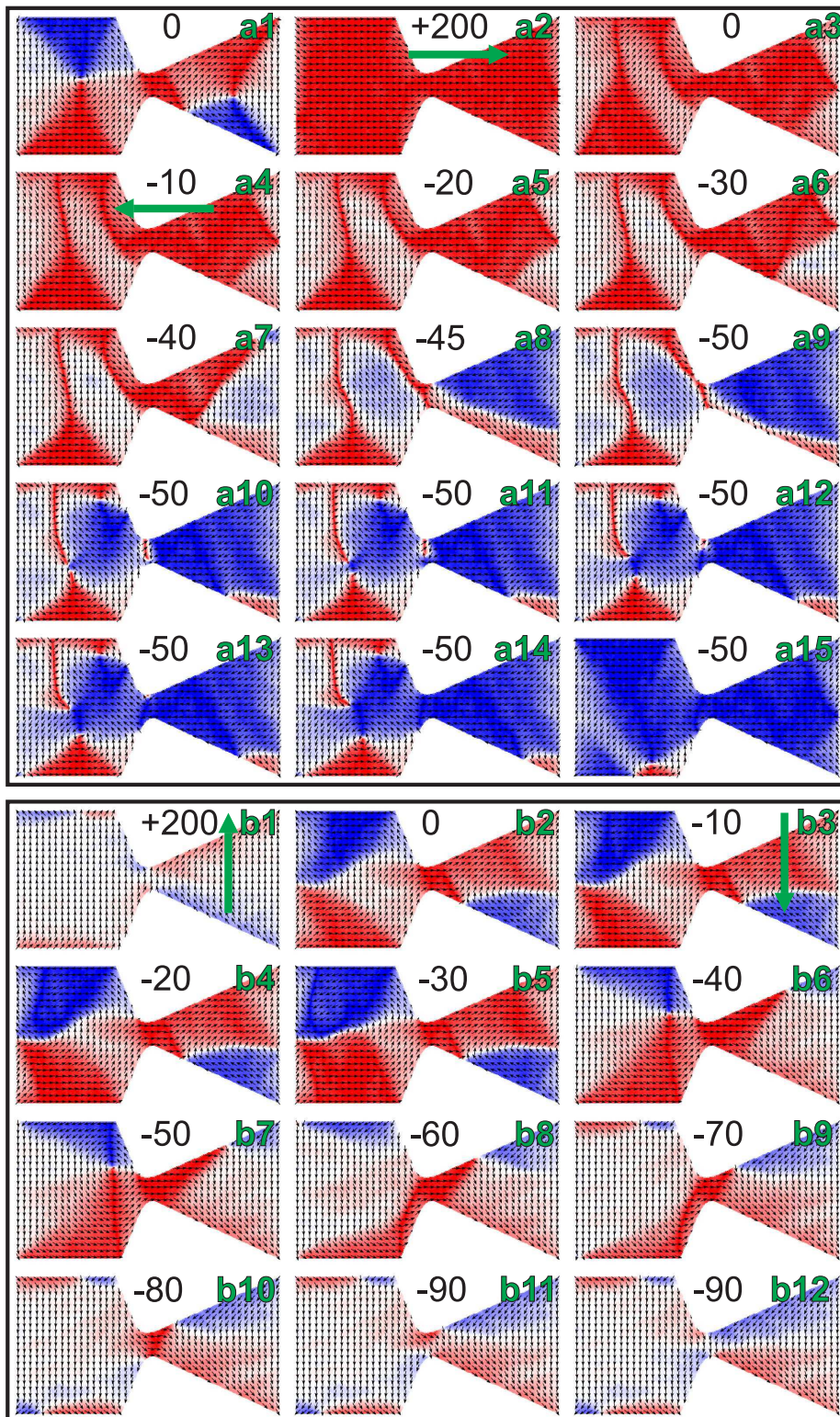


Figure 4.12: The simulated evolution of the magnetization with the magnetic field applied along x direction (longitudinal - top panel) and y direction (transversal - bottom panel). The reference on the images represents their index (right corner) and the applied magnetic field in mT (above the junction). At the same magnetic field the difference is given by the simulation time. The green arrows on (a2, a4, b1, b3) emphasize the direction of the magnetic field.

nanocontact's axis and rotates in the electrodes to minimize the magnetostatic energy and follow the shape anisotropy. Applying a negative magnetic field, reversed domains develop in the electrodes mostly by magnetization rotation and domain wall movement. An interesting aspect during the reversal process is the creation of a vortex in the left electrode (b6), which is then expelled from the structure (b7, b8). The reversed domains extend in the electrodes approaching the nanocontact (b3 to b9), which is the last region reversed by magnetization rotation (b10 to b12).

In Fig. 4.13 the 4 K MR on a 85 nm wide nanocontact are shown. Since the physics involved in the magnetization reversal process is similar to that described for structure A, only the differences will be discussed. The first difference is the increase of the switching field from - 62 to - 90 mT (graph a), which can be explained by the increase of the exchange bias field due to the extension of the left electrode [87]. The second difference is the shift to the right of the red curve in Fig. 4.13 b, which indicates a magnetic anisotropy along the long axis of the left electrode. The shape of the MR and the relative resistance drop of up to 1.2% indicate that the changes in resistance are due to the AMR effect.

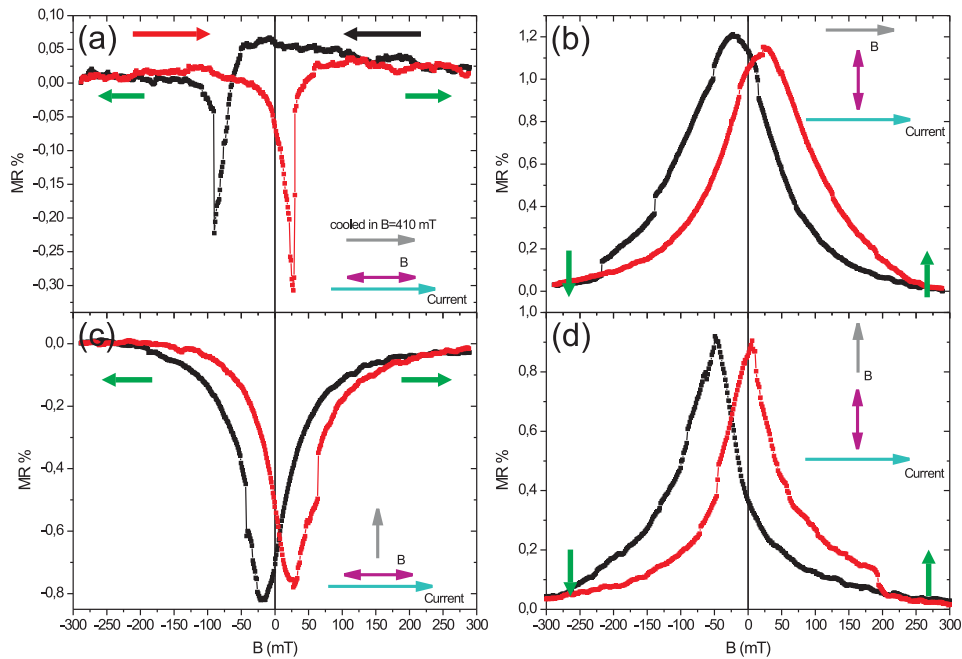


Figure 4.13: MR measurements of a 85 nm wide nanocontact at 4 K after cooling down in an magnetic field of 410 mT. The cooling field direction (grey arrow) along with the measurement configuration are shown on the right side of the graphs. The black and red arrows indicate the sweep directions.

4.4 “Butterfly” electrodes: Structure C

The third structure we have studied consists of two identical electrodes extended in the y direction resembling butterfly wings. An MFM image taken at remanence following positive saturation is shown in *Fig. 4.14 a*. A flux-closure magnetic state for both electrodes is observed. Characteristic for such a butterfly-like structure are the step-like MR traces recorded for both measurement configurations as shown in *Fig. 4.15* where magnetotransport curves for two structures and successive measurements are presented. The position and the number of steps are not fully reproducible, since the magnetization can follow more than one path each time the process is repeated. These steps are found to be distinct irreversible states as traced by minor-loop MR measurements given in *Fig. 4.16 e* and *f*.

When returning from saturation with a magnetic field applied longitudinally the resistance increases with twice the slope observed for structure *B* up to + 13 mT. Like in the previous case (structure *B*) the extra resistance is attributed to domain walls, which now appear in both electrodes. After + 13 mT the resistance starts to decrease due to the increase in M_{\perp} reaching a remanent state like that shown in *Fig. 4.14 a*. The step-like switching, which follows after passing 0 mT is attributed to the changes in the magnetic configuration around the junction. This is confirmed by MR measurements taken on a highly asymmetric nanocontact, which developed due to electromigration after successive loops on the structure shown in *Fig. 4.16 a*. Such a nanocontact behaves like a domain wall diode [85], with different pinning potentials on each side of the junction, resulting in an asymmetric MR. The mirror reversal observed after rotating the sample by 180° (see *Fig. 4.16 d*) clearly indicates that the step-like MR originates from the nanocontact and its proximity. The similarity in the high-field MR

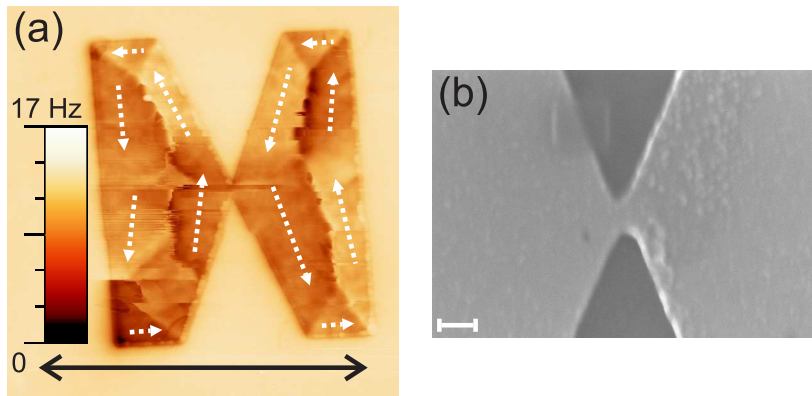


Figure 4.14: (a) MFM image taken at remanence coming from positive saturation (+x). The double arrow represent the scanning procedure. The white arrows show the inferred magnetic configuration. (b) SEM image of the nanocontact.

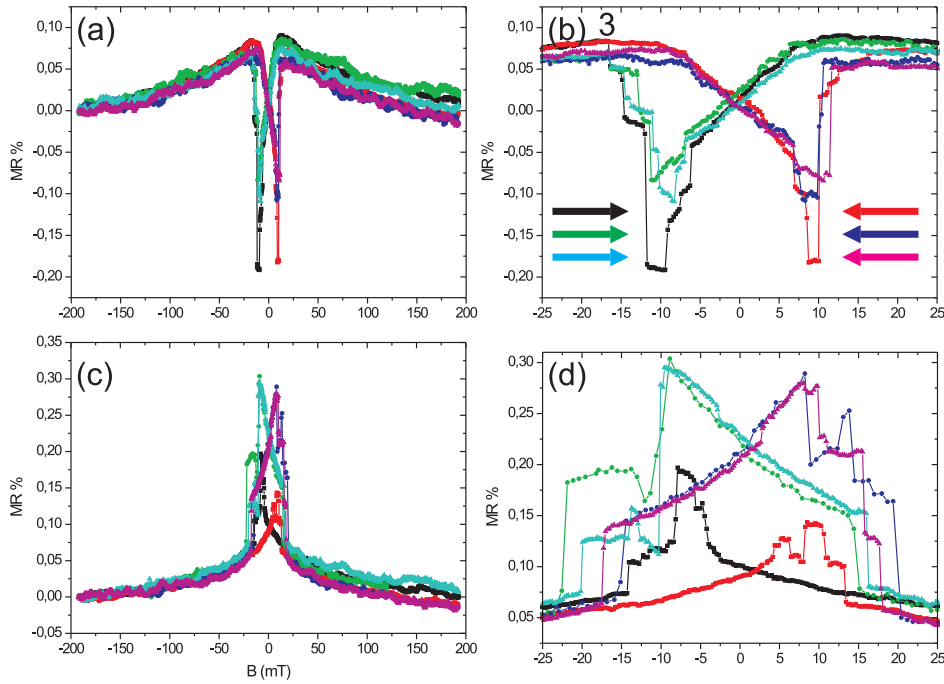


Figure 4.15: MR traces of two different nanocontacts (83 nm wide): (a) longitudinal configuration, (b) extended view of (a), (c) transversal configuration, (d) extended view of (c). The arrows are associated with the symbols - sample 1 (squares), sample 2, first measurement (circles), sample 2, second measurement (triangles) - and show the sweep directions.

constitutes an additional proof that the electrodes do not contribute to the low-field MR. Their contributions are invariant to a 180° rotation. By comparing the first jump in MR denoted with “1” for structure *B* (see Fig. 4.11) with the last jump denoted with “3” for structure *C* (see Fig. 4.15 b), it can be seen that they take place at about the same magnetic field. While in the former case it is attributed to the switching towards the field direction, we assign it now to two reversed domains approaching the nanocontact from both sides and merging in the nanocontact. The steps can be associated with different positions of the two domain walls relative to the junction, while the plateaus relate to the pinning at these positions.

The transverse MR curves presented in Fig. 4.15 c and d show a pronounced hysteretic behavior as compared to the findings on structure *B*. Its presence indicates a magnetic anisotropy along the long axis of the electrodes, which is favored at low magnetic fields. The general shape of the curves and the values of the MR are consistent with the AMR effect.

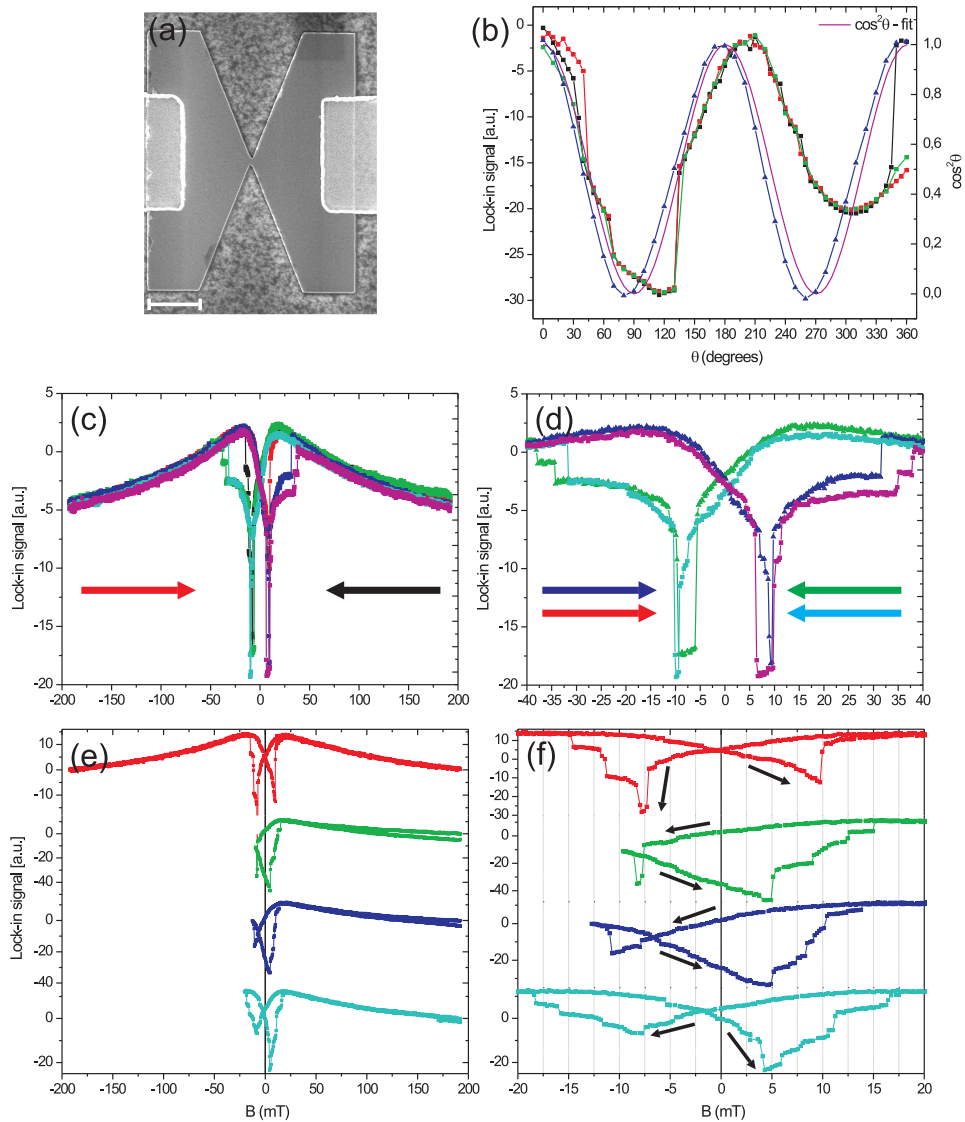


Figure 4.16: (a) SEM image of a 82 nm wide junction before MR measurements. (b) Angular dependence of resistance at saturation (triangles) and at $B = -10$ mT coming from positive saturation (squares, there successive measurements shown in black, red and green). The magenta curve represents the AMR theoretical fit. (c) Longitudinal MR loops showing the transition from a less (black and red) to a highly asymmetric nanocontact. (d) extended view of (c) emphasizing the mirror reversals measured on a highly asymmetric nanocontact after rotating the sample by 180° . (e) Longitudinal minor loops. (f) zoom of (e) in the low-field region. The black arrows represent the measurement procedure, starting from positive saturation.

In the following the results of the micromagnetic simulations on the 83 nm wide nanocontact are discussed. They are shown in *Fig. 4.17*: top panel - longitudinal configuration and bottom panel - transversal configuration. When the longitudinal magnetic field decreases from positive saturation (image *a1*) towards zero (*a2*), the magnetization at the electrode's edges rotates in order to lower the magnetostatic energy. Applying a negative magnetic field, reversed domains develop in the electrodes by magnetization rotation and domain wall movement (*a3* to *a8*). The reversal in the nanocontact region occurs when the domains on each side of the junction merge and dissolve (*a8* to *a11*). At this stage (*a11*) the right electrode is not completely reversed, part of the transversal domain wall being still present. This configuration can be associated with the high resistance state after the last switching event denoted with "3" in *Fig. 4.15 b*. The decrease in resistance towards saturation corresponds to the wiping out of domain walls from the sample (*a12*). The observed steps in MR could not be unambiguously identified in the micromagnetic simulations. The correspondence between the steps and magnetic configurations can be obtained by computing the AMR curves [88].

The calculated evolution of the magnetization for the transversal case is shown in *Fig. 4.17* - bottom panel. Returning from positive saturation (image *b1*) towards zero (*b2*) the magnetization rotates in the electrodes to minimize the magnetostatic energy and follow the shape anisotropy. The magnetization reversal process can be divided into three stages. In the first stage, magnetization rotation and domain wall movement drive the reversal until two vortices, one in each electrode, are formed (*b3* to *b6*). In the second stage, the vortices are moved by the field against the sample's edges and expelled from the electrodes (*b6* to *b9*), accompanying the reversal of the electrodes. In the last stage, a coherent magnetization rotation takes place in the nanocontact (*b10* to *b12*), resulting in a completely saturated structure. Again, it is difficult to make a correspondence between experiment and simulation.

The angular dependence of resistance at saturation and at $B = -10$ mT following positive saturation is presented in *Fig. 4.16 b*. While the former fits well with an AMR $\cos^2\theta$ profile (see Sec. 2.2), the latter exhibits a significant deviation. This can be explained by the presence of domains and domain walls in the switching region. In this case the $\cos^2\theta$ dependence, which applies to single domain structure does not fully describe the MR. Nevertheless, the general shape and the value of the MR point towards a major contribution from AMR.

In *Fig. 4.18* the 4 K MR on a 83 nm wide nanocontact are shown. Two types of measurements were performed: cooling down in an applied magnetic field of $B = +410$ mT (graph *a* and *c*) and zero magnetic field (graph *b, d* and *e*). It was shown by SQUID measurements given in *Fig. 4.3*

that in the zero field cooling (ZFC) case the exchange bias varies locally throughout the sample due to the random distribution of the CoO magnetic moments. This was confirmed by successive MR measurements on the same sample, in the ZFC case. They are presented in *Fig. 4.18 b, d* in and *e*. It can be seen that the first trace in each graph (squares, backward sweep - black arrows, forward sweep - red arrows) is different from the second trace (circles, green/blue arrows). When cooling down in a magnetic field, successive MR curves are almost similar. The small difference is due to the training effect [84]. The switching field (graph *a*) continues to increase from -90 mT (for structure *B*) to -110 mT, supporting the picture of the increase in the exchange bias field with the electrodes area [87]. The pronounced hysteretic behavior in *Fig. 4.18 c* indicates a magnetic anisotropy along the long axis of the electrodes. The shape of the MR and the relative resistance drop of up to 0.5% indicate that the changes in resistance are due to the AMR effect.

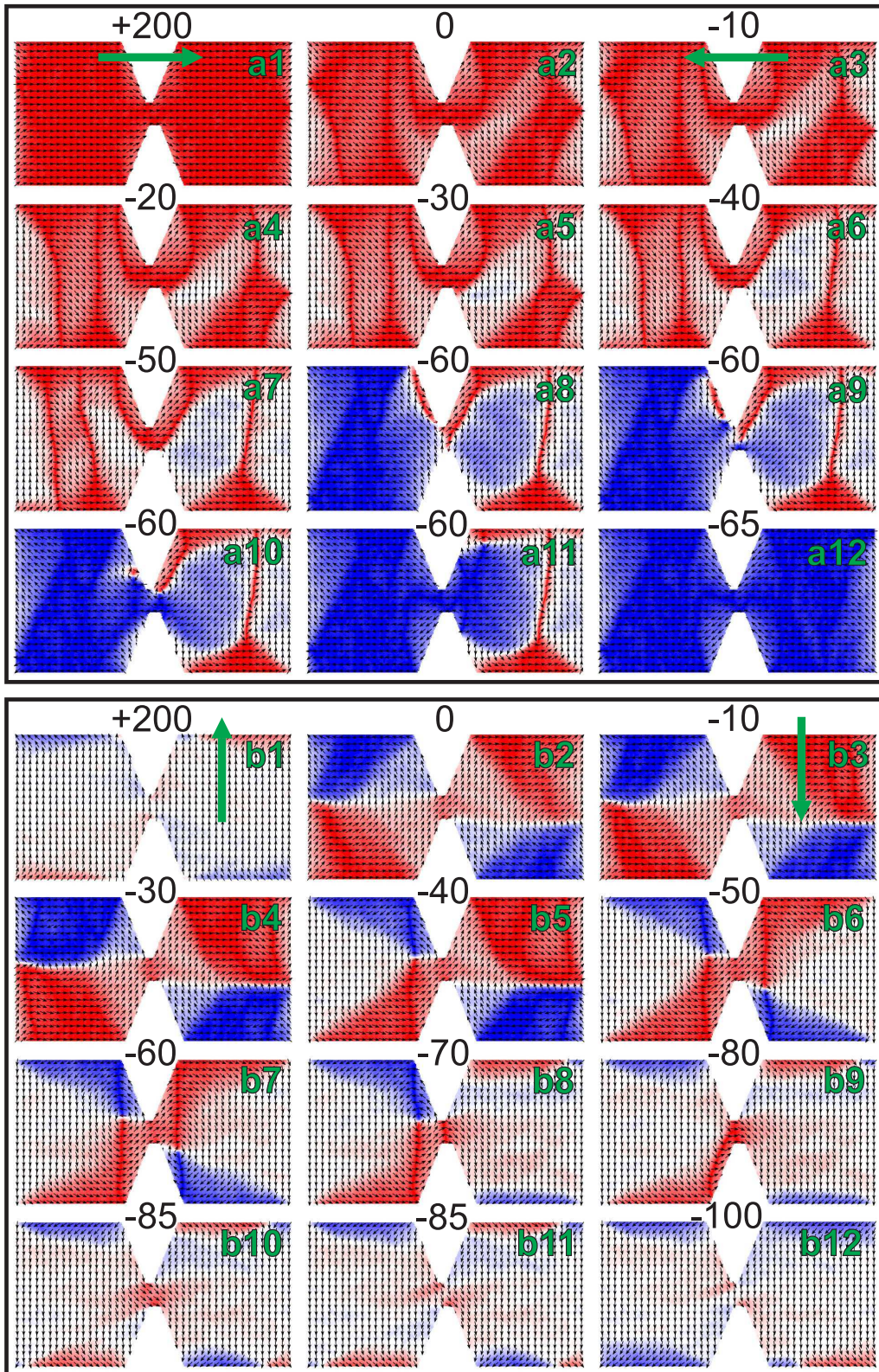


Figure 4.17: The simulated evolution of the magnetization with the magnetic field applied along x direction (longitudinal - top panel) and y direction (transversal - bottom panel). The reference on the images represents their index (right corner) and the applied magnetic field in mT (above the junction). At the same magnetic field the difference is given by the simulation time. The green arrows on (a1, a3, b1, b3) emphasize the direction of the magnetic field.

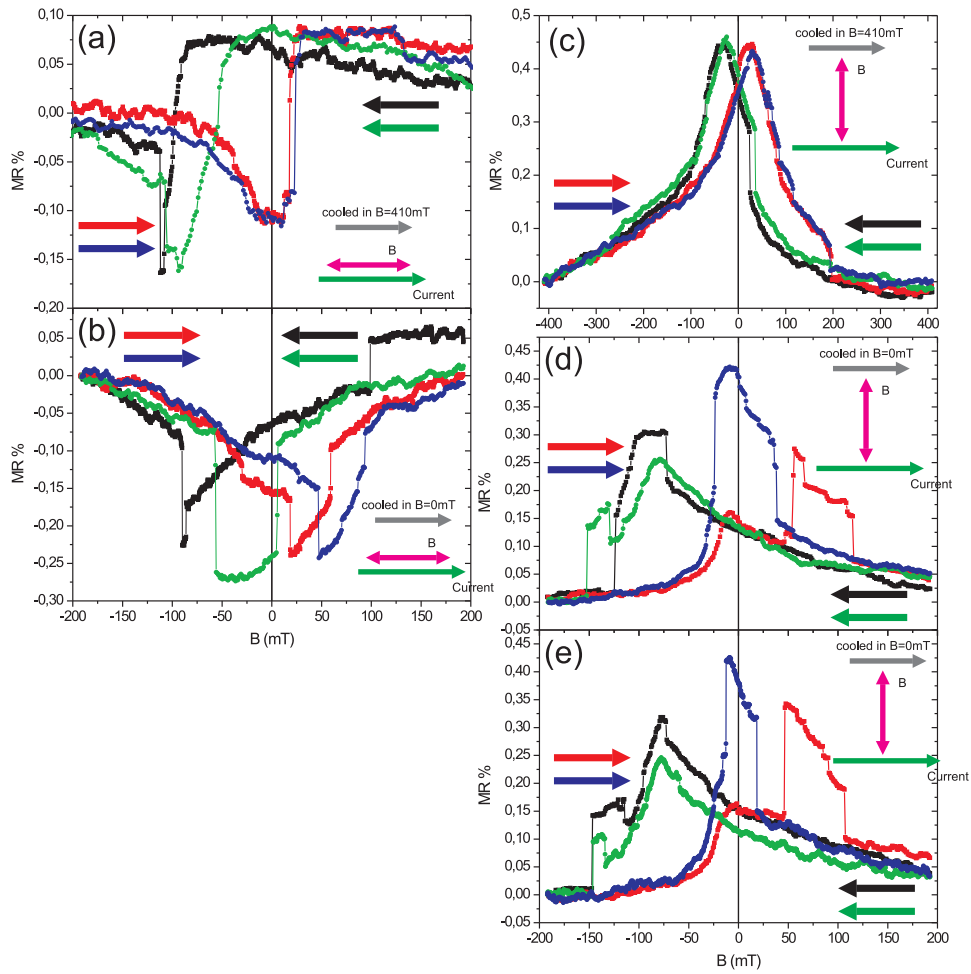


Figure 4.18: Magnetoresistance measurements of a 83 nm wide nanocontact performed at 4 K after cooling down in an magnetic field of 410 mT (a) and (c) and zero magnetic field (b), (d) and (e). The black/red and green/blue arrows on the graphs represent successive measurements and indicate the magnetic field sweep directions. The cooling field direction (shown in grey) along with the measurement configuration are given on the right side of the graphs.

Chapter 5

Conclusions and Outlook

Controlling the magnetization configuration of a ferromagnetic nanostructure and understanding its reversal is relevant for all magnetic device applications. In confined systems such as magnetic nanocontacts or ferromagnetically contacted carbon nanotubes [92, 93], the direct observation of the magnetization distribution during the reversal process is hard to be achieved. These systems are usually investigated by magnetoresistance (MR) measurements, which serve as a non-invasive probe, based on AMR, GMR or TMR effects. Micromagnetic simulations are used to get insight into the underlying magnetization reversal giving rise to the measured MR signal.

In this thesis, 20 nm thick cobalt films and structures with constrictions have been investigated at room temperature and 4 K. A new lithographic approach combining the proximity effect of electron beam lithography with a special layout design has been used to fabricate the nanocontacts. In order to give the reader a complete view of the experimental work, representative MR curves of all structures are given on the same figure. In the longitudinal configuration, *Fig. 5.1 a* and *b*, due to the extension of individual electrodes along the y direction (structure *B*, *C* and *C1*), transversal magnetization components and domain walls develop in the extended electrodes. The increase of the reversible high-field MR (region “1”) with increasing the width of individual electrodes is attributed to a positive contribution coming from the formation of domain walls in the electrodes since the transversal magnetization results in a decrease in resistance due to AMR. The domain walls contribution is overcome by AMR towards zero magnetic field (region “2”), resulting in a decrease in resistance. The second part of the low-field MR (region “3”) is attributed to the nanocontact region and was found to depend on both nanocontact shape and width. The different nanocontact geometries with different shape anisotropies result in a different behavior of the magnetization at the nanocotact. A transition from a sharp switching process (structure *A* and *B*) associated with two domains merging and

dissolving in the nanocontact (irreversible switching event) to a step-like MR (structure C and $C1$) is observed. The steps (irreversible events) are associated with different positions of the two domain walls relative to the junction, while the plateaus to the pinning at these positions (reversible events). The presence of domain walls at the nanocontact, in the low-field region, is confirmed by minor MR loops and micromagnetic calculations. In the transversal configuration, *Fig. 5.1 c* and *d*, the high-field MR does not show a significant dependence on the width of the electrodes because the reversal is dominated by magnetization rotation rather than domain wall formation. In the low-field region, a transition from no/small hysteretic MR (structure A/B) - predominantly coherent rotation of the magnetization between the magnetic easy axis and hard axis (reversible event) - to a pronounced hysteresis (structure C and $C1$) due to the shape anisotropy, which is favored at low fields, is observed.

Our room temperature experiments show the feasibility of engineering of switching fields and reversible/irreversible magnetization reversals in magnetic nanostructures with constrictions using shape anisotropy, which is of potential use for the implementation of optimized read heads in ultra-high-density memory devices [89]. Magnetic domain-wall logic [90] and magnetic race-track memory [91] are other emerging device applications which may require tuning of the same parameters. Moreover, we show that the electrodes contribution in confined systems can be separated from the confined part's contribution.

Micromagnetic simulations show that the nanocontact region is the last reversed area. Reversed domains develop in the electrodes almost simultaneously because of their large widths, leading to a parallel alignment of magnetization in the electrodes and two domain walls on each side of the nanoconstriction. The nature and dynamics of the two domain walls around the nanocontact could also be revealed by micromagnetic simulations. The magnetization reversal takes place either by merging and dissolving of the two domain walls or magnetization rotation in the nanocontact. How the domains merge and dissolve depends on the geometrical details of the nanoconstriction. In both cases no sharp domain wall, which may lead to ballistic magnetoresistance (BMR), develops at the nanocontact. We suggest that the tip-to-tip geometry with μm large electrodes can lead to a sharp domain wall across the constriction when an atomic point nanocontact is formed [24]. In this case, the nanocontact is magnetically decoupled from the extended electrodes, resulting in a separated reversal of the atoms forming the nanocontact, which may lead to an atomically sharp domain wall in the antiferromagnetically aligned state.

By comparing the calculated evolution of the magnetization components integrated over the structure to the shape of the measured MR, it can be concluded that the AMR is the dominant resistance contribution in our

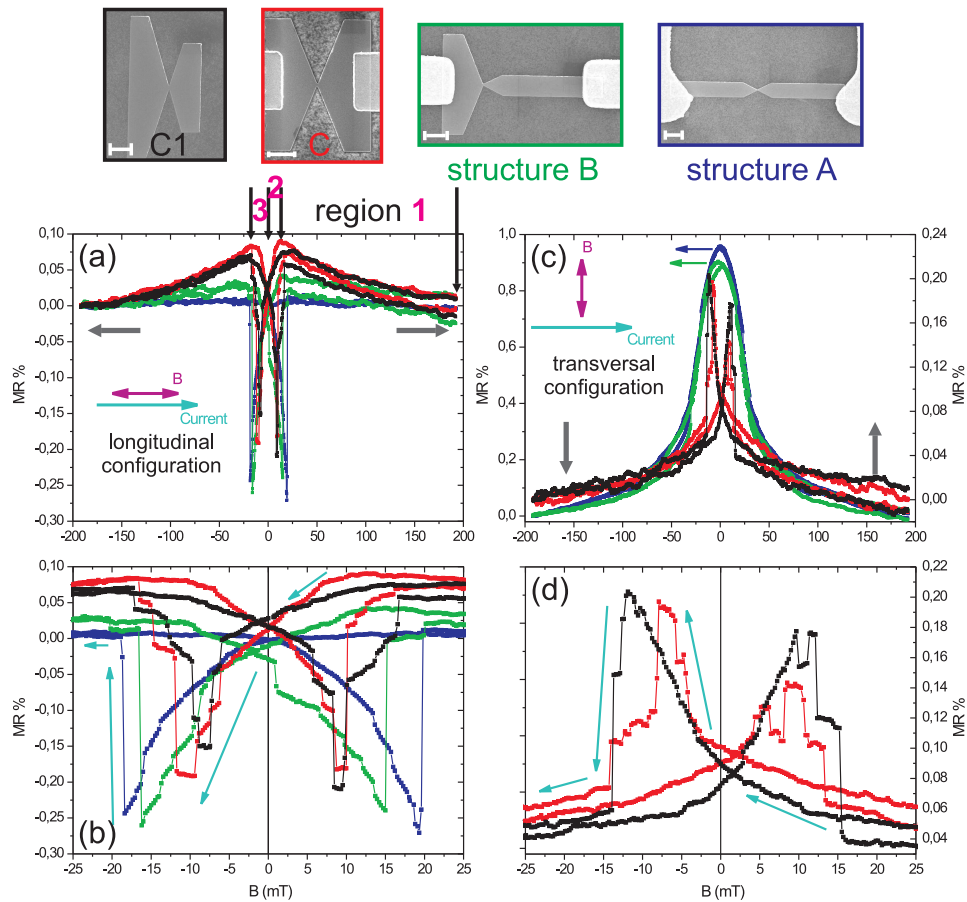


Figure 5.1: Review of room temperature magnetoresistance measurements. Structure C1 is a larger version of structure C and was not discussed in chapter 4. The colored borders of the SEM images correspond to the same colors on the graphs. The scale bars are $1\ \mu\text{m}$. The grey arrows represent the saturation magnetization. (a) Longitudinal MR. The backward sweep direction is divided in three regions denoted with 1, 2 and 3. (b) Extended view of (a) in the switching region. (c) Transversal MR. The green and blue arrows indicate towards the axis to be considered. (d) Zoom of (c) in the switching region for structures C and C1. The cyan arrows indicate the backward sweep direction.

structures. In the longitudinal configuration, the increase in the transversal magnetization components before switching is qualitatively consistent with the resistance decrease observed in *Fig. 5.1 a* - region “3” and *b*, which shows a minimum when magnetization is perpendicular to the current flow direction. In the transversal configuration, the increase in the longitudinal magnetization components before zero magnetic field (structure *A* and *B*) and the switching (structure *C* and *C1*) is qualitatively consistent with the resistance increase observed in *Fig. 5.1 c* and *d*, which shows a maximum when magnetization is parallel to the current flow direction. Moreover, the experimental MR values of up to 1% are consistent with the AMR interpretation.

The presence of domain walls in the nanocontact region suggests that besides AMR, DWMR contributes to the measured signal. The simulation and experiment include the AMR, but only the latter contains DWMR contributions. Considering the calculated longitudinal magnetization configuration before switching (for structure *A*), a higher drop in resistance as compared with the experiment is found. The extra resistance is attributed to the presence of one or more domain walls at the nanocontact. An average positive interface resistance of a single domain wall of $8.4 \times 10^{-7} \Omega\text{m}^2$, which agrees well with the previous experimental results obtained on cobalt films [33, 34, 86], and a domain wall magnetoresistance of 0.07% are estimated. The smallest cobalt nanocontact measured in this thesis was 18 nm wide, which corresponds to the diffusive regime of DWMR. In view of the fact that DWMR contribution in this regime is embedded in AMR, the combination of experiment and simulation may prove a straightforward approach to determine the sign and magnitude of DWMR in magnetic nanostructures.

It was shown by SQUID measurements that a native antiferromagnetic CoO layer forms on the surface of a cobalt film when being exposed to air. When the Co/CoO system is cooled below the Néel temperature of the antiferromagnet ($T_N \approx 290\text{K}$), the Co layer is biased due to the exchange bias effect [84]. The 4 K MR measurements, *Fig. 5.2*, are found to depend on the cooling procedure. When cooling down in an applied magnetic field, a uniform biased Co layer is formed, resulting in a unidirectional anisotropy axis along the field cooling direction. The magnetization reversal takes place either by preponderant domain formation or magnetization rotation between the two axes defined by the shape anisotropy and bias field. The difference between the room temperature MR shown in *Fig. 5.1* and 4 K MR are explained by the presence of the exchange bias field and temperature dependence of the magnetization reversal process. The asymmetry in the switching fields is attributed to the exchange bias field. The switching field is higher when the magnetization rotates against the bias field than in the opposite case when it rotates towards the bias field. The increase in the negative switching field (*Fig. 5.2 a*) is explained by an increase in the

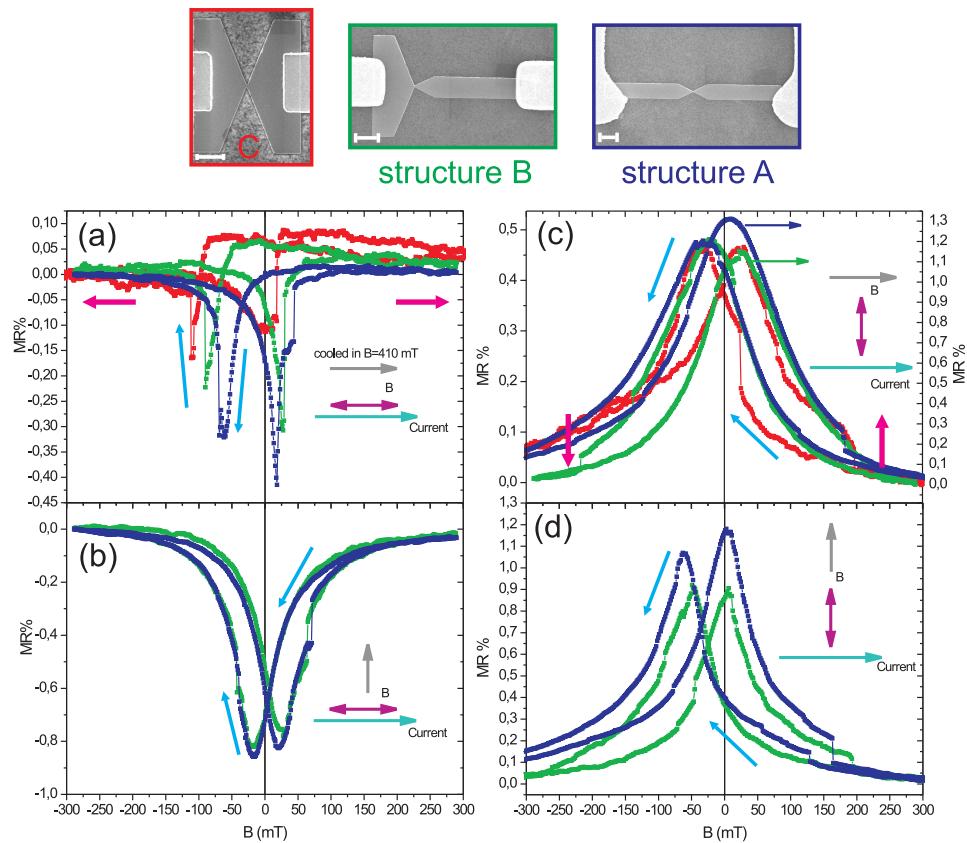


Figure 5.2: Review of 4 K magnetoresistance measurements performed after cooling down in a magnetic field of 410 mT. The cooling field direction (shown in grey) along with the measurement configuration are given on the right side of the graphs. The red arrows represent the saturation magnetization.

exchange bias field with the electrodes area [87]. The magnetization reversal is smoother at 4 K because it is hindered by the bias field and pinning at defects and edges. In the zero field cooling case, there is no defined bias field anisotropy direction due to the random distribution of the CoO magnetic moments. This results in non-reproducible successive MR traces. These experiments emphasize the importance of the cooling procedure on the spin-dependent transport measurements in exchange biased confined systems. They also offer an additional path to separate the switching fields between two electrodes among which one is exchange biased.

The results of this thesis may be of importance for future studies of the spin-dependent transport, particularly in 1-dimensional systems. Carbon nanotubes (CNTs) represent a very interesting confined system of 1D topology. They exhibit ballistic conduction [94] and a long spin relaxation time [95] (when ferromagnetic contacts are used to inject a spin-polarized current), which allow spin manipulation during transfer process [96]. Although, the different signs and amplitudes of the MR found in experiments can be theoretically explained, a further control of the switching behavior of the magnetic electrodes [97], understanding and optimization of the contact properties [98], and understanding of the influence of the intrinsic property of the carbon nanotube on the MR [99] are needed. Based on the results of this thesis we suggest that in case of spin-dependent transport in carbon nanotubes the electrodes may consist of a narrow magnetic wire with a constriction defined along its length and a large pad at one end of the wire. In this way, the magnetization configuration and reversal of the electrodes can be controlled: by positioning a large pad at one end of the wire, a wall is reproducibly nucleated at the point where the pad joins onto the wire [23] when a magnetic field is applied opposite to the direction in which the sample was saturated, continuing increasing the field the wall is injected into the wire and moves until is pinned at the constriction. Using two similar electrodes, parallel and antiparallel configurations can be realized, as shown in *Fig. 5.3*. Another advantage of this geometry is the absence of stray fields, which are generated in extended ferromagnetic electrodes due to magnetization rotation, near the contact with the nanotube.

The transparency of the contacts sets the regime of the electronic transport. For high contact resistances $R > h/e^2$, a nanotube can behave as a quantum dot, in which the Coulomb blockade determines the transport properties [100], whereas for low contact resistances $R < h/e^2$, transport is mainly determined by quantum interference [101]. It has been shown [98] that for understanding the physics leading to the MR effect, it is essential to determine the different characteristic energies (charge energy or energy spacing), which set the behavior of the nanotube. This can be realized by measuring the conductance as a function of the gate voltage (V_g) and source-drain voltage (V_{sd}). While this was done in a two-point geom-

etry, we suggest to combine it with a four-point experiment [102]. Using four identical magnetic electrodes as those shown in *Fig. 5.3* connecting the same nanotube with the same gap between them, two sets of identical measurements (conductance *vs.* V_g and V_{sd}) have to be performed in both configurations. The two-terminal resistance measured between the two inner electrodes includes the resistance originating from the nanotube (R_{NT}) and the contact resistances at the electrodes ($R_{contact} = R_{c1} + R_{c2}$), while the four-terminal resistance includes the nanotube resistance (R_{NT}) between the two inner electrodes. Thus, the gate and source-drain - induced change can be attributed to the intrinsic property of carbon nanotube (R_{NT}) or contact effects ($R_{contact}$). This final example suggests only one of the future research directions, which can make use of this thesis's results.

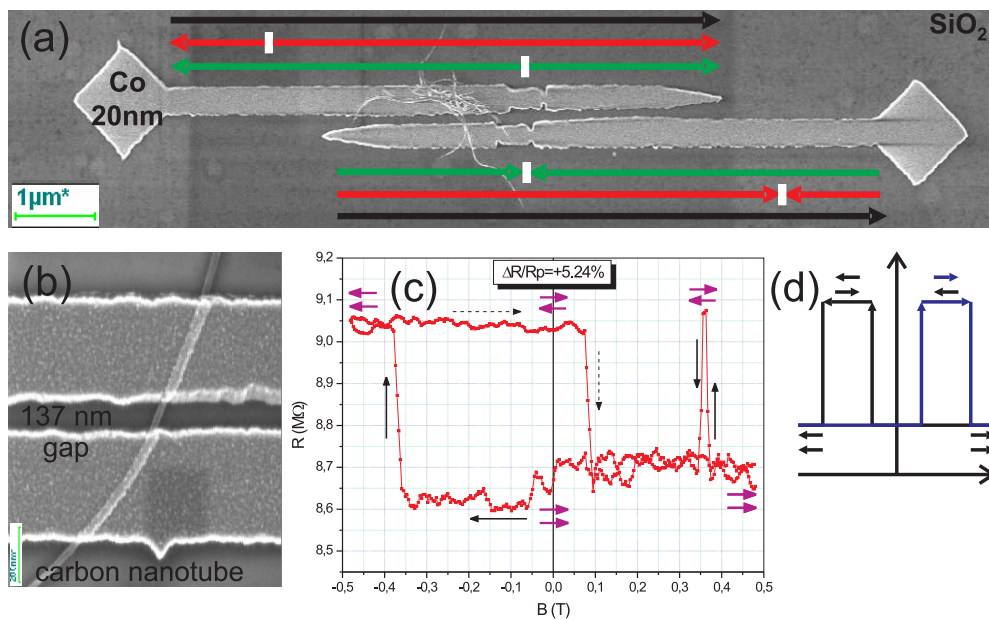


Figure 5.3: (a) SEM image of a test carbon nanotube device consisting of two identical electrodes on top of a bundle of single-wall carbon nanotubes. The large pad at one end of the wire is used to inject a domain wall (white rectangle) into the wire when a magnetic field is applied opposite to the direction in which the electrodes were saturated (black arrows). The triangle shape of the other wire's end hinders the formation of reversed domains. A parallel (red arrows) and antiparallel (green arrows) configurations at the nanotube's contacts can be realized. (b) SEM image of another carbon nanotube device taken at the nanotube's contacts. (c) An example of a spin-dependent transport trace measured on the device presented in (a) - preliminary results. (d) The expected magnetoresistance response providing that the electrodes exhibit reversal by domain wall movement and the contacts to the nanotube and nanotube itself do not change the spin orientation during the injection, transport and detection processes.

References

- [1] G. Binash, P. Grünberg, F. Saurenbach, and W. Zinn, Enhanced Magnetoresistance in Layered Magnetic Structures with Antiferromagnetic Interlayer Exchange, *Phys. Rev. B* 39, 4828 (1989).
- [2] M. Baibich, J. Broto, A. Fert, F. v. Dau, F. Petroff, P. Etienne, G. Greuzet, A. Friederich, and J. Chazelas, Giant Magnetoresistance of (001)Fe/(001)Cr Magnetic Superlattices, *Phys. Rev. Lett.* 61, 2472 (1988).
- [3] S. S. P. Parkin, R. Bhadra, and K. P. Roche, Oscillatory magnetic exchange coupling through thin copper layers, *Phys. Rev. Lett.* 66, 2152 (1991).
- [4] W. J. Gallagher and S. S. P. Parkin, Development of the magnetic tunnel junction MRAM at IBM: From first junctions to a 16-Mb MRAM demonstrator chip, *IBM Journal of Research and Development* 50, 5 (2006).
- [5] Guo-Qiang Gong, Chadwick Canedy, Gang Xiao, Jonathan Z. Sun, Arunava Gupta, and William J. Gallagher, Colossal magnetoresistance of 1 000 000-fold magnitude achieved in the antiferromagnetic phase of $La_{1-x}Ca_xMnO_3$, *Appl. Phys. Lett.* 67, 1783 (1995).
- [6] P. Weiss (1907) *Journal de Physique theorique et appliquee* 6 666-690.
- [7] Ampère, A. M. (1827) *Theorie Mathematique des Phenomenes Electrodynamiques Uniquement Deduite de l'Experience*, Reprinted by Blanchard, Paris 1958.
- [8] Weber, W. (1852) *Pogg. Ann.*, LXXXVII, 167.
- [9] Ewing, J. A. (1893) *Magnetic Induction in Iron and Other Metals*, The Electrician Publishing Company, London.
- [10] L. Landau and E. Lifshitz (1935) *Physikalische Zeitschrift der Sowjetunion* 8 153.
- [11] W.F. Brown, Jr., *J. Appl. Phys.* 30, 993 (1968).
- [12] Alex Hubert and Rudolf Schäfer, *Magnetic Domains: The Analysis of Magnetic Microstructures*, Springer-Verlag Berlin Heidelberg New York 2000.
- [13] See website: [http : //www.aacg.bham.ac.uk/magneticmaterials/domains.htm](http://www.aacg.bham.ac.uk/magneticmaterials/domains.htm).
- [14] Bloch, F. (1932) *Z. Physik*, 74, 295.
- [15] L. Néel, *C. R. Hebd. Seances Acad. Sci.* 241, 533 (1955).

- [16] T. Trunk, M. Redjdal, A. Kakay, M.F. Raune and F.B. Humphrey, Domain wall structure in Permalloy films with decreasing thickness at the Bloch to Néel transition, *J. Appl. Phys.* 89, 7606 (2001).
- [17] M. Redjdal, A. Kakay, M.F. Raune and F.B. Humphrey, Cross-tie walls in thin Permalloy films, *IEEE Trans. Magn.* 38, 2471 (2002).
- [18] H. Kronmüller, *Z. Phys.* 168, 478 (1962).
- [19] G. Herzer, *IEEE Trans. Magn.* 26, 1397 (1990).
- [20] P. Bruno, Geometrically Constrained Magnetic Wall, *Phys. Rev. Lett.* 83, 2425 (1999).
- [21] H. F. Ding, W. Wulfhekel and J. Kirschner, Ultra sharp domain walls in the closure domain pattern of Co(0001), *Europhys. Lett.*, 57, 100 (2002).
- [22] M. Pratzner, H. J. Elmers, M. Bode, O. Pietzsch, A. Kubetzka, and R. Wiesendanger, Atomic-Scale Magnetic Domain Walls in Quasi-One-Dimensional Fe Nanostripes, *Phys. Rev. Lett.* 87, 127201 (2001).
- [23] R. P. Cowburn, D. A. Allwood, G. Xiong, and M. D. Cooke, Domain wall injection and propagation in planar Permalloy nanowires, *J. Appl. Phys.*, 91, 6949 (2002).
- [24] H.D. Chopra, M.R. Sullivan, J.N. Armstrong, and S.Z. Hua, The quantum spin-valve in cobalt atomic point contacts, *Nature Materials*, 4, 832 (2005).
- [25] T. R. McGuire and R. I. Potter, Anisotropic magnetoresistance in ferromagnetic 3d alloys, *IEEE Trans. Magn.* 11, 1018 (1975).
- [26] McGuire, T. Aboaf, J. Klokholm, E., Negative anisotropic magnetoresistance in 3d metals and alloys containing iridium, *IEEE Trans. Magn.* 20, 972 (1984).
- [27] M. Viret, I. Auneau and J. M. D. Coey, Anisotropic magnetotransport properties of cobalt thin films, *Journal of Magnetism and Magnetic Materials*, 140, 683 (1995).
- [28] P. P. Freitas, A. A. Gomesa, T. R. McGuire and T. S. Plaskett, Anisotropic magnetoresistance in Co films, *Journal of Magnetism and Magnetic Materials*, 83, 113 (1990).
- [29] D. Jiles, *Introduction to Magnetism and Magnetic Materials*, Chapman & Hall, pag 180 (1998).
- [30] M. Brands and G. Dumpich, Multiple switching fields and domain wall pinning in single Co nanowires, *J. Phys. D: Appl. Phys.* 38, 822 (2005).

- [31] W. J. M. de Jonge, P. J. H. Bloemen, F. J. A. den Broeder, Ultrathin Magnetic Structures, Berlin-Springer, Chapter 2.3, (1994).
- [32] M. T. Johnson, P. J. H. Bloemen, F. J. A. den Broeder and J. J. de Vries, Magnetic anisotropy in metallic multilayers, Rep. Prog. Phys. 59, 1409 (1996).
- [33] Wei-Li Lee, Frank Q. Zhu, and C. L. Chien, Determination of domain wall resistance in a cobalt thin film by thickness modulation, Appl. Phys. Lett. 88, 122503 (2006).
- [34] Dieter Buntinx, Steven Brems, Alexander Volodin, Kristiaan Temst, and Chris Van Haesendonck, Positive Domain Wall Resistance of 180° Néel Walls in Co Thin Films, Phys. Rev. Lett. 94, 017204 (2005).
- [35] T. Ono, H. Miyajima, K. Shigeto and T. Shinjo, Magnetization reversal in submicron magnetic wire studied by using giant magnetoresistance effect, Appl. Phys. Lett. 72, 1116 (1998).
- [36] K. J. Kirk, J. N. Chapman, C. D. W. Wilkinson, Lorentz microscopy of small magnetic structures (invited), J. Appl. Phys., 85, 5237 (1999).
- [37] M. Hayashi, L. Thomas, Ya. B. Bazaliy, C. Rettner, R. Moriya, X. Jiang, and S. S. P. Parkin, Influence of Current on Field-Driven Domain Wall Motion in Permalloy Nanowires from Time Resolved Measurements of Anisotropic Magnetoresistance, Phys. Rev. Lett. 96, 197207 (2006).
- [38] A. Yamaguchi, T. Ono, S. Nasu, K. Miyake, K. Mibu, T. Shinjo, Real-Space Observation of Current-Driven Domain Wall Motion in Submicron Magnetic Wires, Phys. Rev. Lett. 92, 077205 (2004).
- [39] G.G. Cabrera and L.M. Falicov, Theory of the residual resistivity of Bloch walls I: Paramagnetic effects, Phys. Stat. Sol. (b) 61, 539 (1974).
- [40] G.G. Cabrera and L.M. Falicov, Theory of the residual resistivity of Bloch walls II: Inclusion of diamagnetic effects. Phys. Stat. Sol. (b) 62, 217 (1974).
- [41] C. H. Marrows, Spin-polarised currents and magnetic domain walls, Advances in Physics, 54, 585 (2005).
- [42] L. Berger, Low-field magnetoresistance and domain drag in ferromagnets, J. Appl. Phys., 49, 2156 (1978).
- [43] M. Viret, D. Vignoles, D. Cole, J. M. D. Coey, W. Allen, D. S. Daniel, and J. F. Gregg, Spin scattering in ferromagnetic thin films, Phys. Rev. B 53, 8464 (1996).
- [44] J.F. Gregg, W. Allen, K. Ounadjela, M. Viret, M. Hehn, S.M. Thompson and J.M.D. Coey, Giant magnetoresistive effects in a single element magnetic thin film, Phys. Rev. Lett. 77, 1580 (1996).

- [45] Peter M. Levy and Shufeng Zhang, Resistivity due to Domain Wall Scattering, *Phys. Rev. Lett.* 79, 5110 (1997).
- [46] Gen Tatara and Hidetoshi Fukuyama, Resistivity due to a Domain Wall in Ferromagnetic Metal, *Phys. Rev. Lett.* 78, 3773 (1997).
- [47] R. P. van Gorkom, Arne Brataas, and Gerrit E. W. Bauer, Negative Domain Wall Resistance in Ferromagnets, *Phys. Rev. Lett.* 83, 4401 (1999).
- [48] I. A. Campbell and A. Fert, *Ferromagnetic Materials*, North-Holland, Amsterdam (1982).
- [49] S. H. Florez, M. Dreyer, K. Schwab, C. Sanchez, and R. D. Gomez, Magnetoresistive effects in planar NiFe nanoconstrictions, *J. Appl. Phys.* 95, 6720 (2004).
- [50] L.R. Tagirov, B.P. Vodopyanov and K.B. Efetov, Multivalued dependence of the magnetoresistance on the quantized conductance in nanosize magnetic contacts, *Phys. Rev. B* 65 214419 (2002).
- [51] N. Papanikolaou, Magnetoresistance through spin-polarized p states, *J. Phys.: Cond. Matt.* 15, 5049 (2003).
- [52] Harold U. Baranger and A. Douglas Stone, Electrical linear-response theory in an arbitrary magnetic field: A new Fermi-surface formation, *Phys. Rev. B* 40, 8169 (1989).
- [53] G. Tatara, Y.-W. Zhao, M. Muñoz and N. Garcia, Domain wall scattering explains 300% ballistic magnetoconductance of nanocontacts. *Phys. Rev. Lett.* 83, 2030 (1999).
- [54] H. Imamura, N. Kobayashi, S. Takahashi and S. Maekawa, Conductance quantization and magnetoresistance in magnetic point contacts, *Phys. Rev. Lett.* 84, 1003 (2000).
- [55] L.R. Tagirov, B.P. Vodopyanov and K.B. Efetov, Ballistic versus diffusive magnetoresistance of a magnetic point contact, *Phys. Rev. B* 63, 1044428 (2001).
- [56] N. Garcia, M. Muñoz, and Y.-W. Zhao, Magnetoresistance in excess of 200% in Ballistic Ni Nanocontacts at Room Temperature and 100 Oe, *Phys. Rev. Lett.* 82, 2923 (1999).
- [57] N. Garcia, H. Rohrer, I. G. Saveliev, and Y.-W. Zhao, Negative and Positive Magnetoresistance Manipulation in an Electrodeposited Nanometer Ni Contact, *Phys. Rev. Lett.* 85, 3053 (2000).
- [58] Harsh Deep Chopra and Susan Z. Hua, Ballistic magnetoresistance over 3000% in Ni nanocontacts at room temperature, *Phys. Rev. B* 66, 020403 (2002).

- [59] Susan Z. Hua and Harsh Deep Chopra, 100,000 % ballistic magnetoresistance in stable Ni nanocontacts at room temperature, *Phys. Rev. B* 67, 060401 (2003).
- [60] W.F. Egelhoff, L. Gan, H. Ettetdgui, Y. Kadmon, C.J. Powell, P.J. Chen, A.J. Shapiro, R.D. McMichael, J.J. Mallett, T.P. Moffat, M.D. Stiles and E.B. Svedberg, Artifacts in ballistic magnetoresistance measurements. *J. Appl. Phys.* 95 7554 (2004).
- [61] E.B. Svedberg, J.J. Mallett, H. Ettetdgui, L. Gan, P.J. Chen, A.J. Shapiro, T.P. Moffat and W.F. Egelhoff Jr, Resistance changes similar to ballistic magnetoresistance in electrodeposited nanocontacts, *Appl. Phys. Lett.* 84, 236 (2004).
- [62] J.J. Mallett, E.B. Svedberg, H. Ettetdgui, T.P. Moffat and W.F. Egelhoff Jr, Absence of ballistic magnetoresistance in Ni nanocontacts controlled by an electrochemical feedback system, *Phys. Rev. B* 70 172406 (2004).
- [63] C.-S. Yang, J. Thiltges, B. Doudin and M. Johnson, In situ monitoring of quantum conductance in electrodeposited magnetic point contacts. *J. Phys.: Cond. Matt.*, 14 L765 (2002).
- [64] N. Garcia, H. Wang, H. Cheng and N.D. Nikolic, Ballistic magnetoresistance versus magnetostriction effects in electrodeposited nanocontacts at room temperature, *IEEE Trans. Magn.* 39 2776 (2003).
- [65] M.R. Sullivan, D.A. Boehm, D.A. Ateya, S.Z. Hua and H.D. Chopra, Ballistic magnetoresistance in nickel single-atom conductors without magnetostriction, *Phys. Rev. B* 71 024412 (2005).
- [66] O. Cspedes, S. M. Watts, J. M. D. Coey, K. Dörr, and M. Ziese, Magnetoresistance and electrical hysteresis in stable half-metallic $La_{0.7}Sr_{0.3}MnO_3$ and Fe_3O_4 nanoconstrictions, *Appl. Phys. Lett.* 87, 083102 (2005).
- [67] Clifford, E., Venkatesan, M., Gunning, R., Coey, J.M.D., Magnetoresistance in point contacts of the Heusler alloy $Co_2Cr_{0.6}Fe_{0.4}Al$, *Solid State Communications*, 131, 61 (2004).
- [68] C. Rüster, T. Borzenko, C. Gould, G. Schmidt, L.W. Molenkamp, X. Liu, T.J. Wojtowicz, J.K. Furdyna, Z.G. Yu and M.E. Flatté, Very large magnetoresistance in lateral ferromagnetic (Ga,Mn)As wires with nanoconstrictions, *Phys. Rev. Lett.* 91, 216602 (2003).
- [69] M.I. Montero, R.K. Dumas, G. Liu, M. Viret, O.M. Stoll, W.A.A. Macedo and I.K. Schuller, Magnetoresistance of mechanically stable Co nanoconstrictions, *Phys. Rev. B* 70, 184418 (2004).
- [70] O. Ozatay, P. Cahlsani, N. Emley, I.N. Krivorotov and R.A. Buhrman, Magnetoresistance and magnetostriction effects in ballistic ferromagnetic nanoconstrictions, *J. Appl. Phys.* 95, 7315 (2004).

- [71] M. Viret, S. Berger, M. Gabureac, F. Ott, D. Olligs, I. Petej, J.F. Gregg, C. Fermon, G. Francinet and G. Le Goff, Magnetoresistance through a single nickel atom, *Phys. Rev. B* 66, 220401 (2002).
- [72] M. Gabureac, M. Viret, F. Ott and C. Fermon, Magnetoresistance in nanocontacts induced by magnetostriction effects, *Phys. Rev. B* 69 100401, (2004).
- [73] M. Viret, M. Gabureac, F. Ott, C. Fermon, C. Barreteau, G. Autes, and R. Guirado-Lopez, Giant anisotropic magneto-resistance in ferromagnetic atomic contacts, *Eur. Phys. J. B* 51, 1, (2006).
- [74] J. Velev, R.F. Sabirianov, S.S. Jaswal and E.Y. Tsymbal, Ballistic anisotropic magnetoresistance, *Phys. Rev. Lett.* 94, 127203 (2005).
- [75] S. Khizroev, Y. Hijazi, R. Chomko, S. Mukherjee, R. Chantrell, X. Wu, R. Carley and D. Litvinov, Focused-ion-beam-fabricated nanoscale magnetoresistive ballistic sensors, *Appl. Phys. Lett.* 86, 042502 (2005).
- [76] Z. K. Keane, L. H. Yu, and D. Natelson, Magnetoresistance of atomic-scale electromigrated nickel nanocontacts, *Appl. Phys. Lett.* 88, 062514 (2006).
- [77] M. J. Donahue and D. G. Porter, <http://math.nist.gov/oommf/>
- [78] P. Rai-Choudhury, Editor, *Handbook of Microlithography, Micromachining, and Microfabrication*, Spie, Washington, 1997.
- [79] P. Grutter, H. J. Mamin and D. Rugar, *Magnetic Force Microscopy*, Springer Ser. Surface Sciences, Vol. 28 (Springer, Berlin, Heidelberg 1992)
- [80] Digital Instruments, Santa Barbara, California, USA, <http://www.di.com>. Patent.
- [81] J. M. Garcia, A. Thiaville, J. Miltat et al., Quantitative interpretation of magnetic force microscopy images from soft patterned elements, *Appl. Phys. Lett.* 79, 656 (2001).
- [82] J.L. Olsen, *Electron Transport in Metals*, Wiley Interscience, New York/London (1962).
- [83] B. Leven and G. Dumpich, Resistance behavior and magnetization reversal analysis of individual Co nanowires, *Phys. Rev. B* 71, 064411 (2005).
- [84] J. Nogues and I. K. Schuller, *J. Magn. Magn. Mater.* 192, 203 (1999).
- [85] D. A. Allwood, Gang Xiong, and R. P. Cowburn, Domain wall diodes in ferromagnetic planar nanowires, *Appl. Phys. Lett.* 85, 2848 (2004).
- [86] J. F. Gregg, W. Allen, K. Ounadjela, M. Viret, M. Hehn, S. M. Thompson, and J. M. D. Coey, Giant Magnetoresistive Effects in a Single Element Magnetic Thin Film, *Phys. Rev. Lett.* 77, 1580 (1996).

- [87] M. Fraune, U. Rüdiger, G. Güntherodt, S. Cardoso and P. Freitas, Size dependence of the exchange bias field in NiO/Ni nanostructures, *Appl. Phys. Lett.* 77, 3815 (2000).
- [88] M. Bolte, M. Steiner, C. Pels, M. Barthelme, J. Kruse, U. Merkt, G. Meier, M. Holz, D. Pfannkuche, Magnetotransport through magnetic domain patterns in permalloy rectangles, *Phys. Rev. B* 72, 224436 (2005).
- [89] See website: [http : //www.aip.org/eneews/physnews/2002/split/595 – 1.html](http://www.aip.org/eneews/physnews/2002/split/595-1.html).
- [90] D. A. Allwood, G. Xiong, C. C. Faulkner, D. Atkinson, D. Petit, R. P. Cowburn, Magnetic Domain-Wall Logic, *Science* 309, 1688 (2005).
- [91] S. S. P. Parkin, U.S. Patent No. 6834005 (2004).
- [92] B. Zhao, I. Mönch, T. Mühl, H. Vinzelberg, and C. M. Schneider, Spin-dependent transport in multiwalled carbon nanotubes, *J. Appl. Phys.* 91, 7026 (2002).
- [93] B. Zhao, I. Mönch, H. Vinzelberg, T. Mühl, and C. M. Schneider, Spin-coherent transport in ferromagnetically contacted carbon nanotubes , *Appl. Phys. Lett.* 80, 3144 (2002).
- [94] Ali Javey, Jing Guo, Qian Wang, Mark Lundstrom and Hongjie Dai, Ballistic carbon nanotube field-effect transistors, *Nature* 424, 654 (2003).
- [95] Semenov Y G, Kim K W and Iafrate G J, Preprint cond-mat 0602425 (2006).
- [96] Sangeeta Sahoo, Takis Kontos, Jürg Furer, Christian Hoffmann, Matthias Gräber, Audrey Cottet and Christian Schönenberger, Electric field control of spin transport, *Nature Physics* 1, 99 (2005).
- [97] Ane Jensen, Jonas R. Hauptmann, Jesper Nygård, and Poul Erik Lindelof, Magnetoresistance in ferromagnetically contacted single-wall carbon nanotubes, *Phys. Rev. B* 72, 035419 (2005).
- [98] A. Cottet, T. Kontos, S. Sahoo, H. T. Man, M-S Choi, W. Belzig, C. Bruder, A. F. Morpurgo and C. Schönenberger, Nanospintronics with carbon nanotubes, *Semicond. Sci. Technol.* 21, S78S95 (2006).
- [99] S. Krompiewski, Theoretical studies of spin-dependent electrical transport through carbon nanotubes, *Semicond. Sci. Technol.* 21, S96S102 (2006).
- [100] Sander J. Tans, Michel H. Devoret, Remco J. A. Groeneveld and Cees Dekker, Electron-electron correlations in carbon nanotubes, *Nature* 394, 761 (1998).

- [101] Wenjie Liang, Marc Bockrath, Dolores Bozovic, Jason H. Hafner, M. Tinkham and Hongkun Park, Fabry - Perot interference in a nanotube electron waveguide, *Nature* 411, 665 (2001).
- [102] Takayoshi Kanbara et al., Contact resistance modulation in carbon nanotube devices investigated by four-probe experiments, *Appl. Phys. Lett.* 88, 053118 (2006).

Acknowledgments

I would like to thank the people who have accompanied, supported and guided me throughout the time of my thesis:

Prof. Dr. Claus M. Schneider, my supervisor, for giving me the opportunity to join his group, for his guidance, help and support during the course of my PhD research.

Dr. Henning Dassow and Dr. Guzenko Vitaly, for sharing their experience in the experimental work in the clean room, useful discussions and assistance at the early stages of my work.

Dr. A. van der Hart, he taught me the basics of electron beam lithography and prepared most of the samples used in this thesis.

PD Dr. Riccardo Hertel, for helping me with the interpretation of the experimental results based on micromagnetic simulations.

DP Sebastian Gliga and Dr. Attila Kakay, for their help with the micromagnetic simulations and discussions about micromagnetism.

Dr. Carola Meyer for fruitful discussions and proofreading the thesis.

Dr. Daniel Bürgler for instructive discussions.

Dr. Matthias Buchmeier for MOKE measurements and fruitful discussions.

Dr. Diana Rata for SQUID and XRD measurements.

Bernd Küpper, who helped me saving a lot of time by building for me a small deposition chamber.

All the other people of the Electronic Properties group for the great atmosphere and moments spent together as well as for their helpful remarks and assistance.

My parents for their spiritual and financial support.

My wife, Olga, and my daughters, Stefania and Emila, for their loving support and understanding.

Curriculum Vitae

Personal details

Name: George Sarau
Date and place of birth: February 25, 1978, Macin, Romania
Marital Status: Married, 2 children
Nationality: Romanian

Education

since Oct'03 PhD student
Institute of Electronic Properties, Department of Solid State Research
Research Center Jülich, Germany

Oct'01-Feb'03 M.Sc. Degree Diploma
Thesis name: Alternative High-k Gate Dielectrics for Microelectronics
Faculty of Physics, University of Bucharest, Romania

Oct'96-July'01 University B.Sc. Degree
Thesis name: Liquid Crystal Displays
Faculty of Physics, University of Bucharest, Romania

Scientific activity

Magnetization Reversal of Micron-Scale Cobalt Structures with a Nanoconstriction, **G. Sarau**, S. Gliga, R. Hertel and C. M. Schneider; IEEE Trans. Magn. **43**, 2854 (2007).

Magnetoresistance Response of Cobalt Nanocontacts Between Extended Magnetic Electrodes, **G. Sarau** and C. M. Schneider; paper submitted to Journal of Applied Physics.

Tuning magnetoresistance response of nanocontacts by electrode design, **G. Sarau**, S. Gliga, R. Hertel and C. M. Schneider; oral presentation at the 10th Joint MMM/Intermag Conference, January, 2007.

Fabrication and magnetoresistance measurements of ferromagnetic nanocontacts, **G. Sarau**, R. Hertel, A. van der Hart, M. Weides, C. M. Schneider; poster presented at the Spring School "Nanomagnetism and Spintronics", May 24 - June 3, 2005, Cargese, Corsica.

Publications

(not related with this thesis - work performed at the National Institute of Materials Physics, Bucharest, Romania)

Structural, electrical, and photoelectrical properties of $\text{Cd}_x\text{Pb}_{1-x}\text{S}$ thin films prepared by chemical bath deposition; Pentia, E., Draghici, V., **Sarau, G.**, Mereu, B., Pintilie, L., Sava, F., Popescu, M.; *Journal of the Electrochemical Society* 151 (11), pp. G729-G733, (2004).

Electrical properties of metal-oxide-silicon structures with LaAlO_3 as gate oxide; Mereu, B., **Sarau, G.**, Dimoulas, A., Apostolopoulos, G., Pintilie, I., Botila, T., Pintilie, L., Alexe, M.; *Materials Science and Engineering B: Solid-State Materials for Advanced Technology* 109 (1-3), pp. 94-98 (2004).

Field-effect transistor based on nanometric thin CdS films; Mereu, B., **Sarau, G.**, Pentia, E., Draghici, V., Lisca, M., Botila, T., Pintilie, L.; *Materials Science and Engineering B: Solid-State Materials for Advanced Technology* 109 (1-3), pp. 260-263 (2004).

Field effect assisted thermally stimulated currents in CdS thin films deposited on SiO_2/Si substrates; Lisca, M., Pentia, E., **Sarau, G.**, Pintilie, L., Pintilie, I., Botila, T.; *Journal of Optoelectronics and Advanced Materials* 5 (4), pp. 849-852 (2003).

Conduction mechanisms in SrTiO_3 thin films on silicon; Mereu, B., **Sarau, G.**, Alexe, M.; *Materials Research Society Symposium - Proceedings* 747, pp. 165-170 (2003).